Politechnika Krakowska im. Tadeusza Kościuszki
Wydział Inżynierii Środowiska i Energetyki
Katedra Procesów Cieplnych, Ochrony Powietrza
i Utylizacji Odpadów

# Mathematical modeling of heat exchangers taking into account different correlations on the air-side Nusselt number on each tube row

Rozprawa doktorska

Autor:
mgr inż. Mateusz Marcinkowski

Promotor:
prof. dr hab. inż. Dawid Taler

Promotor pomocniczy:
dr inż. Jacek Sacharczuk

Kraków, 2023

# Contents

# 1 Introduction

The plate fin and tube heat exchangers are the driving force behind the constant search for novel and more sophisticated methods for modeling and analysis, with the aim of achieving increased precision within shorter timeframes. One of the biggest challenges in modeling plate fin and tube heat exchangers is the very high complexity of the design. Consequently, the analysis necessitates a simplification strategy, involving the division of the structure into recurring segments to facilitate more simplified investigations [1][2].

The present study is strongly related to basic research, directed at formulating a universal methodology that will be independent of the geometry of the heat exchanger. This methodology is designed to determine the average Nusselt number on the individual tube rows for a variety of heat exchanger configurations, achieved through three different methods based on computational fluid dynamics (CFD) simulations. By utilizing these methods, correlations can be established for Nusselt numbers and subsequently validated through experiments. These newly established correlations can be used for the utilization of more efficient and cost-effective analysis techniques, effectively eliminating the need for laborious and expensive experimental trials.

The results of this work not only expand our knowledge of heat exchange processes but also of the influence of heat exchanger design on the dimensions and placement of dead zones – a factor that affects the efficiency of the heat transfer process. Moreover, significant attention has been directed toward solving problems associated with the direct measurement of average mass air temperatures for individual rows. Achieving a high-efficiency approach to the heat transfer process in heat exchangers is based on an innovative method based on analysis of both CFD simulations and experimental findings.

Using the results and correlations derived from experimental studies, a comprehensive mathematical model has been formulated and programmed using the C++ programming language. This model is dedicated to heat exchanger modeling on a wider scale, thereby offering a versatile tool for researchers and engineers in the field.

The results of this work not only expand our knowledge of heat exchange processes but also provide practical tools and methodologies that can be used in the design and optimization of various types of heat exchangers. The presented universal method for determining average Nusselt number values and heat transfer coefficients represents a significant step toward improving the efficiency and understanding of these processes. Improving the efficiency of the heat transfer process taking place in plate fin and tube heat exchangers is crucial for the future development of technologies utilizing finned tubular heat exchangers such as heat pumps, waste heat recovery units [3][4] and in the heating, ventilation, air conditioning and refrigeration (HVAC&R) industry [5][6].

# 2 State of the art

## 2.1 Analysis of the existing state of the art of design of plate fin and tube heat exchangers

The complex structure of the plate fin and tube heat exchanger requires two main methods to increase its output [7][8]. First, it can be done by increasing a the heat transfer surface area using experimental verifications [9], CFD simulations [10] or mathematical modelling [11] of various tube or fin geometries, transverse or longitudinal tube spacing, fin spacing and fin width, tube arrangements or number of tube rows [12][13][14][15][16]. As far as fin geometries are concerned, one can distinguish between straight fins [17][18][19], wavy fins [20][21], louvred fins [22][23], slit fins [24][25], fins with turbulence generators [26], and fins with delta winglets [27].

Each of these geometries can be optimized to maximize the air-side heat transfer coefficient (HTC). The tube's geometry (diameter and shape) can affect heat transfer. Their influence can be studied in terms of changes in the diameter of the tubes in the case of circular tubes [28] as well as the size of the tubes' flatness in the case of elliptical tubes [29] and flat tubes [30]. Due to the work-intensive research, most common articles present studies with a single tube diameter (for example, 8 mm [31], 8.53 mm [32], 9.93 mm [33], 10 mm [34], 12 mm [35] or 15.9 mm [36]). In contrast, studies on tube diameter optimization are rare (2-27 mm [28], 7.53-10.23 mm [37] or 16-20 mm [38]). The spacing of transverse and longitudinal tubes is more often discussed as an opportunity to increase the heat transfer of compact heat exchangers [38][33]. Researchers seek to optimize the division of transverse and longitudinal tubes to maximize heat transfer and minimize pressure losses during gas flow through the exchanger [39].

Another element that is considered is fins' spacing [40] and width [41]. The possibility of using specific fin spacing is very application-dependent. A larger fin spacing [42] is considered when there is a possibility of excessive contamination [43] or icing of the heat exchanger [44]. On the other hand, a smaller fin spacing [45][46] is used in a controlled and pollution-free environment [47]. Furthermore, often with the study of different divisions of the fins comes a check of a specific range of their thickness to increase heat transfer or the Energy Efficient Index [48].

Finally, it is possible to analyze the layout and number of rows of tubes in the heat exchanger. There are two possibilities regarding tube arrangement: straight [49] and staggered [50]. The number of rows can vary from 1 [51] to even 7 [52]. Intuitively, it can be indicated that the more rows of the exchanger, the greater the total amount of exchanged heat [53]. Still, it turns out that this is not a linear relationship and it is very dependent on the gas velocity in front of the exchanger [54]. In addition, every exchanger works in a completely different way, and there are other phenomena that may increase or

decrease the amount of energy exchanged in a particular row [55]. The second method is to increase the air-side heat transfer coefficient by using various types of additional structural elements on the surface of the tubes or fins, which cause increased turbulence and mixing of flows [56][57]. Of course, these methods can increase pressure drop, which is why the Energy Efficiency Index (EEI), which describes the ratio of power output to pressure drop, is examined frequently [58]. Printing heat exchangers [59][60][61][62] or obtaining more complex structures like metal porous foam [63], woven wire fin [64] or lattice metal frame [56] are also increasingly discussed. All of these structures allow for increased heat transfer coefficient [65] and can be manufactured using a standard manufacturing process. Printed exchangers (metal or polymer [66][67][68]) are able to achieve geometries and turbulence levels that are impossible with standard exchangers [69][70].

Rising copper prices and the demand for lightweight materials recently is driving the desire for new designs such as micro-channel heat exchangers [71][72][73][74]. This solution can reduce the weight of the exchanger, improve its compactness, and increase the heat transfer coefficient [75]. Additionally, it is possible to replace copper with cheaper aluminium [76][77]. Micro-channel heat exchangers are currently being researched [78] and are applied in many fields [79].

The type of liquid flowing inside the exchanger can significantly affect the heat transfer coefficient on the air-side. This can be achieved using nanofluids instead of standard liquids like water. A nanofluid is a fluid containing nano-sized particles, compared to the base fluid, increase the convective heat transfer coefficient and thermal conductivity [80][81][82]. The novel properties of nanofluids have applications in heat exchangers in various fields including microelectronics, fuel cells, hybrid-powered engines, and many more [83].

Standard methods of maximizing the power of compact heat exchangers while minimizing their size were most often based on parameterization of one parameter, e.g., tube spacing or fin type. Otherwise, it will be a time- and work-consuming task. In the era of computers, with significant computing power, it is possible to create algorithms that will be able to change many of the parameters in order to achieve the required initial assumptions. Most often, these are genetic algorithms classified as evolutionary algorithms [84][85] or machine learning algorithms [86]. Most of the time these are optimization algorithms. Genetic algorithms are a kind of heuristic that searches the space of alternative solutions to a problem in order to find the best solutions [87], and machine learning algorithms that, improve automatically through exposure to data [88]. These algorithms are the next step as far as testing heat exchangers go; however, they are not the subject of this dissertation.

## 2.2 Correlations for determining air-side heat transfer coefficients

The design of plate fin and tube heat exchangers, which include thin metal sheets intersecting with metal tubes with different tube rows, fin spacing, and tube diameter and spacing, causes complex phenomena, especially on the air-side [5]. Each row in the heat exchanger transfers heat from one fluid to another differently. These differences may result from different air and water supply temperatures, air velocity, and air turbulence. They also show a more important issue, such as differences in the average heat transfer coefficient between each row [54].

The operating characteristics of compact heat exchangers are usually determined experimentally. This is due to the high complexity of tested devices and systems. Experimental studies are also widely used to determine the flow and thermal characteristics of finned tube heat exchangers [89]. Heat transfer correlations are created on the side of the flowing liquid, which is usually water [90], and the flowing gas, which is usually air, in a wide range of Reynolds numbers. The effectiveness of various types of design improvements, such as oval tubes, new fin shapes, or heat exchanger air flow blades, is also evaluated experimentally. The above methods are described in detail in the previous paragraphs.

The experimental results have high credibility, but one of the main concerns is their cost. To determine the experimental correlations with different numbers of tubes and rows, it is necessary to build an experimental stand equipped with complex measuring equipment and an advanced hydraulic system. Therefore, computational fluid dynamics (CFD) modeling is increasingly popular in the development of tubular cross-flow heat exchangers [91]. The impact of various innovations in the design of the exchanger is modeled in different ranges of Reynolds numbers on the gas side as well as on the liquid side. One such innovation could be the placement of four circular convex strips to improve heat transfer on the air-side [92]. It is not possible to completely eliminate experimental research. In this case, the experiment partially encapsulates verifying results [93]. Hence, CFD modeling allows for greater flexibility in research and industry. So far, many correlations of the Nusselt number, Colburn factor, or HTC have been determined. Most studies present only average Nusselt number correlations for the entire exchanger. Some studies reported studies to determine local HTC values within the entire exchanger, and few studies to date reported results or determined row-specific average Nusselt number correlations in multi-row PFTHEs.

The first group of studies reviewed looked at the mean HTC values in PFTHE. Gonzalez et al. [94] reported average Nusselt numbers depending on the fin material and Reynolds numbers for double-row in-line PFTHE. Lindqvist et al. [19] carried out CFD studies taking into account different angles of tube bundles. They also presented graphs with the Colburn parameter for low Reynolds numbers. Elmekawy et al. [95] showed

that attaching splitter plates to tubes can increase the Nusselt number and reduce the pressure drop. Petrik and Szepesi [96] determined the correlations of the Nusselt number for single-row and double-row U-shaped heat exchangers. Additionally, in another study by Petrik et al. [97], numerical Nusselt correlations have been presented in the case of standard PFTHE. Khan et al. [98] examined twisted oval HEX tubes and determined average Nusselt numbers and pressure drop correlations. Łecki et al. [99] presented a comparison of the HTC obtained by CFD simulation with the help of Verein Deutscher Ingenieure (VDI), calculated by correlation for a three-row in-line PFTHE. Okbaz et al. [100] presented different correlations of Colburn factors for PFTHE with different numbers of rows. However, they were averaged across the entire PFTHE. Sadeghianjahromi et al. [14] determined the HTC and pressure drop coefficients in PFTHE with different types of fins and round and flat tubes under dry and wet conditions. Awais and Bhuiyan [50] wrote a review article where they presented many correlations to the Colburn parameter.

All of the previously described studies refer to mean Nusselt numbers, Colburn coefficients, or HTC correlations for the entire exchangers or show the local HTC distribution within the exchangers to predict heat transfer correlations for the entire PFTHE. Only a few studies showing heat transfer correlations for individual rows in PFTHE can be found. In the 1970s, Rich et al. [101] performed experimental studies in which they determined the Colburn coefficients for each row of tubes in multi-row PFTHEs (from one to eight rows). This was the first time when the differences in HTC within PFTHE were shown. After many years, possibly due to the lack of use for this type of gaze, Taler et al. [54] determined individual Nusselt number correlations for each row in the case of double-row PFTHE.

Developing new analytical methods for calculating compact heat exchangers for a more precise design of their geometry [102], requires more individual relationships for heat exchange inside the exchanger [103][55]. Here, the great practical importance of the correlation of heat exchange on individual rows of tubes for heat exchangers with different numbers of rows of tubes is shown, and their occurrence in the literature is currently marginal.

In addition, returning the study by Rich et al. [101] showed that further rows of tubes in multi-row PFTHE are inefficient when the air velocity is low and the airflow in the exchanger is laminar. However, Nusselt number correlations for individual rows of tubes have not been developed. Taler et al. [54] showed that in a two-row car radiator made of round or oval tubes, the first row of tubes is more efficient than the second one when the air velocity is lower than 2.5 m/s. However, exchangers with more tubes have not been modeled by CFD or investigated experimentally. There are still many issues to be solved when looking at compact heat exchangers, i.e., a larger PFTHE cross-section but with fewer rows would be more efficient than a three, four or five-row PFTHE. Which rows are the least efficient? Should we consider individual correlations for multi-row PFTHEs?

## 2.3 Purpose, scope, and thesis of the work

The determination of experimental correlations for heat exchangers is carried out on the basis of experimental studies which are very time-consuming and costly. Usually, correlations are determined for the entire heat exchanger of a certain design, which limits the applicability of these correlations to other heat exchangers, e.g., differing in the number of tube rows. To date, there is little experimental work on the determination of correlations for the Nusselt number on individual tube rows. The exception is the experimental work of Rich [101], who determined the values of average Nusselt numbers on given tube rows as a function of Reynolds number.

From the literature review, there is a lack of information on how the value of airflow velocity (Reynolds number) affects the distribution of Nusselt numbers on individual tube rows along the airflow path.

**Objective**

In this dissertation, the results of CFD modeling of a 4-row plate fin and tube heat exchanger will be carried out for air velocities from 0.5 to 10 m/s. For low air velocities in front of the exchanger, not exceeding 3 m/s, the Nusselt number for the first row is the highest and successively decreases in the following tube rows. On the fourth and further rows of tubes, there is a stabilization of the flow and heat transfer conditions, which makes the Nusselt numbers very similar. At higher air velocities upstream of the exchanger, when the airflow in the exchanger becomes turbulent, the distribution of average Nusselt numbers on individual tube rows along the airflow path changes. The Nusselt numbers on individual tube rows are similar.

Given the widespread use of plate fin and tube heat exchangers for heating or cooling air, the determination of individual correlations on individual tube rows is interesting not only from a cognitive but also from a practical point of view. Knowing the individual correlations on the 1st, 2nd, 3rd, and further rows of tubes, it is possible to choose the most efficient design of the exchanger. The optimal number of tube rows for the sum of investment and operating costs can be selected.

The individual correlations on each tube row, determined by CFD modeling and experiment, will be compared with each other. In order to conduct experimental verification of CFD modeling, a test stand was built on which 4-row plate fin and tube heat exchangers with a staggered (checkerboard) arrangement of tubes with plain fins and round tubes were examined. Hot water flowed inside the tubes, while cooler air flowed transversely to the axis of the tubes. Air velocities in front of the exchanger varied from 0.5 to 10 m/s during the CFD simulations and from 0.5 to 5 m/s during the experimental tests.

**Thesis**

The nature of the changes in Nusselt numbers in successive tube rows of a plate fin and tube heat exchanger depends mainly on the air velocity in front of the exchanger (Reynolds number). Air-side Nusselt numbers on individual tube rows vary significantly for average values for the entire exchanger.

For low air velocities in front of the exchanger, when the Reynolds number related to the hydraulic diameter varies from 200 to 2,200 - 3,600 (this corresponds to changes in air velocity in front of the exchanger from 0.5 m/s to 2.5 - 6 m/s), the Nusselt number for the first row is the highest, the second and fourth row is placed near the average value.

For higher air velocities in front of the exchanger, when the Reynolds number related to the hydraulic diameter changes from 2,200 - 3,600 to 6,000 (corresponding to changes in air velocity in front of the exchanger from 2.5 - 6 m/s to 10 m/s), the Nusselt number for the second and fourth row has the highest value. The first row comes closer to the average value of the Nusselt number for the entire heat exchanger.

The third row has the least Nusselt number in the entire Reynolds number range from 200 to 6,000.

# 3 CFD simulation of flow and heat transfer of the plate fin and tube heat exchanger

## 3.1 Fundamentals of fluid flow

The basis of CFD modeling is the equations of the conservation of mass, momentum, and energy. In addition to these equations, constitutive equations, e.g., Newton's law of viscosity and Fourier's law of heat conduction, are required to build a mathematical model of heat flow and heat transfer. The coefficients in the constitutive equations are determined experimentally, e.g., in Fourier's law it is the heat conduction coefficient, and in Newton's law the dynamic viscosity. At the edge of the analyzed area, boundary conditions of the first (Dirichlet condition), second (Neumann condition), or third kind (Robin condition, also called Newton's cooling law) must be given. For unsteady issues, the initial conditions for time $t = 0$ must be given, e.g., the initial distribution of pressure, temperature, and velocity.

The equations of conservation of mass, momentum and energy, constitutive relationships, boundary conditions, and initial conditions form the basis for building a mathematical model of a given process. If the fluid flow is turbulent, a turbulent flow model is usually needed. If it is possible to solve the mathematical model equations for a turbulent flow without using a turbulence model (Direct Numerical Simulation, abbreviated DNS), then a turbulence model of the flow is unnecessary. However, it should be emphasised

that due to the low computing power of computers, the DNS method can only be used for simple steady-state problems, as the computer calculation time is very long. In this dissertation, the modeling of the flow and heat transfer in the exchanger was carried out using Ansys Fluent 2022 R2.

### 3.1.1 Mass conservation equation

The continuity equation, or equation for the conservation of mass, can be written as follows [104]:

$$\frac{\partial \rho}{\partial t} = \nabla \cdot (\rho \mathbf{v}) = S_m \tag{3.1}$$

Eq 3.1 is the generic version of the mass conservation equation and is applicable to both incompressible and compressible flows. Source $S_m$ is the mass contributed to the continuous phase from the dispersed second phase (for example, vaporization of liquid droplets) and any user-defined sources. The notation convention used in Eq. 3.2 in vector calculus, using the nabla symbol $\nabla$. It facilitates the description of the gradient (for a scalar field) or a variety of differential operators including the derivative (corresponding to the gradient), divergence, and rotation (for a vector field, as in this case (Eq. 3.3)) or Laplacian (for a vector or scalar field).

$$\nabla = (\frac{\partial}{\partial x}, \frac{\partial}{\partial y}, \frac{\partial}{\partial z}) \tag{3.2}$$

In a three-dimensional Euclidean space with a Cartesian coordinate system ($x$, $y$, $z$), the nabla is defined by partial derivatives. In addition, if in this space we consider a velocity vector field (**u** - velocity vector in x-direction, **v** - velocity vector in y-direction, **w** - velocity vector in z-direction) of the variables ($x$, $y$, $z$), then the divergence ($div$) **v** being a scalar field can be expressed by the scalar product of the nabla by **v**:

$$div \cdot \mathbf{v} = \nabla \cdot \mathbf{v} = \frac{\partial \mathbf{u}}{\partial x} + \frac{\partial \mathbf{v}}{\partial y} + \frac{\partial \mathbf{w}}{\partial z} \tag{3.3}$$

### 3.1.2 Momentum conservation equations

The conservation of momentum in a non-accelerating (inertial) reference frame is defined as follows [104]:

$$\frac{\partial}{\partial t}(\rho \mathbf{v}) + \nabla \cdot (\rho \mathbf{v}\mathbf{v}) = -\nabla p + \nabla \cdot \boldsymbol{\tau} + p\mathbf{g} + \mathbf{F} \tag{3.4}$$

where $p$ is the static pressure, $\boldsymbol{\tau}$ is the stress tensor (Eq. 3.5), and $p\mathbf{g}$ and **F** are the gravitational body forces and the external body forces, respectively. **F** can also contain other model-dependent source terms. The stress tensor $\boldsymbol{\tau}$ can be written as follows:

$$\boldsymbol{\tau} = \mu \left[ (\nabla \mathbf{v} + \nabla \mathbf{v}^T) - \frac{2}{3} \nabla \cdot \mathbf{v} I \right] \tag{3.5}$$

where $\mu$ is the molecular viscosity, $I$ is the unit tensor and the second term on the right is the effect of volume dilation.

### 3.1.3 Energy conservation equations

The energy equation is solved in the following form [104]:

$$\frac{\partial}{\partial t}(\rho(e+\frac{v^2}{2})) + \nabla \cdot (\rho v(h+\frac{v^2}{2})) = \nabla \cdot (k_{eff}\nabla T - \sum_j h_j \mathbf{J}_j + \boldsymbol{\tau} \cdot \mathbf{v}) + S_h \quad (3.6)$$

where $k_{eff}$ is the effective conductivity ($k + k_t$, where $k_t$ is the turbulent thermal conductivity, defined according to the turbulence model used) and $\mathbf{J}_j$ is the diffusion flow of species. The first three components are on the right side of Eq. 3.6 reflect energy transfer by conduction, species diffusion, and viscous dissipation, in this order. $S_h$ contains the volumetric heat sources. Additionally, $h$ is defined as an enthalpy for an ideal gas:

$$h = \sum_j Y_j h_j \quad (3.7)$$

and below equation includes the contribution from pressure work for incompressible materials:

$$h = \sum_j Y_j h_j + \frac{p}{\rho} \quad (3.8)$$

In the preceding equations, Eq. 3.7 and Eq. 3.8, $Y_j$ is the mass fraction of species j, and $h_j$ is the component of enthalpy that includes solely changes in enthalpy owing to specific heat:

$$h_j = \int_{T_{ref}}^{T} c_{p,j} dT \quad (3.9)$$

Here $T_{ref}$ depends on the models used in the software solver. The internal energy $e$ is defined for both compressible and incompressible materials:

$$e = h - \frac{p_{op} + p}{\rho} \quad (3.10)$$

where $p$ is the gauge pressure and $p_{op}$ is the operating pressure. One can also include the definition of enthalpy and internal energy for an incompressible ideal gas in a common formula:

$$h = c_p T + \frac{p}{\rho} \quad (3.11)$$

### 3.1.4 Basic principles of turbulence modeling using Reynolds averaging

In this work, the Reynolds averaging model was used to model turbulence [104]. The solution variables in the instantaneous (exact) Reynolds averaging Navier-Stokes (RANS) equations are divided into mean (ensemble-averaged or time-averaged) and fluctuating components. Regarding the velocity components:

$$u_i = \overline{u}_i + u_i^{'} \quad (3.12)$$

where $\overline{u}_i$ and $u_i^{'}$ are the mean and fluctuating velocity components ($i$ = 1,2,3). However, a scalar component $\varphi$ such as pressure, energy, or other scalar variables can be written:

$$\varphi = \overline{\varphi} + \varphi^{'} \tag{3.13}$$

The ensemble-averaged momentum equations are obtained by substituting formulas of this kind for the flow variables into the instantaneous continuity and momentum equations and taking a time (or ensemble) average (and dropping the over bar on the mean velocity). In Cartesian tensor form, they are as follows:

$$\frac{\partial \rho}{\partial t} + \frac{\partial}{\partial x_i}(\rho u_i) = 0 \tag{3.14}$$

$$\frac{\partial}{\partial t}(\rho u_j) + \frac{\partial}{\partial x_i}(\rho u_i u_j) = -\frac{\partial p}{\partial x_i} + \frac{\partial}{\partial x_i}\left[\mu(\frac{\partial u_i}{\partial x_j} + \frac{\partial u_j}{\partial x_i} - \frac{2}{3}\delta_{i,j}\frac{\partial u_i}{\partial x_i})\right] + \frac{\partial}{\partial x_j}(-\rho\overline{u_i^{'}u_j^{'}}) \tag{3.15}$$

Reynolds-averaged Navier-Stokes (RANS) equations are Eq. 3.14 and Eq. 3.15. They have the same general structure as the instantaneous Navier-Stokes equations, except that the velocities and other solution variables are now ensemble averaged (or time-averaged). Additional terminology that depicts the consequences of turbulence has now appeared. These Reynolds stresses, $-\rho\overline{u_i^{'}u_j^{'}}$, must be modeled to close Eq. 3.15.

### 3.1.5 Shear-stress transport (SST) $k-\omega$ turbulence model

The SST $k-\omega$ model includes all refinements of the baseline (BSL) $k-\omega$ model and in addition accounts for the transport of the turbulence shear stress in the definition of turbulent viscosity. These features make the SST $k-\omega$ model [104] [105] more accurate and reliable for a wider class of flows (for example, adverse pressure gradient flows, airfoils, transonic shock waves) than the standard and BSL $k-\omega$ model.

**Modeling turbulent viscosity**

The previously stated BSL model incorporates the benefits of the Wilcox [106] and $k-\omega$ model, however, it still fails to accurately anticipate the beginning and magnitude of flow separation from smooth surfaces. The fundamental problem is that neither model considers a turbulent shear stress transmission. As a result, the eddy-viscosity is overestimated. A limiter to the formulation of the eddy-viscosity can be used to attain the right transport behaviour:

$$\mu_t = \frac{\rho k}{\omega}\frac{1}{max\left[\frac{1}{\alpha^*}, \frac{SF_2}{a_{1,\omega}}\right]} \tag{3.16}$$

where $S$ is the strain rate magnitude and $F_2$ is shown:

$$F_2 = tanh(\phi_2) \tag{3.17}$$

$$\phi_2 = max\left[2\frac{\sqrt{k}}{0.09\omega y}, \frac{500\mu}{\rho y^2 \omega}\right] \tag{3.18}$$

where $y$ is the distance to the next surface. The coefficient $\alpha^*$ in Eq. 3.16 reduces turbulent viscosity, resulting in a low Reynolds number correction. It is provided by:

$$\alpha^* = \alpha^*_\infty(\frac{\alpha^*_0 + Re_t/R_k}{1 + Re_t/R_k}) \tag{3.19}$$

where

$$Re_t = \frac{\rho k}{\mu\omega} \tag{3.20}$$

$$R_k = 6 \tag{3.21}$$

$$\alpha^*_0 = \frac{\beta_i}{3} \tag{3.22}$$

$$\beta_i = 0.072 \tag{3.23}$$

For the high Reynolds number $k - \omega$ model, $\alpha^* = \alpha^*_\infty = 1$.

**Model constants**

This model has constant values as follows:

- $\sigma_{k,1} = 1.176,\ \sigma_{\omega,1} = 2.0,\ \sigma_{k,2} = 1.0,\ \sigma_{\omega,2} = 1.168$
- $\alpha_1 = 0.31,\ \beta_{i,1} = 0.075,\ \beta_{i,2} = 0.0828$
- $\alpha^*_\infty = 1.0,\ \alpha_\infty = 0.52,\ \alpha_0 = \frac{1}{9},\ \beta^*_\infty = 0.09$
- $R_\beta = 8.0,\ R_k = 6.0,\ R_\omega = 2.95,\ \zeta^* = 1.5,\ M_{t0} = 0.25$

**Wall boundary conditions**

In the $k - \omega$ model, the wall boundary conditions for the $k$ equation are addressed in the same manner as the $k$ equation is treated when improved wall treatments are employed with the $k - \epsilon$ model. This means that for wall-function meshes, all boundary conditions

will correspond to the wall-function approach, but for fine meshes, the appropriate low-Reynolds number boundary conditions will be used. Ansys Fluent software specifies the value of at the wall as follows [104]:

$$\omega_w = \frac{\rho(u^*)^2}{\mu}\omega^+ \tag{3.24}$$

Analytical solutions can be given first for the laminar sublayer:

$$\omega^+ = \frac{6}{\beta_i(y^+)^2} \tag{3.25}$$

and next for the logarithmic region:

$$\omega^+ = \frac{1}{\sqrt{\beta^*_\infty}}\frac{du^+_{turb}}{dy^+} \tag{3.26}$$

As a result, a wall treatment for the $\omega$ equation may be created, which shifts automatically from the viscous sublayer formulation to the wall function depending on the grid. This blending was adjusted with Couette flow to achieve a grid-independent solution of the skin friction value and wall heat transfer. This better blending is the near-wall treatment's default behavior.

## 3.2 Assumption of the CFD simulation

A series of CFD simulations of air-side flow and heat transfer in three dimensions at steady state were carried out for the following data:

- Method 1: Constant temperature of the fin surface and constant temperature of the external surfaces of tubes: 70 $°C$.
- Method 2: Constant temperature of the fin base and constant temperature of the external surfaces of tubes: 70 $°C$.
- Method 3: Constant temperature of the fluid free flow: 70 $°C$ and known heat transfer coefficient on the inner side of the tube: 1300 $\frac{W}{m^2K}$ [90].
- the constant air inlet temperature: 20 $°C$.
- air velocity in front of the heat exchanger is uniform; simulations were carried out in the following range of air changes: 0.5 $m/s \leq w_0 \leq$ 10 $m/s$.
- There is a thermal resistance between the base of the fin and the outer surface of the tube that contributes to reducing the heat flux of the heat exchanger from water to air: $R_{tr}$ = 3.17E-05 $\frac{m^2K}{W}$ [107].

- Mass average temperature control in the outlet area with the Ansys Fluent opening boundary condition setup (the open boundary condition is a design boundary that allows phenomena generated in the flowing fluid to pass through the outlet surface without distortion and without affecting the internal solution [108]).
- The physical properties of air are temperature-dependent.
- For modeling flow and heat transfer on the air-side, the governing equations or conservation equations of mass, momentum, and energy, given in (chapter 3.1), were applied [104].
- The $k - \omega$ Shear Stress Transport ($k - \omega\ SST$) turbulence model was used [105].
- The residuals were set to less than $10^{-4}$ for the continuity equations and $10^{-6}$ for the velocities in each direction and the energy equations.
- Ansys Fluent 2022 software was used to perform the simulations [104].

## 3.3 Determination of the air-side Reynolds number

Other subsections will be devoted to the methods for determining heat transfer correlations on the air-side based on the results of CFD simulations. The following will show how the maximum flow velocity in the exchanger is calculated. The maximum air velocity is used to calculate the air-side Reynolds number, which is found in the correlations on the Nusselt number, determined on the basis of computer simulation results.

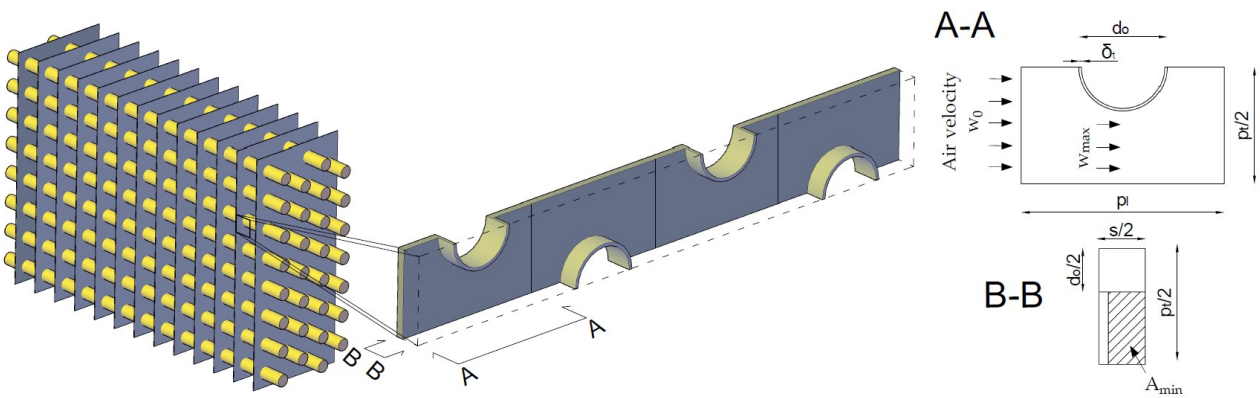


Figure 3.1: Schematic of the diagram showing the location of air maximum velocity and air minimum cross-sectional area.

The hydraulic diameter $d_h$, which is derived using the definition offered by Kays and London [1], and the maximum air velocity $w_{max}$ in the smallest cross-sectional area $A_{min}$ are the foundation of the mathematical model. To divide the volume through which air flows in a single row (Eq. 3.28) by the surface area in contact with the air (Eq. 3.29),

the hydraulic diameter (Eq. 3.27) has been obtained. All the basic dimensions needed to determine the hydraulic diameter and maximum speed are shown in Fig. 3.1.

$$d_h = \frac{4V_o}{A} \tag{3.27}$$

$$V_o = V_a - V_t \tag{3.28}$$

$$A = A_f + A_t \tag{3.29}$$

The volume through which air flows in a single row is denoted by the symbol $V_o$. Total area in a single row is represented by the letter $A$. Other symbols stand for: $V_a$ is the overall volume of a row, $V_t$ is the volume of tubes in one row, $A_f$ is the area occupied by the fins in one fin pitch, and $A_t$ is the area of the bare tubes in a row between the two fins directly above it.

$$V_a = p_l p_t (s - \delta_f) \tag{3.30}$$

$$V_t = \pi (\frac{d_o}{2})^2 (s - \delta_f) \tag{3.31}$$

$$A_f = 2 \left[ p_l p_t - \pi (\frac{d_o}{2})^2 \right] \tag{3.32}$$

$$A_t = \pi d_o (s - \delta_f) \tag{3.33}$$

The transverse fin pitch is designated by the letter $p_t$, while the longitudinal fin pitch is indicated by the character $p_l$. Other symbols represent: $s$ the fin pitch, $\delta_f$ the fin thickness, $d_o$ the tube's outer diameter. Eq. 3.34 shows Eq. 3.27 in its form, including Eqs. 3.30 -3.33. The hydraulic diameter in the case of PFTHE is equal to 5.35 mm and typically has a slightly lower pitch than the double fin using the geometry from 3.1.

$$d_h = \frac{4(s - \delta_f)(p_l p_t - \pi(\frac{d_o}{2})^2)}{2\left[p_l p_t - \pi(\frac{d_o}{2})^2\right]) + (\pi d_o)(s - \delta_f)} \tag{3.34}$$

Eq. 3.35 shows the calculation of $w_{max}$. The parameter $w_{max}$, which has been determined for the minimal airflow cross-section between tubes [1], may exist in a different location in the case of varied PFTHE construction (Fig. 3.1).

$$w_{max} = \frac{(sp_l)}{(s - \delta_f)(p_l - d_{o,min})} \frac{\overline{T}_a^i}{\overline{T}_{a,0}} w_0 \tag{3.35}$$

The air velocity in the smallest cross-section of the airflow is represented by the symbol $w_{max}$. Other symbols are shown: $d_{o,min}$ the minimum distance between tubes, $\overline{T}_{0,a}$ the average air temperature of the inlet mass, $\overline{T}_a^i$ the average air temperature of the mass in the $i$-th row of the PFTHE, and $w_0$ the air velocity in front of the PFTHE.

Using the hydraulic diameter ($d_h$) (Eq. (3.34)) and the maximum air velocities ($w_{max}$) (Eq. (3.35)) for each row independently, Reynolds numbers ($Re_a$) (Eq. (3.36)) [3] were determined.

$$Re_a = \frac{w_{max} d_h}{\nu_a} \tag{3.36}$$

Eq. (3.36) uses the following symbols: $d_h$ the hydraulic diameter of the air and $\nu_a$ the kinematic viscosity of the air.

## 3.4 CFD model, geometry and boundary conditions

The materials and dimensions of the simulated PFTHE are shown in Tab. 3.1. The heat exchanger was obtained from the PFTHE Kelvion manufacturer's website [109]. The PFTHE has a fin pitch of 3 mm ($s$). However, only a value of less than half of the total space between the fins occurs in the width of the modeled airflow. Half the distance between the fins: 1.5 mm ($0.5s$), must be further reduced by the thickness of half the fins: 0.07 mm ($0.5s - 0.5\delta_f$). The result is the width of the modeled distance of 1.43 mm. The air symmetry from the third direction permits the following simplifications: top, bottom, and side. The tubes' outside diameter ($d_o$) is 12 mm and tube wall thickness ($\delta_t$) is 0.35 mm. The transverse tube pitch ($p_t$) is 32 mm. However, because of air symmetry, the height of the simulated volume is equal to 0.5 $p_t$ and equals 16 mm. The length of each row ($L_r$) is the same as the longitudinal tube pitch ($p_l$), which is 27.71 mm.

| **Description** | **Designation** | **Value** |
|---|---|---|
| Rows | $R$ | 4 |
| Transversal tube pitch | $p_t$ | 32 mm |
| Longitudinal tube pitch | $p_l$ | 27.71 mm |
| Tube outer diameter | $d_o$ | 12 mm |
| Tube wall thickness | $\delta_t$ | 0.35 mm |
| Fin pitch | $s$ | 3 mm |
| Fin thickness | $\delta_f$ | 0.14 mm |
| Fin length of single row | $L_r$ | 27.71 mm |

Table 3.1: Dimensions of the modelled PFTHE [109].

In the examined PFTHE, shows a repeating air segment between one fin pitch for method 1, method 2, and method 3 (Fig. 3.2). The expanded inlet and outflow zones shown in the above figures are also required for a proper model of the upstream and

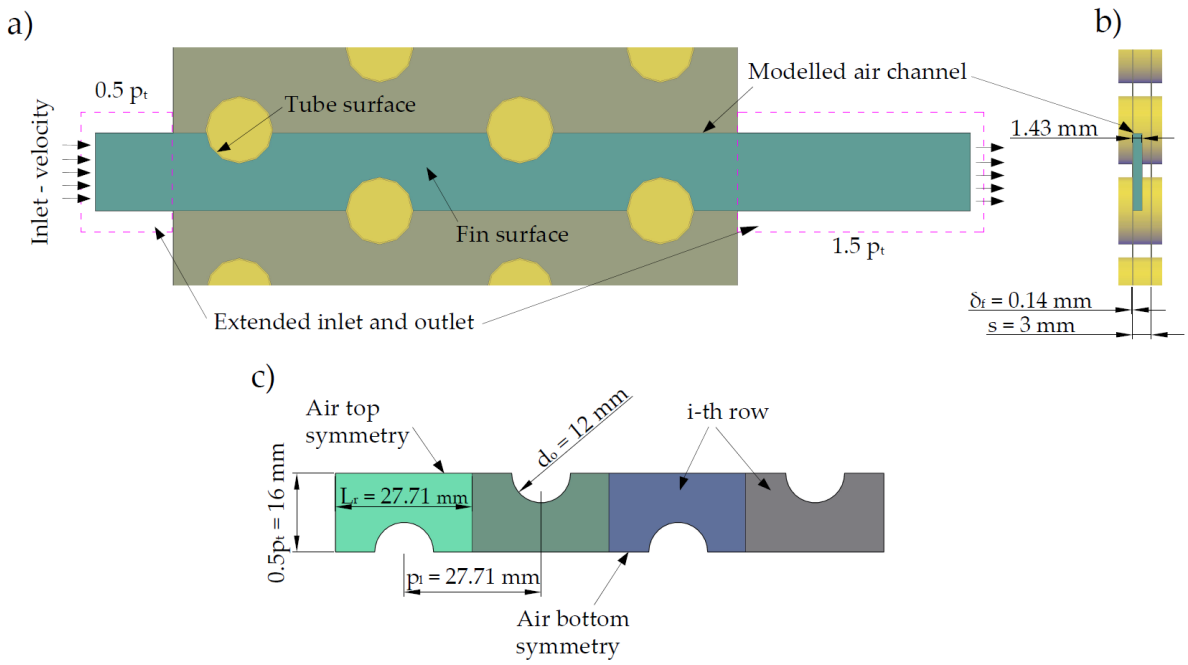


Figure 3.2: a) Repeatable section of the PFTHE: modeled air channel, and boundary conditions. b) Cross-section of the modeled air channel - dimensions. c) Fin and tube geometry characteristics.

downstream temperature and pressure fields [92]. The extended inlet and outlet zones are presented in numerous studies that display CFD modeling findings. However, depending on the zones extended to various characteristics like the tube's outer dimension ($d_o$) [92], fin spacing ($s$), and longitudinal tube pitch ($p_l$) [110], as well as the height of the channel (0.5 $p_t$) [30] and the length of the tube bank (flow length) [111][112]. The intake zone in this research is equal to 0.5 $p_t$ = 16 mm, while the outflow zone is equal to 1.5 $p_t$ = 48 mm, where the four-row tube bank measures 110.84 mm.

Fig. 3.3 geometry of all methods displays Ansys Fluent software boundary conditions [104], modeled geometry, main simulation assumptions and heat exchanger thermal resistance model for each method. The symbols are used in the figure describe: $T_a$ means air temperature, $T_{wall}$ denotes fin and tubes wall temperature, $T_{fl}$ is the free flow fluid temperature, $R_{\alpha,a}$ is thermal heat transfer resistance from the outside surface of the tubes and fin, $R_{\lambda,f}$ is thermal heat conduction resistance of the fin, $R_{\lambda,ft}$ is thermal heat conduction resistance of the tubes and fin, $R_{\alpha,w}$ is thermal heat transfer resistance from the inside surface of the tubes. The temperature of the air inlet is kept constant at 20 $°C$ with verification mass average temperature in the air outlet cross-section, the air outlet is set as an opening condition [108]. The modeled air zone has top, bottom, and side symmetry conditions. On the surface opposite to the air symmetry side (the fin surface), wall boundary conditions are set.

The temperature in this fin wall remained constant at 70 $°C$. On the tube surfaces, the

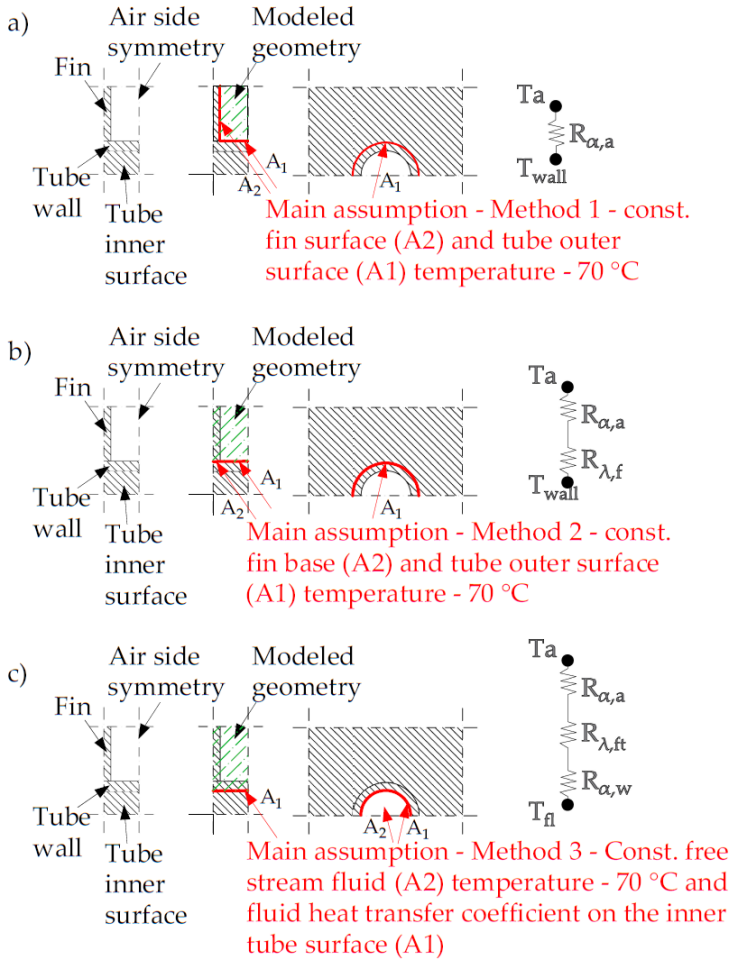


Figure 3.3: Cross-section with the main assumption of the method, and thermal resistance model depicting the heat exchanger thermal operation for: a) method 1, b) method 2, c) method 3.

same conditions and consistent temperature are established. The same conditions with the same constant temperature were set on the tube surfaces. The different constant temperatures of the surface of the fin and tube in the range of 60 $°C$ to 80 $°C$ cause a slight discrepancy, less than 1.6 % compared to the constant temperature: 70 $°C$ [93]. The proposed conditions are universal, and they can be used in water-to-air finned heat exchange where there is heat exchange between fluids and gasses, and also in an evaporator or condenser where there is a constant temperature of phase transition and on the other side of the tube changing the temperature of fluid or gas, which is most commonly used in air heat pumps or air conditioning.

In the present work, the heat transfer coefficients and Nusselt number on the air-side of the individual tube rows and on the entire exchanger were determined using the 3 methods described in subsection 3.2. Method 2 and Method 3 were tested, which considered the same heat exchanger geometry as in Method 1, and thus the repeatable section of the exchanger was identical. All the methods were based on a representative and repeatable

section of the exchanger with a width of one fin pitch ($s$) and a height of half the transverse pitch of the exchanger ($p_t$). The methods differed by assuming different thermal boundary conditions on the surface of tubes and fins, as mentioned above.

## 3.5 Mesh parameters and mesh independent study

Fig. 3.4, Fig. 3.5 and Fig. 3.6, respectively for method 1, 2 and 3 show the repeated portion of the modeled PFTHE with a finite volume mesh. For better distribution into equal pieces, the mesh has been split into several volumes (different colors in Fig 3.4 - Fig 3.6). The mesh has been compacted at the surfaces of the fins and tubes (compaction in zoom-in windows). Because of the prolonged and slanted elements, the regularity of the volumes is disturbed in the compaction zone. However, the volume distortion is within acceptable bounds. Method 1, method 2, and method 3 represent a particular value of 35.6 °, 35.5 ° and 32.4 ° as the smallest orthogonal angle. The highest aspect ratio is 22, 76, and 45, and the mesh expansion factor is 22, 14, and 19 [113].

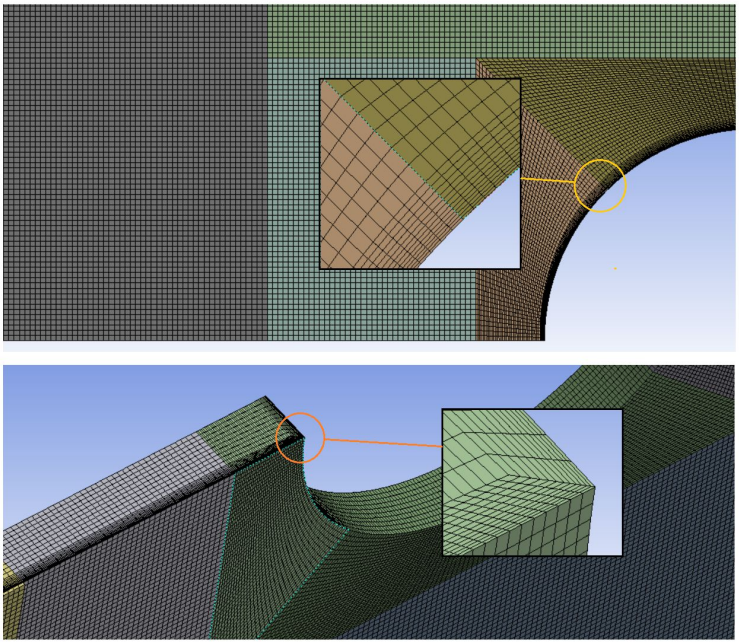

Figure 3.4: Repeatable fragment of the PFTHE with finite volume mesh for method 1.

Data for the computation mesh are shown in Tab. 3.2. The cuboid and quadrilateral elements make up the calculating mesh. Moreover, it has densities at the interface between the air and the fins, and tubes to improve the simulation accuracy. Densities are calculated using a first layer thickness equal to 0.035 mm with a growth rate of 1.1 and 12 layers for method 1 and 8 layers for methods 2 and 3.

Each air velocity in the complete spectrum of CFD simulations was individually subjected to mesh-independent investigation individually (Fig. 3.7, Fig. 3.8 and Fig. 3.9).

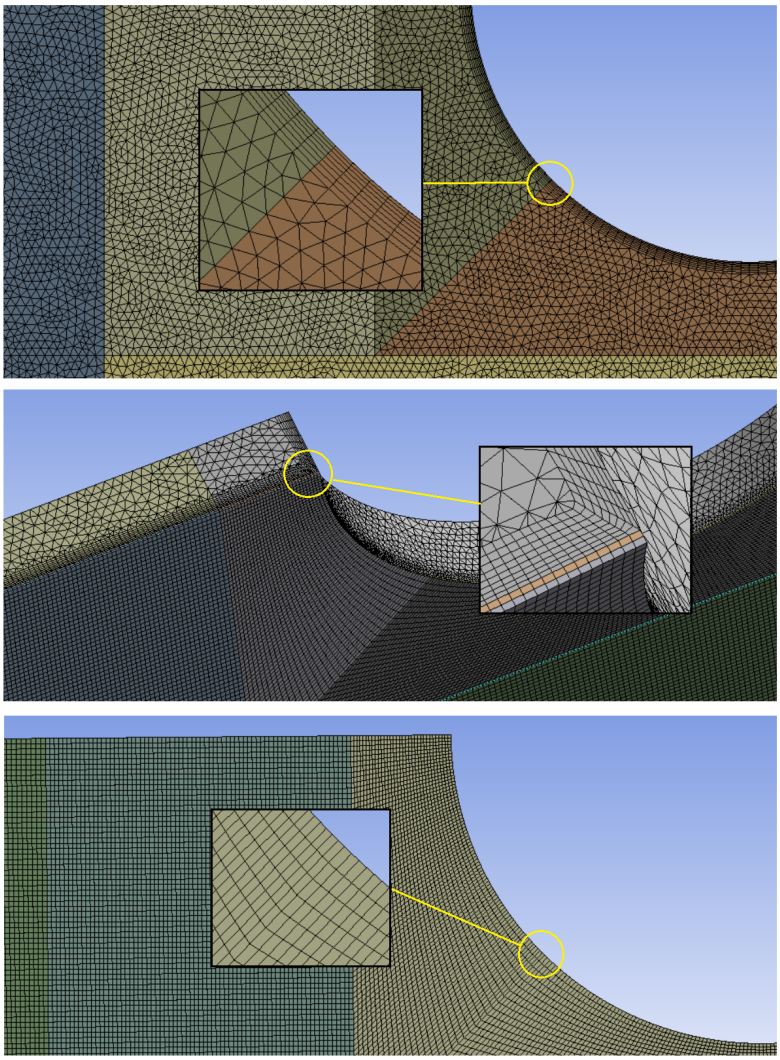

Figure 3.5: Repeatable fragment of the PFTHE with finite volume mesh for method 2.

| Mesh parameter | Method 1 | Method 2 | Method 3 |
|---|---|---|---|
| Finite element number, - | 3,104,268 | 7,252,330 | 11,332,752 |
| Number of nodes, - | 3,277,429 | 2,781,776 | 4,930,446 |
| Dimension of the air element, mm | 0.15 | 0.18 | 0.16 |
| Maximum dimension of the air element, mm | 0.20 | 0.21 | 0.21 |
| Dimension of the fin element, mm | - | 0.09 | 0.09 |
| First layer thickness, mm ($y^+ = 1$) | 0.023 | 0.023 | 0.023 |
| Growth rate, - | 1.1 | 1.1 | 1.1 |
| Number of layers, - | 12 | 8 | 8 |
| Minimum orthogonal angle (<1 % elements) | 35.6° | 35.5° | 32.4° |
| Mesh expansion factor (<1 % elements) | 14 | 76 | 45 |
| Maximum aspect ratio (<1 % elements) | 22 | 14 | 19 |

Table 3.2: Mesh data of the modelled part of the heat exchanger for methods 1, 2 and 3.

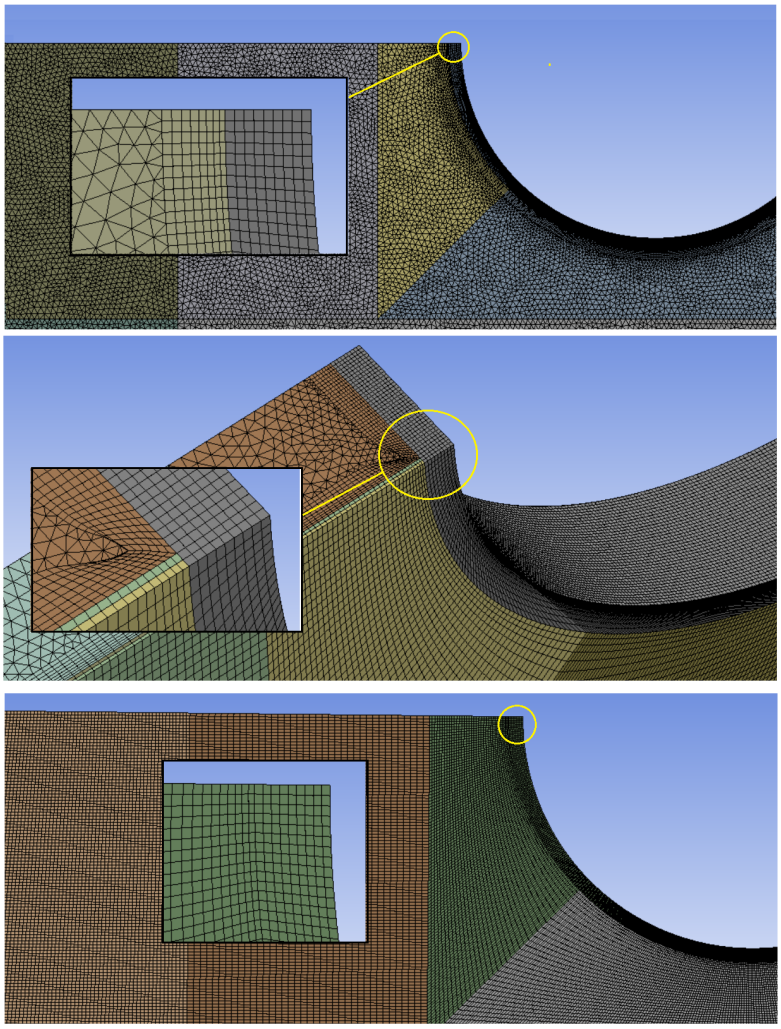

Figure 3.6: Repeatable fragment of the PFTHE with finite volume mesh for method 3.

Calculating the relative differences ($e_{Nu}$)(Eq. 3.37) between various Nusselt numbers in the fourth row of PFTHE for meshes with specific element numbers ($Nu_{ni}$) and the reference Nusselt numbers in the fourth row of PFTHE for meshes with 3,104,268 mesh elements ($Nu_{ref}$) for method 1, 7,252,330 mesh elements for method 2 and 11,332,752 mesh elements for method 3 resulted in the designation of Nusselt number stabilization, which is as follows:

$$e_{Nu} = \frac{(Nu_{ni} - Nu_{ref})}{Nu_{ref}} \tag{3.37}$$

Fig. 3.7, Fig. 3.8, and Fig. 3.9 illustrate the stabilization of the Nusselt number at an air velocity of 10 m/s in front of the heat exchanger for the fourth row of PFTHE. The stabilization of the Nusselt number has been achieved for a mesh of 3,104,268 elements for method 1, 7,252,330 for method 2, and 11,332,752 for method 3. The relative differences for the mesh with the largest number of elements differ by less than 1.6 % for method 1, 1.12 % for method 2, and 1.6 % for method 3, and further increasing the

mesh elements does not produce results that are considerably different. The differences between the lower air velocities and other rows of PFTHE are even very near zero. This demonstrates that the last row of PFTHE experiences the most irregularity and turbulence flow in the scenario under consideration.

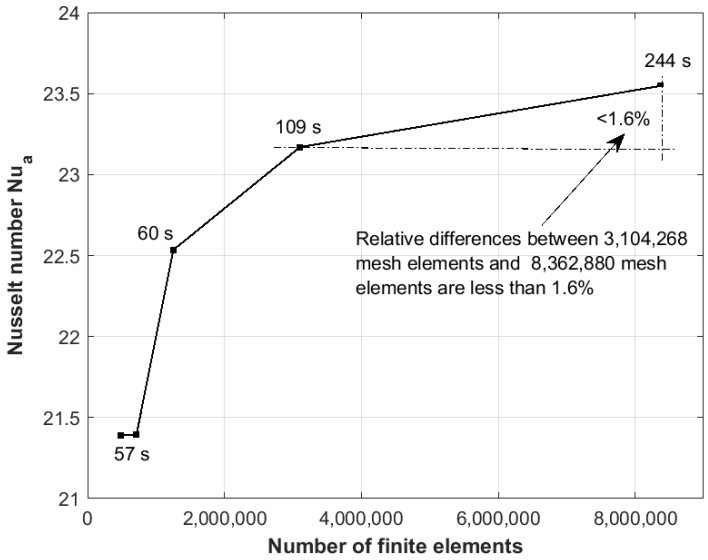


Figure 3.7: Nusselt number stabilization for mesh independent investigation for 10 $m/s$ air velocity in front of the heat exchanger from the fourth row of PFTHE for method 1.

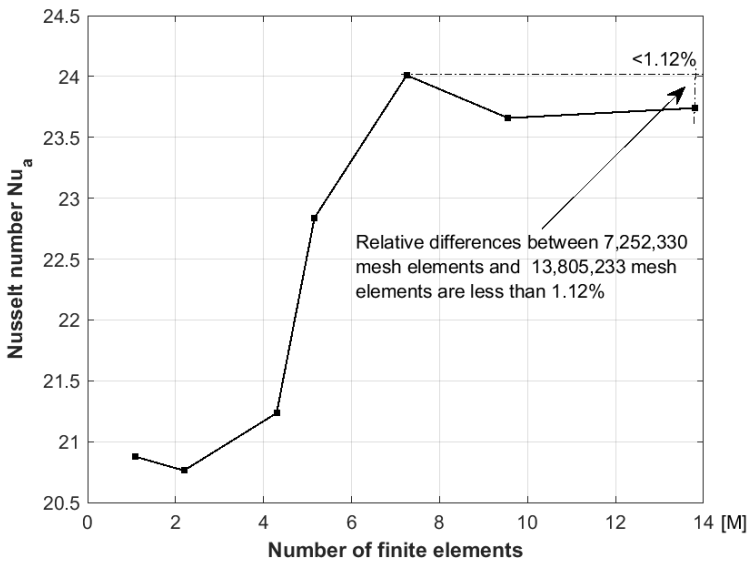


Figure 3.8: Nusselt number stabilization for mesh independent investigation for 10 $m/s$ air velocity in front of the heat exchanger from the fourth row of PFTHE for method 2.

In Fig. 3.7, the calculation time is also displayed. It can be seen that the chosen mesh takes more than twice as long to calculate as the mesh with the most components. The

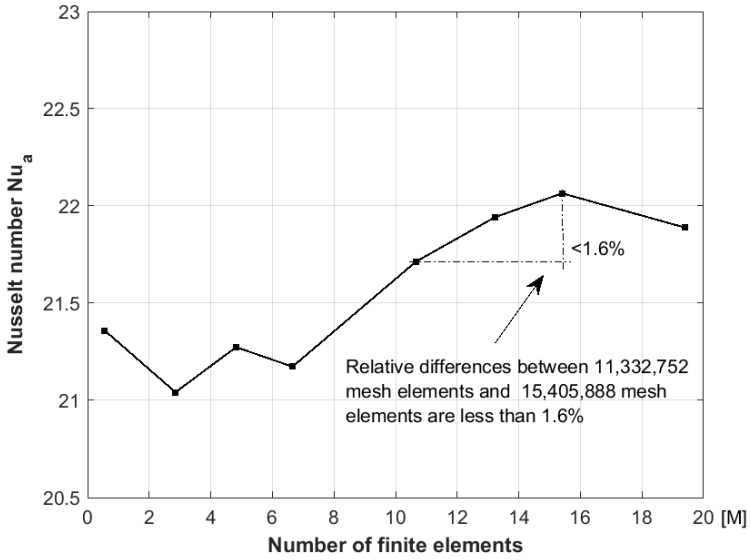


Figure 3.9: Nusselt number stabilization for mesh independent investigation for 10 $m/s$ air velocity in front of the heat exchanger from the fourth row of PFTHE for method 3.

reference mesh mentioned above was chosen for additional calculations since it offers the best performance in terms of accuracy to processing time. 3,104,268 parts compose the chosen mesh. The following mesh sizes make up the size of the mesh elements: 0.15 mm mesh element size 0.20 mm mesh maximum (Tab. 3.2). There are just cuboidal pieces in the entire mesh (Fig. 3.4). Also, for further computations, the reference mesh for methods 2 and 3 was chosen since it provides the best performance in terms of accuracy to processing time. The selected mesh comprises 7,252,330 sections for method 2 and 11,332,752 parts for method 3. The mesh elements are made up of the following mesh sizes: for method 2, the mesh elements are 0.18 mm in size and 0.21 mm in maximum, while for method 3, the mesh elements are 0.16 mm in size and 0.21 mm in maximum (Tab. 3.2). For methods 2 and 3, the complete mesh is made up of quadrilateral pieces (Fig. 3.5 and Fig. 3.6).

## 3.6 Procedure for Determining Air-side Nusselt Number on Individual Tube Rows

The doctoral dissertation presents three different methods for determining the average air-side heat transfer coefficients. Knowledge of the average value of the heat transfer coefficient on the air-side is necessary to determine power correlations on the Nusselt number on the air-side. The local heat transfer coefficient is determined on the basis of the temperature and heat flux density at a given point on the tube or fin surface and the mass average air temperature in the area adjacent to the analyzed point. To date, there is no procedure for determining the average heat transfer coefficient for a given row of tubes

for the entire exchanger or a particular row of tubes due to the difficulties in determining the average mass air temperature. All methods are compatible with the experimental determination of Reynolds number and Nusselt number, due to which Nusselt number correlations determined from the air-side can be compared with Nusselt number correlations determined on the basis of CFD simulations.

### 3.6.1 Method 1 - assuming equal temperatures on the surface of the tubes and fins

The average heat transfer coefficient $\alpha_{a,i}$ on a given tube row is determined assuming that the temperature $T_{wall}$ of the fins and tube walls are constant. At the inlet of the $i$-th control volume (row), the air temperature is $\overline{T}_a^i$. To determine the temperature distribution along the analyzed control volume, the heat balance equation for the flowing air (Fig. 3.38) will be written for the $i$-th control volume of the width $\Delta y$.

Determining the HTC and Nusselt number of a given row is done as follows:

- Taking the average mass flow temperature at the outlet $\overline{T}_a^{i+1}$ for each row independently from the Fluent Post-Processor. Between the following two tubes, in succession, there are areas where the average mass flow temperatures can be extracted (Fig. 3.10).

- Use Eq. (3.60) to obtain the logarithmic average temperature differential ($\Delta\overline{T}^i m, a$) between the surface temperatures of the fin and tube ($T_{wall}$) and the average mass flow temperature at the inlet ($\overline{T}_a^i$) of the particular row. To determine the logarithmic mean value of the temperature difference, began by deriving the differential equation of the energy balance.

$$\dot{m}_{a,i} h_a|_y + \alpha_{a,i} \Delta y U_{ca} (T_{wall} - T_a) = \dot{m}_{a,i} h_a|_{y+\Delta y} \tag{3.38}$$

  where $h$ is the enthalpy of the air in front of $h|_y$ and behind $h|_{y+\Delta y}$ the control area. $U_{ca}$ is the perimeter of the airflow cross-section area, $\Delta y$ is the width of the control volume. $T_{wall}$ and $T_a$ mean the temperature of the fin and tube wall and air temperature for a particular distance inside the control volume, respectively. The air mass flux $\dot{m}_a$ flow through the control area with cross-section $A_{m,a}$ is given by the formula (Fig. 3.10):

$$\dot{m}_a = A_{m,a} \overline{w}_{a,i} \rho_{a,i} = A_{m,a} \frac{1}{BH} \overline{w}_{a,0} \rho_{a,0} \tag{3.39}$$

  where the control area with cross-section $A_{m,a}$ is given by (Fig. 3.10):

$$A_{m,a} = \frac{p_t}{2} \frac{(s - \delta_f)}{2} \tag{3.40}$$

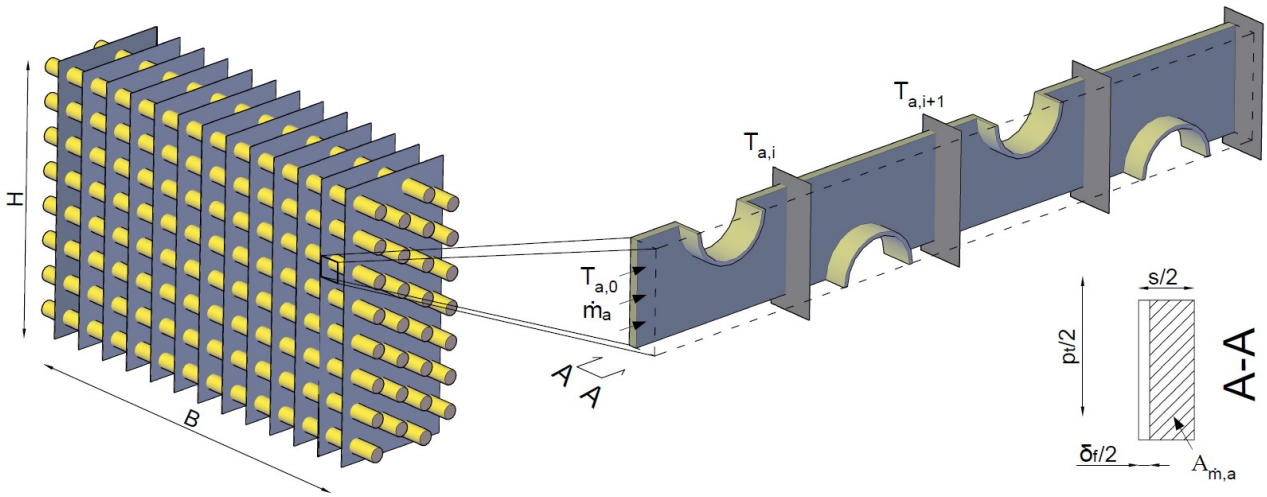


Figure 3.10: Schema of the air mass flow, air mass flow area, and mass average air temperature for $i$-th of the control volume.

Eq. 3.38 after transformations can be written:

$$\dot{m}_{a,i}\frac{h_a|_{y+\Delta y} - h_a|_y}{\Delta y} = \alpha_{a,i}U_{ca}(T_{wall} - T_a) \tag{3.41}$$

If $\Delta y \to 0$, Eq. 3.41 takes the form:

$$\dot{m}\frac{dh_a}{dy} = \alpha_{a,i}U_{ca}(T_{wall} - T_a) \tag{3.42}$$

After considering that:

$$\frac{dh_a}{dy} = \frac{dh_a}{dT}\frac{dT}{dy} = c_{p,a}\frac{dT}{dy} \tag{3.43}$$

From Eq. 3.42, the following equation is obtained:

$$\dot{m}_{a,i}c_{p,a}\frac{dT}{dy} = \alpha_{a,i}U_{ca}(T_{wall} - T_a) \tag{3.44}$$

After separating the variables and considering that $dT = d(T_{wall} - T_a)$:

$$\dot{m}_{a,i}c_{p,a}\frac{d(T_{wall} - T_a)}{(T_{wall} - T_a)} = -\alpha_{a,i}U_{ca}dy \tag{3.45}$$

After dividing both sides by $\dot{m}_{a,i}c_{p,a}$ and integrating, the next equation is obtained:

$$ln(T_{wall} - T_a) = -\frac{\alpha_{a,i}U_{ca}dy}{\dot{m}_{a,i}c_{p,a}} \tag{3.46}$$

$$T_{wall} - T_a = e^{(-\frac{\alpha_{a,i}U_{ca}}{\dot{m}_{a,i}c_{p,a}}y + C)} = C_1 e^{-\frac{\alpha_{a,i}U_{ca}}{\dot{m}_{a,i}c_{p,a}}y} \tag{3.47}$$

where $C_1 = e^C$. The constant $C_1$ is determined from the boundary condition $T|_{y=0} = T_1$, where $T_1$ is the given air temperature at the entry to the control volume. After substituting the above boundary condition into Eq. 3.47 is obtained:

$$T_1 = T_{wall} - C_1 e^{-\frac{\alpha_{a,i} U_{ca}}{\dot{m}_{a,i} c_{p,a}} 0} \tag{3.48}$$

From where the following equation is obtained:

$$C_1 = T_{wall} - T_1 \tag{3.49}$$

After substituting $C1$ into Eq. 3.47:

$$T_{a,y} = T_{wall} - (T_{wall} - T_1) e^{-\frac{\alpha_{a,i} U_{ca}}{\dot{m}_{a,i} c_{p,a}} y} \tag{3.50}$$

Eq. 3.50 allows determining the air temperature along the length of the control area for any y-coordinate. The air temperature at exit $T_2$ of the control area $y = L$ is:

$$T_2 = T_{wall} - (T_{wall} - T_1) e^{-\frac{\alpha_{a,i} U_{ca}}{\dot{m}_{a,i} c_{p,a}} L} \tag{3.51}$$

Given that $U_{ca} L = A$, Eq. 3.51 takes the form:

$$T_2 = T_{wall} - (T_{wall} - T_1) e^{-\frac{\alpha_{a,i} A}{\dot{m}_{a,i} c_{p,a}}} \tag{3.52}$$

where $A$ is the area of the heat transfer surface. If air flows through a channel with a constant cross-sectional area, $U_{ca} L = A$ can be assumed in equation (2.51). In the case of the exchanger under study, the shape of the channel is more complex. Taking into account the symmetry conditions, only 1/4 of the volume of the modeled area is analyzed. Therefore, in the formula for the area of the heat transfer area, 1/4 of the area of the tube and 1/4 of the area of the fin are considered. In method 1, $A = \frac{1}{2}\left[\pi d_o \frac{(s-\delta_f)}{2} + (p_t p_l - \frac{\pi d_o^2}{2})\right]$ (Fig. 3.11). In methods 2 and 3, the heat transfer coefficient from the air-side reduced to the outer surface of the tube $A_{=}\frac{1}{4}\pi d_o s$ was introduced.

The heat flux transferred through the fin and tube walls at a constant temperature to the air in the control volume can be determined as the product of the area at the boundary of the control area $A$, the heat transfer coefficient from the air-side $\alpha_{a,i}$ and the logarithmic average temperature $\Delta T_{ma,i}$ difference between the wall temperature $T_{wall}$ and the air temperature inside the control volume $T_a$. For this purpose, the difference in the outlet temperature of the control area $T_2$ and the wall temperature $T_{wall}$ is written in a dimensionless form. From Eq. 3.51 is obtained:

$$\frac{T_{wall} - T_2}{T_{wall} - T_1} = e^{-\frac{\alpha_{a,i} A}{\dot{m}_{a,i} c_{p,a}}} \tag{3.53}$$

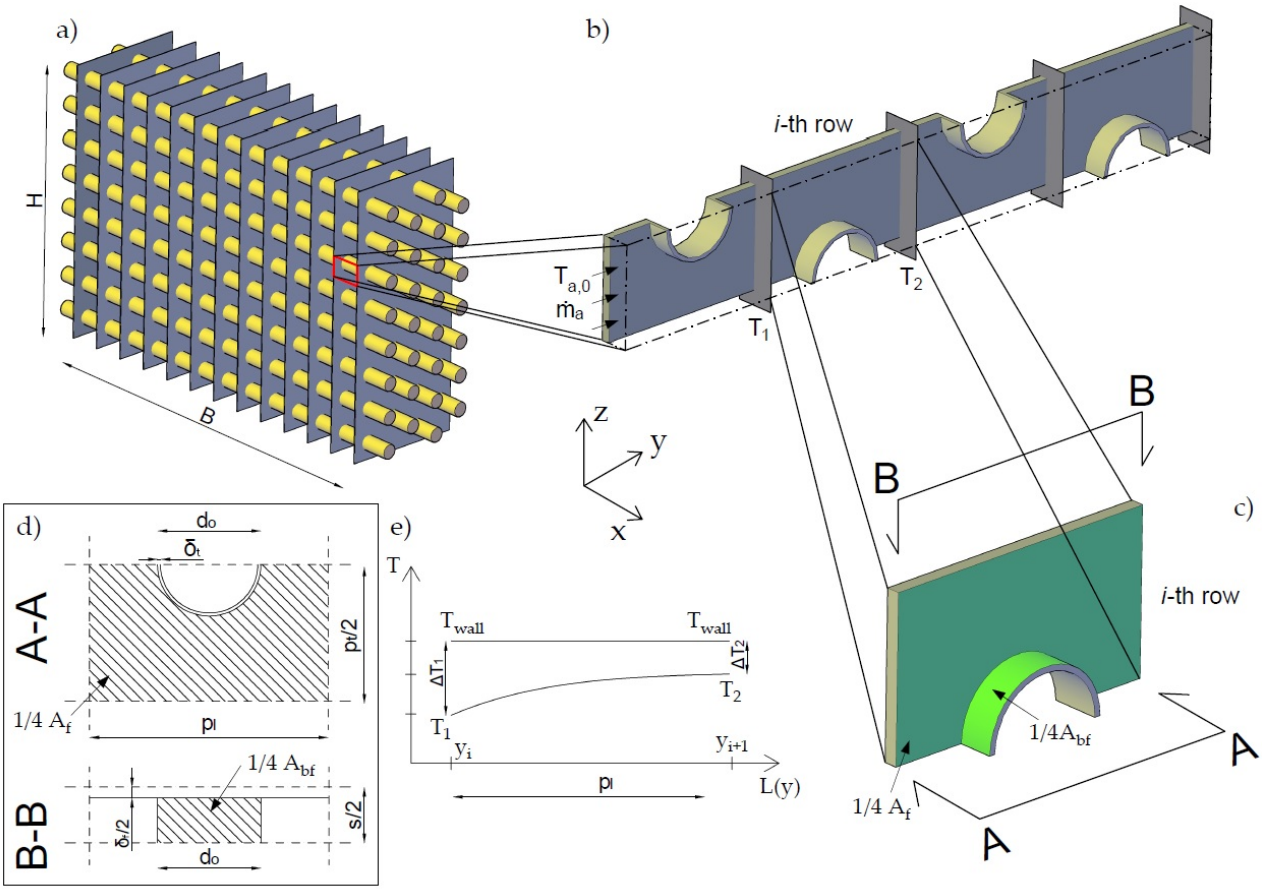


Figure 3.11: a) The entire heat exchanger view, with a section of the control volume marked. b) Model of control volume with marked dividing planes between rows. c) View of one row; d) Cross-sections of one row. e) Schematic diagram showing heating of air over the length of one row.

After logarithmization, we obtain:

$$ln\frac{T_{wall} - T_2}{T_{wall} - T_1} = -\frac{\alpha_{a,i}A}{\dot{m}_{a,i}c_{p,a}} \tag{3.54}$$

In addition, after considering:

$$\dot{m}_{a,i}c_{p,a} = \frac{\dot{Q}_a}{T_2 - T_1} \tag{3.55}$$

And the substitution of Eq. 3.55 to Eq. 3.54 is obtained:

$$ln\frac{T_{wall} - T_2}{T_{wall} - T_1} = -\frac{\alpha_{a,i}A}{\dot{Q}_a}(T_2 - T_1) \tag{3.56}$$

Formula Eq. 3.56 can be written in the form:

$$ln\frac{T_{wall}-T_2}{T_{wall}-T_1}=\frac{\alpha_{a,i}A}{\dot{Q}_a}\left[(T_{wall}-T_2)-(T_{wall}-T_1)\right] \tag{3.57}$$

From the formula Eq. 3.56 one obtains $\dot{Q}_a$:

$$\dot{Q}_a=\alpha_{a,i}A\frac{\left[(T_{wall}-T_2)-(T_{wall}-T_1)\right]}{ln\frac{T_{wall}-T_2}{T_{wall}-T_1}}=\alpha_a A\Delta T_{m,a} \tag{3.58}$$

where the logarithmic mean temperature difference $\Delta T_{ma,i}$ is given by formula: $\dot{Q}_a$:

$$\Delta T_{m,a}=\frac{((T_{wall}-T_2)-(T_{wall}-T_1))}{ln(\frac{T_{wall}-T_2}{T_{wall}-T_1})}=\frac{\Delta T_2-\Delta T_1}{ln\frac{\Delta T_2}{\Delta T_1}} \tag{3.59}$$

where $\Delta T_1=T_{wall}-T_1$ and $\Delta T_2=T_{wall}-T_2$ (Fig. 3.11).

$$\Delta\overline{T}^i_{m,a}=\frac{(T_{wall}-\overline{T}^{i+1}_a)-(T_{wall}-\overline{T}^i_a)}{ln(\frac{T_{wall}-\overline{T}^{i+1}_a}{T_{wall}-\overline{T}^i_a})} \tag{3.60}$$

The constant surface temperature of fins and tubes is represented by the symbol $T_{wall}$. The mass average air temperatures of the entrance and exit for the $i$-th row of PFTHE are represented by the symbols $\overline{T}^i_a$ and $\overline{T}^{i+1}_a$.

- Generate the total heat flow ($\dot{Q}_a$) for the $i$-th row of the PFTHE from the fins and tube surfaces to the air.

- Use Eq. (3.62) to calculate the unique HTC for each row independently. From Eq. 3.58 written for the $i$-th control area, it is obtained:

$$\dot{Q}_a=\alpha_a A\Delta T_{m,a} \tag{3.61}$$

From Eq. 3.61, $\alpha^i_a$ is determined. The temperatures $T_2$ and $T_1$ are known from the CFD simulation.

$$\alpha^i_a=\frac{\dot{Q}^i_a}{A\Delta\overline{T}^i_{m,a}} \tag{3.62}$$

- Calculate the Nusselt number using Eq. (3.63).

$$Nu^i_a=\frac{\alpha^i_a d_h}{\lambda_a} \tag{3.63}$$

where $\lambda_a$ means air heat conduction.

### 3.6.2 Method 2 - assuming Uniform temperature on the outer surface of the tubes and at the base of the fins

Most of the parameters included in the methodology are identical to those of method 1 in subsection 3.6.1. Method 2 uses the same equation (Eq. 3.52), which takes into account the logarithmic average heating of the air from the hot tubes and fins.

$$T_2 = T_{wall} - (T_{wall} - T_1)e^{-\frac{\alpha_{a,i}A}{\dot{m}_{a,i}c_{p,a}}} \tag{3.64}$$

In addition, an equivalent heat transfer coefficient from the air-side is introduced that considers the presence of the fin on the tube. The equivalent heat transfer coefficient is defined as follows:

$$\alpha_{a,eq}A_o(T_{wall} - T_a) = \alpha_a A_{bf}(T_{wall} - T_1) + \alpha_a A_f(T_w - T_1)\eta_f \tag{3.65}$$

After dividing both sides of the equation by $A_o(T_w - T_a)$, one gets:

$$\alpha_{a,eq} = \alpha_a(\frac{A_{bf}}{A_o} + \frac{A_f}{A_o}\eta_f) \tag{3.66}$$

And:

$$A_o = \pi d_o s, \quad A_{bf} = \pi d_o(s - \delta_f), \quad A_f = 2p_t p_l - \frac{\pi d_o^2}{2} \tag{3.67}$$

where $A_o$ is the equivalent outer surface of the tube as if fins did not exist, $A_{bf}$ means the outer surface of the tube in one fin pitch $s$ (between fins) and $A_f$ is the surface of the fins in one fin pitch $s$ (Fig. 3.11). The reduced heat transfer coefficient $\alpha_{eq}$ is determined from the condition:

$$T_2^{calc} = T_2^{CFD} \tag{3.68}$$

where $T_2^{calc}$ is defined by the formula:

$$T_a^{CFD,i+1} = T_w^i - (T_w^i - T_a^{CFD,i})e^{-\frac{\alpha_{eq}^i A_o}{\dot{m}_a c_{p,a}}} \tag{3.69}$$

Using CFD modeling, temperatures at the outlet of $i$-th row of tubes $T_a^{CFD,i+1}$ are determined for a given air mass flow $m_a$. The heat transfer coefficient $\alpha_a$ from the air-side is determined using the sweep method so that Eq. 3.69 is satisfied.

$$\alpha_{a,j} = \frac{\alpha_{eq,j}}{\frac{A_{bf}}{A_o} + \frac{A_f}{A_o}\eta_f(\alpha_{a,j})}, \quad j = j, ..., n_{exp} \tag{3.70}$$

where $n_{exp}$ is the number of air velocities for which the CFD simulation was performed.

Instead of first determining $\alpha_{eq}$ from Eq. 3.68 and then determining $\alpha_a$ from Eq. 3.70, the procedure to determine $\alpha_a$ can be slightly simplified. First, substitute the expression $\alpha_{eq}$ defined by Eq. 3.66 into Eq. 3.69 and then use the interval search method to determine the value of $\alpha_a$ from Eq. 3.68

### 3.6.3 Method 3 - assuming Known Free Stream Fluid Temperature and Fluid Heat Transfer Coefficient on the inner tube surface

Method 3 presents the most accurate heat flow in a heat exchanger from hot water to cold air. The process uses constant temperatures in the free fluid flow inside the tube (70 $°C$) and a constant heat transfer coefficient on the water-side. The simulation also considered equal thermal resistance between the base of the fin and the outer surface of the tube, and equal: $R_{tc}$ = 3.17E-05 $\frac{m^2K}{W}$. The ability to assume a constant temperature in the free stream is due to the small differences in the outlet temperatures of individual rows. Furthermore, the effect of these row-by-row temperature differences on the air-side heat transfer coefficient is negligible, because the Prandtl numbers that vary for air do not change much [114]. The water-side heat transfer coefficients are equal in each row of tubes and are determined from the correlation [90] proposed by Taler and Taler as follows:

$$Nu_w = 0.01253 Re_w^{0.8413} Pr_w^{0.6179} \left[1 + (\frac{d_i}{L_x})^{2/3}\right] \quad 3000 \leq Re_w \leq 10^6 \quad 1 < Pr_w \leq 3 \tag{3.71}$$

$$Nu_w = 0.00881 Re_w^{0.8991} Pr_w^{0.3911} \left[1 + (\frac{d_i}{L_x})^{2/3}\right] \quad 3000 \leq Re_w \leq 10^6 \quad 3 < Pr_w \leq 1000 \tag{3.72}$$

The temperature increment on each row is recorded in the following

$$\Delta T_a^i = T_a^{i+1} - T_a^i \tag{3.73}$$

The symbol $\Delta T_a^i$ means the difference in the mass average air temperature between two adjacent rows, $T_a^{i+1}$ denotes the mass average air temperature in the inlet of the next row (or in the outlet of the $i$-th row) and $T_a^i$ is the mass average air temperature in the $i$-th row. The mass average temperatures were read using Ansys Fluent software using thermal resistance $R_t$ between copper tubes and aluminum fins. From another perspective, the temperatures in Eq. (3.73) could be determined by solving a differential equation describing air temperature distribution considering boundary conditions in front of the heat exchanger (Fig. 3.11).

$$\frac{dT_a(y)}{dy} = N_a^i[T_w - T_a^i(y)] \tag{3.74}$$

The symbol $N_a^i$ (Eq. (3.74)) means the number of heat exchange units for the air-side for a particular row of tubes.

$$N_a^i = \frac{U_o^i A_{eq}}{\dot{m}_a c_{p,a}} \tag{3.75}$$

In Eq. (3.74), the symbol $A_{eq}$ denotes the outer surface area of the bare tube without fins in one fin pitch. The symbol $\dot{m}_a$ means air mass flow per tube and $c_{p,a}$ air heat capacity. The overall heat transfer coefficient is shown below.

$$\frac{1}{U_o^i} = \frac{1}{\alpha_{eq}^i} + \frac{A_{eq}}{A_m}\frac{\delta_t}{\lambda_t} + \frac{A_{eq}}{A_{in}}\frac{1}{\alpha_w} \tag{3.76}$$

where $\alpha_{eq}^i$ the equivalent air-side heat transfer coefficient considering the fins attached to the tube, $A_{in}$ the area of the inner surface of the tube, $A_m = \frac{A_i + A_o}{2}$ the average area of the inner and outer surface of the tube $\delta_t$ the thickness of the wall of the tube, $\lambda_t$ the thermal conductivity of the tube material, $\alpha_w$ the water-side heat transfer coefficient. The equivalent air-side HTC in Eq. 3.77 $\alpha_{eq}$ is calculated using the mean HTC value in the entire row of the tube.

$$\alpha_{eq}^i = \alpha_a^i[\frac{A_{bf}}{A_o} + \frac{A_f}{A_o}\eta_f(\alpha_a^i)] \tag{3.77}$$

where $A_{bf}$ area of the outer tube surface between the fins, $A_f$ surface area of the fins, $\eta_f(\alpha_a)$ fin efficiency.

The boundary conditions in Eq. (3.78) have the following form:

$$T_a^i\big|_{y=0} = T_a^0 \tag{3.78}$$

Solving Eq. (3.74) considering the boundary condition Eq. (3.78)

$$T_a^i(y) = T_w + (T_a^i - T_w)e^{-N_a^i y}, \qquad 0 \leq y \leq 1 \tag{3.79}$$

Substituting $y = 1$ into Eq. (3.79) obtained the outlet temperature for the $i$-th row of tubes.

$$T_a^{i+1} = T_a^i(y) = T_w + (T_a^i - T_w)e^{-N_a^i} \tag{3.80}$$

The air temperature behind each row of tubes was determined sequentially. First, the air temperature behind the first row of tubes is determined (Eq. 3.81). The air temperature behind the first row of tubes is, in turn, the temperature at the inlet of the second row of tubes (Eq. 3.82). The resulting average air temperatures behind each row of tubes are determined by the following formulas (Eq. 3.81 - Eq. 3.84):

Considering the range of $(y)$ for the next $i$-th row of tubes, the obtained outlet temperatures for the $i$-th row of tubes.

- $T_{a,I}$ behind the first row of tubes:

$$Row\ 1 \qquad T_{a,I} = T_w + (T_a^0 - T_w)e^{-N_{a,I}} \tag{3.81}$$

- $T_{a,II}$ behind the second row of tubes:

$$Row\ 2 \qquad T_{a,II} = T_w + (T_{a,I} - T_w)e^{-(N_{a,I}+N_{a,II})} \tag{3.82}$$

- $T_{a,III}$ behind the third row of tubes:

$$Row\ 3 \qquad T_{a,III} = T_w + (T_{a,II} - T_w)e^{-(N_{a,I}+N_{a,II}+N_{a,III})} \tag{3.83}$$

- $T_{a,IV}$ behind the fourth row of tubes:

$$Row\ 4 \qquad T_{a,IV} = T_w + (T_{a,III} - T_w)e^{-(N_{a,I}+N_{a,II}+N_{a,III}+N_{a,IV})} \tag{3.84}$$

The symbols $N_{a,I}$, $N_{a,II}$, $N_{a,III}$ and $N_{a,IV}$ indicate the number of $NTU$ heat transfer units on the first, second, third and fourth rows of tubes.

The outlet temperature from the entire heat exchanger using the average air-side heat transfer coefficient.

$$T_a^{out} = T_w + (T_a^{in} - T_w)e^{-(4N_a^{avg})} \tag{3.85}$$

The symbol $T_a^0$ means air temperature in front of the heat exchanger, $T_{a,I}$ outlet air temperature of the particular row e.g. $T_{a,I}$ for row 1., $T_{a,II}$ for row 2., etc. The symbol $T_w$ denotes the temperature of the water and $N_a^i$ equals the number of heat exchange units for the $i$-th row of tubes e.g. $N_{a,I}$ for row 1., $N_{a,II}$ for row 2., etc. The symbol $N_a^{avg}$ means the average number of heat exchange units for the entire heat exchanger.

The resulting nonlinear equations from Eq. (3.81) to Eq. (3.85 with respect to air-side HTC ($\alpha_a$) can be solved by performing CFD simulations or having experiments. Necessarily is to obtain the air temperature behind each row of tubes. Next, for $n$ different air velocities in front of the PFTHE $w_j^0, j = 1, ..., n$, $n$ air temperatures behind each row of tubes $T_a^{cfd,i+1}$ are obtained, and the HTC coefficient of the air-side $\alpha_{a,j}^i, j = 1, ..., n$ are obtained.

## 3.7 Model Validation - Comparison with existing average Nusselt number correlations

The results of the Nusselt number of the CFD model under investigation are shown in Fig. 3.12, along with more recent correlations such as Wang et al. (1997) [115] and Wang et al. (1996) [116], Gray and Webb (1986) [3], McQuiston (1981) [117].

In the instance of a Nusselt number comparison, Fig. 3.12 compares the correlations found by the current CFD investigation (method 1, method 2, and method 3) with the most recent correlations mentioned above. Tab 3.3 lists the geometric parameters and study constraints that were compared. It should be observed that the geometry of the research given is rather similar but not necessarily identical.

For $Re_{d_o}$ = 1000, $Re_{d_o}$ = 2000, and $Re_{d_o}$ = 13,000, respectively, there is a relative difference of -10.3%, 12.0 % and 29.6 % between the average Nusselt numbers for the three methods provided in this study and the Nusselt number correlation for Wang et al.

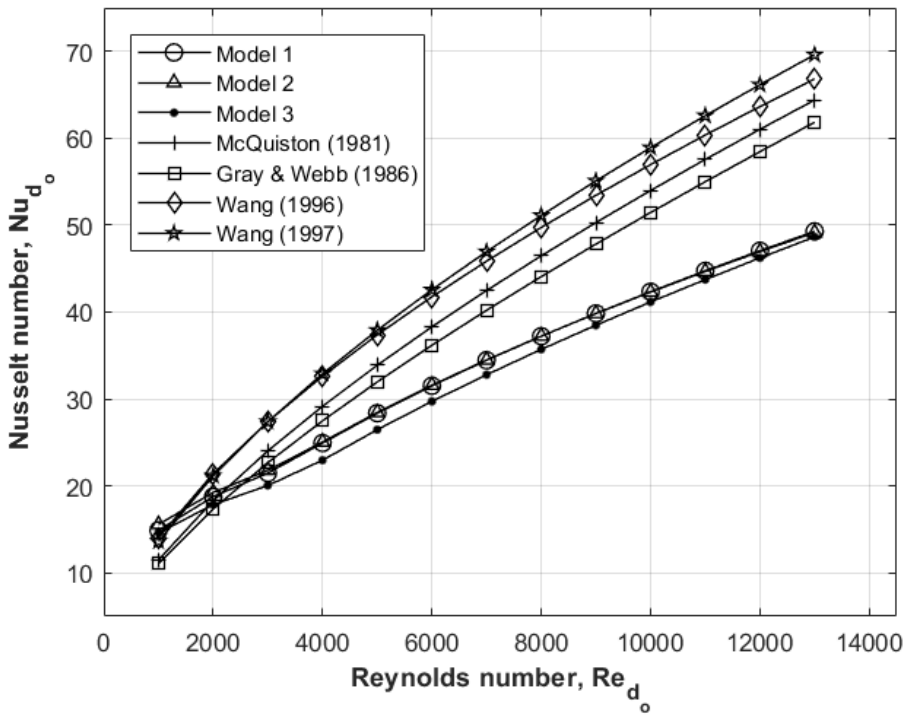


Figure 3.12: Average Nusselt number for the entire PFTHE in a function of Reynolds number based on the outer tube diameter for different research.

| Description | Designa -tion | Current Study - 3 methods | Wang et al. [115] | Wang et al. [116] | Gray & Webb [3] | McQuiston [117] |
|---|---|---|---|---|---|---|
| Rows | R | 4 | 2-6 | 2-6 | 4 | 4 |
| Transversal tube pitch [mm] | $p_t$ | 32 | 25.4 | 25.4 | - | 25.4 - 50.8 |
| Longitudinal tube pitch [mm] | $p_l$ | 27.71 | 22.0 | 22.0 | - | 25.4 - 50.8 |
| Tube outer diameter [mm] | $d_o$ | 12 | 10.23 | 10.23 | - | 9.53-15.86 |
| Fin pitch [mm] | $s$ | 3 | 1.75-3.21 | 1.82-3.20 | - | 1.81-6.35 |
| Fin thickness [mm] | $\delta_f$ | 0.14 | 0.13-0.2 | 0.13 | - | 0.15-0.25 |
| Ratio $p_t/d_o$ | - | 2.67 | - | - | 1.97-2.55 | - |
| Ratio $p_l/d_o$ | - | 2.31 | - | - | 1.7-2.58 | - |
| Ratio $s/d_o$ | - | 0.25 | - | - | 0.08-0.64 | - |

Table 3.3: Dimensions of PFTHE geometry from different researches.

(1997) [115]. When $Re_{d_o}$ = 1000, $Re_{d_o}$ = 2000, and $Re_{d_o}$ = 13,000 are used, there is a -6.9 %, 13.0 % and 26.6 % relative difference between the Nusselt number provided in this study and the Nusselt number correlation for Wang et al. (1996) [116]. When $Re_{d_o}$ = 1000, $Re_{d_o}$ = 3000 and $Re_{d_o}$ = 13,000 are used, there is a -36.0 %, 6.9 %and 20.7 % relative difference between the Nusselt number provided in this study and the Nusselt number correlation for McQuiston [117]. For $Re_{d_o}$ = 1000, $Re_{d_o}$ = 2000, and $Re_{d_o}$ =

13,000, respectively, there is a relative difference of -30.7%, -1.7 % and 23.9 % between the average Nusselt numbers for three methods provided in this study and the correlation of the Nusselt number for Gray and Webb [3].

The findings in Fig. 3.12 above demonstrate that the proposed models and calculations carried out in Ansys Fluent rather faithfully reflect the heat transport assumptions in the heat exchangers under discussion. The correlations provided in this work were obtained using CFD modeling, whereas the other correlations were determined using experimental tests, which may account for the modest variations. Given that the geometry of the exchangers under study differs in terms of both tube diameter and the distance between tubes and fins, the differences between the correlations achieved experimentally and the correlation predicted by Ansys Fluent calculations are acceptable. Moreover, varying experimental test settings and the parameters used in CFD modeling might result in variations in the values of the Nusselt number.

## 3.8 Air-side Nusselt number correlations for the individual row of tubes and for the entire heat exchanger

This subsection presents the temperature increment over the particular row of tubes and the total temperature rise of the entire heat exchanger. The obtained air-side Nusselt number correlations are also presented in the continuation of the paragraph. In addition, the general assumptions of the simulations are shown in section 3.2, and the particular dimensionless numbers and other supplementary equations are shown in section 3.3. The temperature results and correlations were prepared for three different CFD methods described in the earlier subsections: method 1 - assume constant temperature of the fin surface and constant temperature of the external surfaces of the tubes - subsection 3.6.1, method 2 - constant temperature of the fin base and constant temperature of the external surfaces of the tubes - subsection 3.6.2 and method 3 - constant temperature of the free flow and constant heat transfer coefficient on the inner side of the tube - subsection 3.6.3. The validation of CFD models and the comparison of the average Nusselt number correlations with correlations found in the literature are presented in subsection 3.7.

**Air temperature results**

The results of the calculation of the average mass air temperature based on the CFD simulation behind each row $T_{a,I}$, $T_{a,II}$, $T_{a,III}$, $T_{a,IV}$ are summarized in the Tab. 3.4 for method 1 and in the Tab. 3.5 for method 2.

The air temperature results were checked over a range of air velocities in front of the exchanger, from 0.5 to 10 m/s. Except that up to a velocity of 3 m/s, simulations were performed every 0.5 m/s due to the supposed limit of laminar and turbulent airflow inside the exchanger. On the other hand, from 3 m/s onward, checking was done every

1 m/s. Also, the difference in temperature rise between successive rows decreases as the temperature increases. This is because the air is heated significantly less the higher the airflow is at the same liquid flow inside the heat exchanger tubes than at low air speeds.

| $j$ | $w_o$, $m/s$ | $T_{a,I}$, $°C$ | $T_{a,II}$, $°C$ | $T_{a,III}$, $°C$ | $T_{a,IV}$, $°C$ |
|---|---|---|---|---|---|
| 1 | 0.5 | 52.69 | 63.06 | 66.99 | 68.65 |
| 2 | 1 | 42.87 | 53.56 | 59.30 | 63.12 |
| 3 | 1.5 | 38.43 | 48.52 | 54.78 | 59.52 |
| 4 | 2 | 35.84 | 45.40 | 51.57 | 56.62 |
| 5 | 2.5 | 34.11 | 43.22 | 49.09 | 54.25 |
| 6 | 3 | 32.86 | 41.59 | 47.22 | 52.49 |
| 7 | 4 | 31.14 | 39.26 | 44.61 | 50.03 |
| 8 | 5 | 29.98 | 37.65 | 42.84 | 48.18 |
| 9 | 6 | 29.15 | 36.40 | 41.43 | 46.79 |
| 10 | 7 | 28.50 | 35.53 | 40.45 | 45.59 |
| 11 | 8 | 27.99 | 34.89 | 39.72 | 44.73 |
| 12 | 9 | 27.57 | 34.25 | 39.05 | 43.87 |
| 13 | 10 | 27.21 | 33.75 | 38.50 | 43.35 |

Table 3.4: Air temperature behind each row determined by CFD for method 1.

| $j$ | $w_o$, $m/s$ | $T_{a,I}$, $°C$ | $T_{a,II}$, $°C$ | $T_{a,III}$, $°C$ | $T_{a,IV}$, $°C$ |
|---|---|---|---|---|---|
| 1 | 0.5 | 49.72 | 61.04 | 65.79 | 67.97 |
| 2 | 1 | 40.09 | 50.98 | 57.14 | 61.37 |
| 3 | 1.5 | 35.83 | 45.77 | 52.05 | 57.06 |
| 4 | 2 | 33.37 | 42.59 | 48.69 | 53.79 |
| 5 | 2.5 | 31.72 | 40.38 | 46.04 | 51.09 |
| 6 | 3 | 30.54 | 38.70 | 44.00 | 49.07 |
| 7 | 4 | 28.91 | 36.43 | 41.24 | 46.25 |
| 8 | 5 | 27.82 | 34.53 | 39.09 | 43.85 |
| 9 | 6 | 27.02 | 33.37 | 37.74 | 42.44 |
| 10 | 7 | 26.40 | 32.41 | 36.60 | 41.15 |
| 11 | 8 | 25.91 | 31.52 | 35.58 | 39.88 |
| 12 | 9 | 25.51 | 30.82 | 34.72 | 38.67 |
| 13 | 10 | 25.18 | 30.31 | 34.13 | 37.98 |

Table 3.5: Air temperature behind each row determined by CFD for method 2.

The results of the calculation of the increase in the air temperature of the average mass in each row for method 3 $\Delta T_{a,I}$, $\Delta T_{a,II}$, $\Delta T_{a,III}$, $\Delta T_{a,IV}$ and the temperature increase of the entire heat exchanger $\Delta T_{a,t}$ are summarized in the tab. 3.6 for method 3.

It can be seen in Tab. 3.6 that the increase in air temperature is greatest for the first row for low air velocities. However, for air velocities of 8 m/s and higher, the largest air temperature rise is observed for the second row.

| $j$ | $w_0$, $m/s$ | $\Delta T_{a,I}$, $°C$ | $\Delta T_{a,II}$, $°C$ | $\Delta T_{a,III}$, $°C$ | $\Delta T_{a,IV}$, $°C$ | $\Delta T_{a,t}$, $°C$ |
|---|---|---|---|---|---|---|
| 1 | 0.47 | 17.72 | 9.92 | 4.36 | 2.67 | 34.87 |
| 2 | 1.11 | 9.22 | 6.10 | 4.39 | 3.39 | 23.09 |
| 3 | 1.45 | 9.08 | 6.35 | 4.93 | 3.93 | 24.29 |
| 4 | 2.06 | 6.49 | 5.05 | 4.02 | 3.45 | 19.01 |
| 5 | 2.55 | 5.50 | 4.57 | 3.61 | 3.25 | 16.92 |
| 6 | 3.13 | 4.94 | 4.37 | 3.43 | 3.19 | 15.92 |
| 7 | 4.07 | 3.51 | 3.24 | 2.54 | 2.54 | 11.83 |
| 8 | 4.91 | 2.77 | 2.59 | 2.19 | 2.24 | 9.78 |
| 9 | 6 | 3.93 | 3.59 | 3.22 | 3.32 | 14.06 |
| 10 | 7 | 3.48 | 3.38 | 2.90 | 2.92 | 12.68 |
| 11 | 8 | 3.12 | 3.14 | 2.59 | 2.59 | 11.44 |
| 12 | 9 | 2.84 | 2.90 | 2.53 | 2.49 | 10.76 |
| 13 | 10 | 2.61 | 2.67 | 2.33 | 2.24 | 9.85 |

Table 3.6: Air temperature increments on each row and the total air temperature increment over the entire heat exchanger determined by CFD for method 3.

**Parameters $x_1$ and $x_2$ of the air heat transfer coefficient correlations**

For method 1, the results of the heat transfer coefficient $\alpha_a$ (Eq. 3.62) determined based on the total heat transferred by the surface of the fins and tubes $Q_a$, the total heat transfer area $A$ and the logarithmic mean temperature $\Delta\overline{T}_{m,a}$ are presented in Tab. 3.7.

| $j$ | $w_0$ $\frac{m}{s}$ | $\alpha_{a,avg}$ $\frac{W}{m^2K}$ | $\alpha_{a,I}$ $\frac{W}{m^2K}$ | $\alpha_{a,II}$ $\frac{W}{m^2K}$ | $\alpha_{a,III}$ $\frac{W}{m^2K}$ | $\alpha_{a,IV}$ $\frac{W}{m^2K}$ | $Nu_{a,avg}$ | $Nu_{a,I}$ | $Nu_{a,II}$ | $Nu_{a,III}$ | $Nu_{a,IV}$ |
|---|---|---|---|---|---|---|---|---|---|---|---|
| 1 | 0.5 | 31.45 | 36.57 | 32.41 | 29.59 | 28.49 | 6.06 | 7.20 | 6.03 | 5.40 | 5.16 |
| 2 | 1.0 | 34.78 | 42.43 | 35.52 | 30.46 | 31.37 | 6.75 | 8.46 | 6.77 | 5.68 | 5.78 |
| 3 | 1.5 | 41.21 | 47.98 | 40.96 | 36.60 | 39.86 | 8.03 | 9.63 | 7.91 | 6.91 | 7.42 |
| 4 | 2.0 | 46.42 | 53.09 | 46.51 | 40.93 | 45.62 | 9.08 | 10.69 | 9.05 | 7.80 | 8.56 |
| 5 | 2.5 | 50.86 | 57.82 | 51.86 | 43.86 | 50.33 | 9.99 | 11.67 | 10.14 | 8.41 | 9.51 |
| 6 | 3.0 | 55.48 | 62.27 | 56.94 | 47.00 | 56.13 | 10.92 | 12.59 | 11.18 | 9.05 | 10.65 |
| 7 | 4.0 | 64.74 | 70.47 | 66.48 | 54.14 | 68.24 | 12.78 | 14.28 | 13.12 | 10.49 | 13.04 |
| 8 | 5.0 | 73.17 | 77.93 | 75.36 | 61.93 | 77.82 | 14.49 | 15.82 | 14.93 | 12.06 | 14.94 |
| 9 | 6.0 | 81.33 | 84.89 | 83.12 | 68.86 | 88.79 | 16.13 | 17.26 | 16.52 | 13.46 | 17.11 |
| 10 | 7.0 | 88.65 | 91.44 | 92.00 | 76.42 | 95.09 | 17.61 | 18.60 | 18.32 | 14.97 | 18.38 |
| 11 | 8.0 | 96.43 | 97.64 | 101.69 | 83.90 | 102.84 | 19.18 | 19.88 | 20.28 | 16.47 | 19.92 |
| 12 | 9.0 | 103.19 | 103.59 | 109.19 | 91.70 | 108.63 | 20.55 | 21.10 | 21.81 | 18.03 | 21.08 |
| 13 | 10.0 | 111.24 | 109.32 | 117.44 | 99.47 | 119.11 | 22.17 | 22.28 | 23.48 | 19.59 | 23.15 |

Table 3.7: Heat transfer coefficient $\alpha_a$ and Nusselt number $Nu_a$ for different air velocities for method 1.

The equation for this method used to determine the average heat transfer coefficient $\alpha_a$ of the entire PFTHE and for the $i$-th row of tubes has the following formula:

$$\alpha_a^i = \frac{Q_a}{A\Delta\overline{T}_{m,a}^i} \tag{3.86}$$

The Nusselt number of each tube row was approximated as a power function of the Reynolds and Prandtl numbers using Eq. (3.87). This equation was derived from the Colburn analogy, which states that $Nu/(RePr^{1/3}) = f(Re)$. The function $f(Re)$ is determined by CFD simulations. Once the coefficients $x_1$ and $x_2$ are obtained by CFD modeling of airflow, Eq. (3.87) can also be used to calculate the Nusselt number for other gases.

$$Nu_a = x_1 Re_a^{x_2} Pr_a^{1/3} \tag{3.87}$$

$Nu_a = f(Re_a, Pr_a)$. The non-dimensional numbers: Nusselt $Nu_a$, Reynolds $Re_a$, and Prandtl $Pr_a$, and, in addition, other formulas necessary to calculate the components of these numbers are presented in subsection 3.3. The least squares method was used to determine the unknown parameters $x_1$ and $x_2$ in the approximation function. The 95 % confidence intervals for the Nusselt number in each tube row, were calculated using the least squares method. The values obtained from Eq. 3.87 differ by +/- 2 $\sigma$, where $\sigma$ is the mean standard deviation of the Nusselt numbers obtained by the CFD modeling.

The parameters $x_1$ and $x_2$ of method 1 for the correlations determined for the average Nusselt numbers for the entire exchanger and for correlations of Nusselt numbers of individual rows of tubes are shown in Tab 3.8.

| Reynolds number range | 200 $<Re_a<$1400 | | 1400 $<Re_a<$6000 | |
|---|---|---|---|---|
| Correlation's parameter | $x_1$ | $x_2$ | $x_1$ | $x_2$ |
| Average | 0.9760 | 0.3337 | 0.1652 | 0.5781 |
| Row 1 | 1.4001 | 0.3053 | 0.4217 | 0.4700 |
| Row 2 | 0.9478 | 0.3386 | 0.1305 | 0.6118 |
| Row 3 | 1.0403 | 0.3025 | 0.0923 | 0.6307 |
| Row 4 | 0.5230 | 0.4156 | 0.1282 | 0.6145 |

Table 3.8: The PFTHE air-side Nusselt number correlation parameters of method 1 for different Reynolds number ranges.

For method 2 and 3 the results of the heat transfer coefficient $\alpha_a$ determined based on the increase in air temperatures calculated on the basis of CFD simulations are shown in the Tab. 3.9 for method 2 and Tab. 3.10 for method 3. The nonlinear equation for this method used to determine average heat transfer coefficient $\alpha_a$ of the entire PFTHE has

the following formula:

$$Average \qquad (T_w - T_a^0)\left[1 - e^{-(4N_a^{avg})}\right] - \Delta T_{a,t}^{cfd} = 0 \tag{3.88}$$

However, for the individual row of tubes: $\alpha_a$ of the entire PFTHE has the following formula:

$$Row\ 1 \qquad (T_w - T_a^0)\left[1 - e^{-(N_{a,I})}\right] - \Delta T_{a,I}^{cfd} = 0 \tag{3.89}$$

$$Row\ 2 \qquad (T_w - T_{a,I})\left[1 - e^{-(N_{a,II})}\right] - \Delta T_{a,II}^{cfd} = 0 \tag{3.90}$$

$$Row\ 3 \qquad (T_w - T_{a,II})\left[1 - e^{-(N_{a,III})}\right] - \Delta T_{a,III}^{cfd} = 0 \tag{3.91}$$

$$Row\ 4 \qquad (T_w - T_{a,III})\left[1 - e^{-(N_{a,IV})}\right] - \Delta T_{a,IV}^{cfd} = 0 \tag{3.92}$$

| $j$ | $w_0$ $\frac{m}{s}$ | $\alpha_{a,avg}$ $\frac{W}{m^2K}$ | $\alpha_{a,I}$ $\frac{W}{m^2K}$ | $\alpha_{a,II}$ $\frac{W}{m^2K}$ | $\alpha_{a,III}$ $\frac{W}{m^2K}$ | $\alpha_{a,IV}$ $\frac{W}{m^2K}$ | $Nu_{a,avg}$ | $Nu_{a,I}$ | $Nu_{a,II}$ | $Nu_{a,III}$ | $Nu_{a,IV}$ |
|---|---|---|---|---|---|---|---|---|---|---|---|
| 1 | 0.5 | 32.82 | 36.45 | 32.79 | 30.23 | 29.16 | 6.33 | 7.20 | 6.13 | 5.54 | 5.30 |
| 2 | 1.0 | 36.70 | 41.95 | 35.86 | 30.80 | 31.37 | 7.14 | 8.40 | 6.89 | 5.78 | 5.81 |
| 3 | 1.5 | 42.13 | 47.39 | 41.21 | 35.75 | 39.20 | 8.24 | 9.54 | 8.01 | 6.80 | 7.35 |
| 4 | 2.0 | 47.18 | 52.47 | 46.89 | 40.73 | 44.47 | 9.27 | 10.60 | 9.19 | 7.82 | 8.41 |
| 5 | 2.5 | 51.28 | 57.21 | 52.47 | 43.30 | 48.61 | 10.11 | 11.59 | 10.33 | 8.36 | 9.26 |
| 6 | 3.0 | 55.72 | 61.67 | 57.67 | 45.99 | 54.19 | 11.02 | 12.51 | 11.40 | 8.93 | 10.38 |
| 7 | 4.0 | 65.15 | 69.95 | 68.94 | 52.36 | 65.99 | 12.93 | 14.22 | 13.70 | 10.23 | 12.73 |
| 8 | 5.0 | 72.42 | 77.43 | 75.35 | 59.64 | 74.16 | 14.42 | 15.77 | 15.04 | 11.72 | 14.39 |
| 9 | 6.0 | 81.86 | 84.32 | 85.55 | 67.89 | 85.97 | 16.34 | 17.19 | 17.12 | 13.39 | 16.75 |
| 10 | 7.0 | 90.13 | 90.78 | 94.56 | 75.14 | 96.14 | 18.02 | 18.52 | 18.96 | 14.86 | 18.79 |
| 11 | 8.0 | 96.58 | 96.83 | 100.79 | 82.93 | 101.85 | 19.34 | 19.77 | 20.25 | 16.44 | 19.97 |
| 12 | 9.0 | 101.63 | 102.85 | 107.72 | 88.99 | 103.41 | 20.39 | 21.01 | 21.68 | 17.68 | 20.33 |
| 13 | 10.0 | 109.76 | 108.84 | 116.62 | 97.42 | 112.21 | 22.04 | 22.25 | 23.50 | 19.39 | 22.10 |

Table 3.9: Heat transfer coefficient $\alpha_a$ and Nusselt number $Nu_a$ for different air velocities for method 2.

The above formulas were resolved using a method to search the collection against $\alpha_a$. The Nusselt number of each tube row was approximated as a power function of the Reynolds and Prandtl numbers using Eq. (3.87). This equation was derived from the Colburn analogy, which states that $Nu/(RePr^{1/3}) = f(Re)$, as it was described for method 1.

The non-dimensional numbers: Nusselt $Nu_a$, Reynolds $Re_a$, and Prandtl $Pr_a$, and, other formulas necessary to calculate the components of these numbers are presented in subsection 3.3.

| $j$ | $w_0$ $\frac{m}{s}$ | $\alpha_{a,avg}$ $\frac{W}{m^2K}$ | $\alpha_{a,I}$ $\frac{W}{m^2K}$ | $\alpha_{a,II}$ $\frac{W}{m^2K}$ | $\alpha_{a,III}$ $\frac{W}{m^2K}$ | $\alpha_{a,IV}$ $\frac{W}{m^2K}$ | $Nu_{a,avg}$ | $Nu_{a,I}$ | $Nu_{a,II}$ | $Nu_{a,III}$ | $Nu_{a,IV}$ |
|---|---|---|---|---|---|---|---|---|---|---|---|
| 1 | 0.47 | 30.15 | 31.00 | 34.00 | 25.00 | 27.00 | 5.85 | 6.17 | 6.55 | 4.73 | 5.04 |
| 2 | 1.11 | 34.25 | 42.40 | 34.40 | 30.90 | 30.40 | 6.76 | 8.53 | 6.78 | 6.01 | 5.85 |
| 3 | 1.45 | 39.40 | 46.45 | 38.50 | 36.80 | 36.50 | 7.77 | 9.35 | 7.59 | 7.14 | 7.00 |
| 4 | 2.06 | 42.90 | 48.70 | 43.40 | 39.50 | 40.50 | 8.52 | 9.85 | 8.64 | 7.76 | 7.88 |
| 5 | 2.55 | 47.10 | 52.00 | 49.30 | 42.40 | 45.20 | 9.37 | 10.51 | 9.82 | 8.36 | 8.83 |
| 6 | 3.13 | 52.40 | 56.80 | 57.50 | 46.20 | 50.00 | 10.47 | 11.53 | 11.52 | 9.16 | 9.82 |
| 7 | 4.07 | 57.50 | 60.80 | 64.00 | 48.50 | 58.00 | 11.56 | 12.36 | 12.89 | 9.69 | 11.51 |
| 8 | 4.91 | 64.90 | 64.70 | 67.80 | 57.00 | 71.50 | 12.97 | 13.12 | 13.58 | 11.30 | 14.04 |
| 9 | 6.00 | 82.40 | 81.00 | 79.50 | 74.50 | 96.00 | 16.64 | 16.59 | 16.11 | 14.95 | 19.10 |
| 10 | 7.00 | 88.80 | 86.00 | 95.50 | 79.50 | 95.00 | 17.96 | 17.62 | 19.38 | 15.99 | 18.96 |
| 11 | 8.00 | 91.80 | 90.00 | 107.00 | 80.00 | 92.00 | 18.60 | 18.45 | 21.74 | 16.13 | 18.41 |
| 12 | 9.00 | 103.00 | 95.00 | 115.00 | 96.00 | 107.00 | 20.89 | 19.48 | 23.40 | 19.38 | 21.45 |
| 13 | 10.00 | 104.30 | 99.00 | 120.00 | 98.00 | 102.00 | 21.18 | 20.31 | 24.44 | 19.82 | 20.49 |

Table 3.10: Heat transfer coefficient $\alpha_a$ and Nusselt number $Nu_a$ for different air velocities for method 3.

| Reynolds number range | 200 $<Re_a<$1400 | | 1400 $<Re_a<$6000 | |
|---|---|---|---|---|
| Correlation's parameter | $x_1$ | $x_2$ | $x_1$ | $x_2$ |
| Average | 1.2063 | 0.3063 | 0.1737 | 0.572 |
| Row 1 | 1.4265 | 0.3013 | 0.3883 | 0.4791 |
| Row 2 | 0.9595 | 0.3388 | 0.1583 | 0.5894 |
| Row 3 | 1.1931 | 0.2821 | 0.0696 | 0.6622 |
| Row 4 | 0.657 | 0.3798 | 0.145 | 0.5963 |

Table 3.11: The PFTHE air-side Nusselt number correlation parameters of method 2 for different Reynolds number ranges.

| Reynolds number range | 200 $<Re_a<$1400 | | 1400 $<Re_a<$6000 | |
|---|---|---|---|---|
| Correlation's parameter | $x_1$ | $x_2$ | $x_1$ | $x_2$ |
| Average | 1.2617 | 0.2885 | 0.0978 | 0.6371 |
| Row 1 | 1.3884 | 0.2957 | 0.2485 | 0.5226 |
| Row 2 | 1.6234 | 0.2551 | 0.0537 | 0.7206 |
| Row 3 | 0.8066 | 0.3382 | 0.0477 | 0.7107 |
| Row 4 | 0.7602 | 0.35 | 0.1422 | 0.596 |

Table 3.12: The PFTHE air-side Nusselt number correlation parameters of method 3 for different Reynolds number ranges.

The least squares method was used also here to determine the unknown parameters $x_1$ and $x_2$ in the approximation function. The 95 % confidence intervals for the Nusselt number in each tube row, calculated using the least squares method, are also shown in each figure. The values obtained from Eq. 3.87 differ by +/- 2 $\sigma$, where $\sigma$ is the mean standard deviation of the Nusselt numbers obtained from the CFD modeling.

The parameters $x_1$ and $x_2$ of methods 2 and 3 for the correlations determined for the average Nusselt numbers for the entire exchanger and for the correlations of the Nusselt numbers of the individual rows of tubes are shown in Tab. 3.11 and Tab 3.12.

**Air heat transfer coefficient diagrams**

All three proposed methods for conducting CFD simulations showed similar results. The dependence of the air-side Nusselt number on the Reynolds number calculated from the hydraulic diameter for methods 1 (Fig. 3.13 and Fig. 3.14), 2 (Fig. 3.15 and Fig. 3.16), and 3 (Fig. 3.17 and Fig. 3.18) are presented respectively.

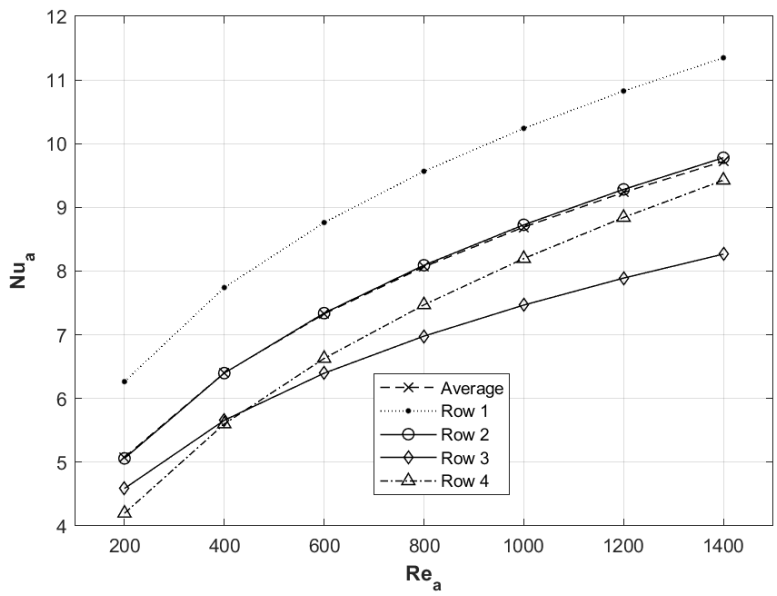


Figure 3.13: The impact of the PFTHE row number on the Nusselt number for method 1 in the following Reynolds number range 200–1400.

The high local values of the Nusselt number in the developing (run-up) section in channels produced by adjacent continuous fins are what cause the first tube row to have a high average Nusselt number for low air velocities (Fig. 3.13, Fig. 3.15 and Fig. 3.17). The rear stagnation point (region of the tube's surface toward the back) is where the dead zone has less of an impact than the second and third rows. Because of the development of air vortices close to the front and rear surfaces of the tube, the average Nusselt number on the second and third rows of tubes has lower values. As far as heat transfer is concerned, these are dead zones, since the swirling air temperature is nearly the same as the surfaces of the fins and tubes (Fig. 3.19).

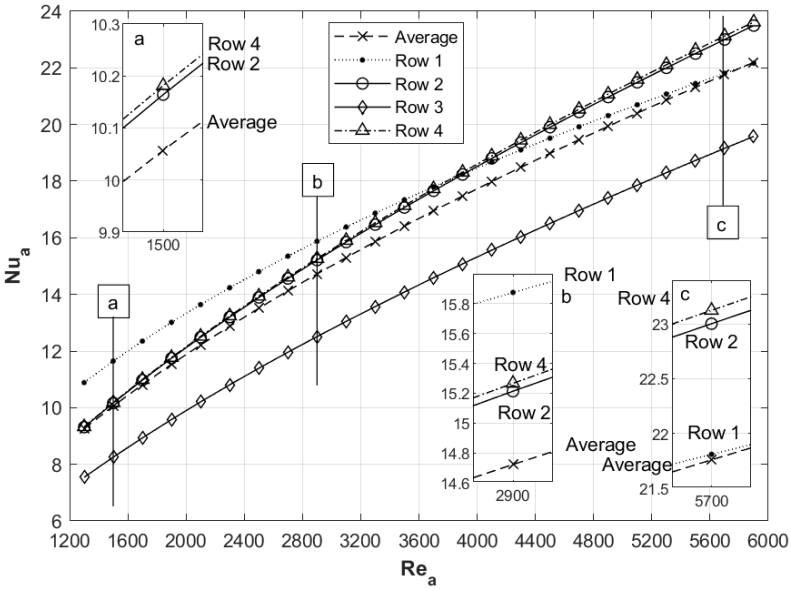


Figure 3.14: The impact of the PFTHE row number on the Nusselt number for method 1 in the following Reynolds number range 1400–6000.

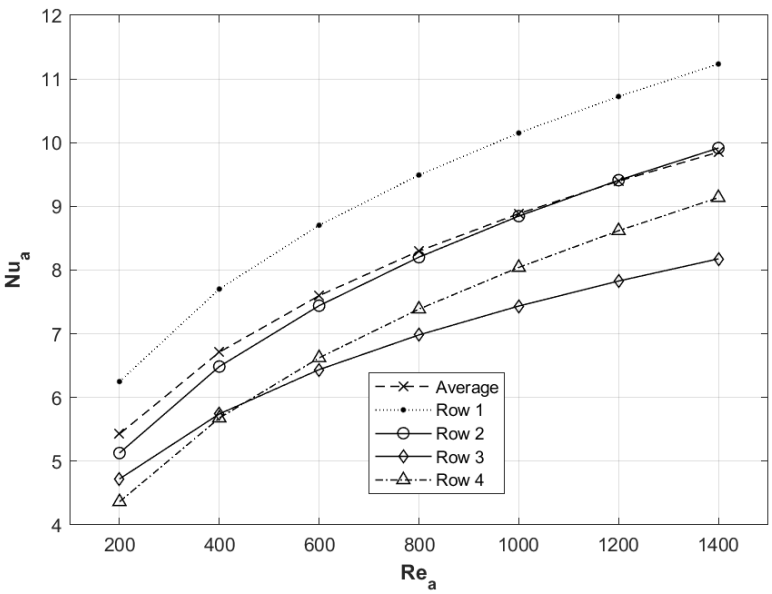


Figure 3.15: The impact of the PFTHE row number on the Nusselt number for method 2 in the following Reynolds number range 200–1400.

In cases where $Re_a \geq 400$, the average Nusselt number for the fourth row of tubes is higher than the average Nusselt number in the third row of tubes. This is because the air vortices that form behind and in front of the tubes in the fourth row have a smaller surface area than those in the third row (Fig. 3.19).

The distribution of the average Nusselt number in each row of tubes differs from that for smaller Reynolds numbers when the Reynolds numbers are greater than 1200 (Fig. 3.14, Fig. 3.16 and Fig. 3.18). For higher Reynolds number values, airflow through the

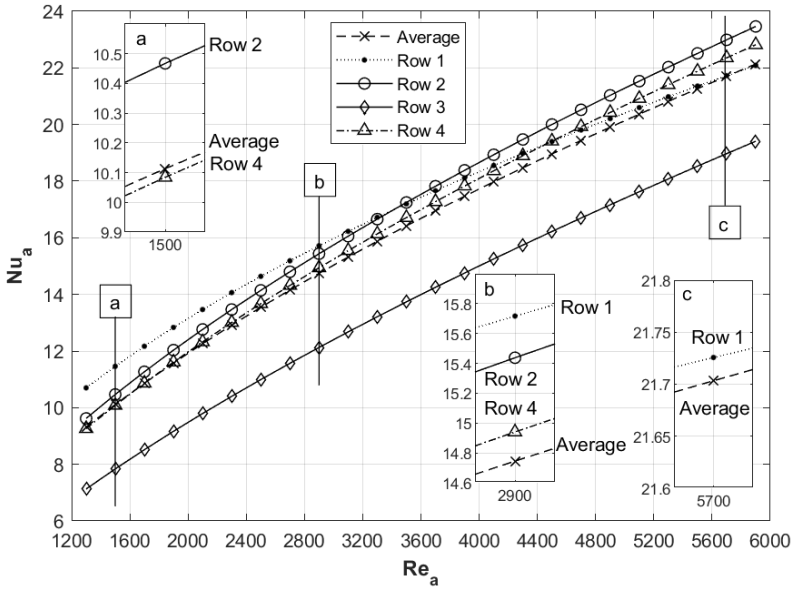


Figure 3.16: The impact of the PFTHE row number on the Nusselt number for method 2 in the following Reynolds number range 1400–6000.

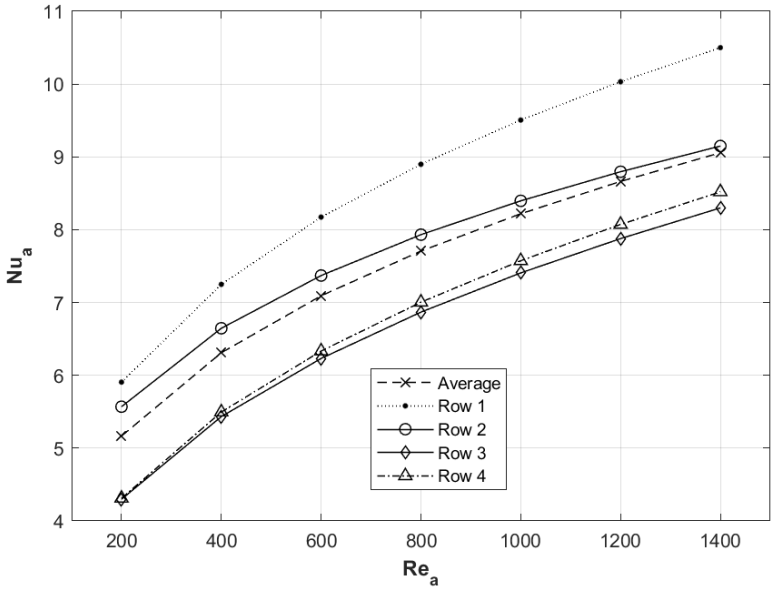


Figure 3.17: The impact of the PFTHE row number on the Nusselt number for method 3 in the following Reynolds number range 200–1400.

channels formed by the fins is mainly turbulent.

The length of the developing flow part in turbulent flows, where the airflow is thermally and hydraulically evolved, is considerably smaller compared to the laminar airflow. The input of the entry section to increase the average Nusselt number for the first and second rows of tubes is smaller than for laminar flow. The dead zones in the area of the rear surface of the first and second rows of tubes are similar. Therefore, the average Nusselt numbers for the first and second rows of tubes are similar.

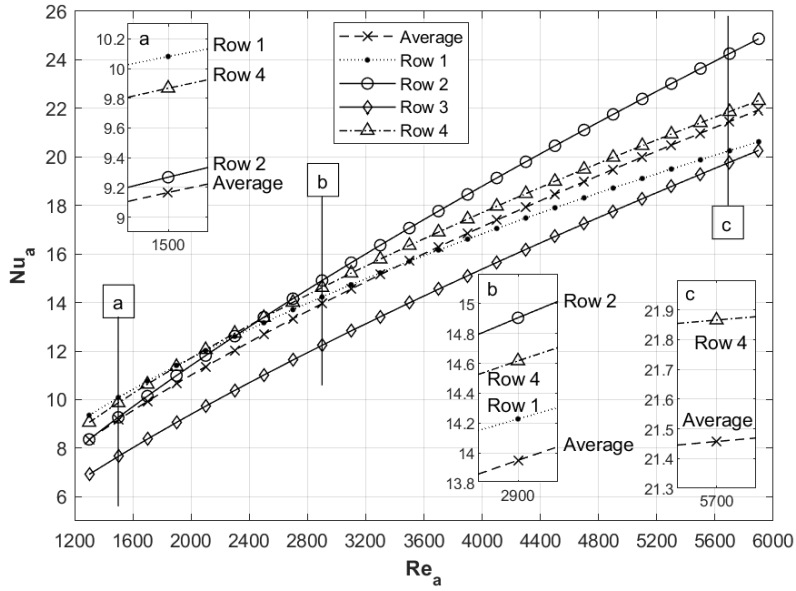


Figure 3.18: The impact of the PFTHE row number on the Nusselt number for method 3 in the following Reynolds number range 1400–6000.

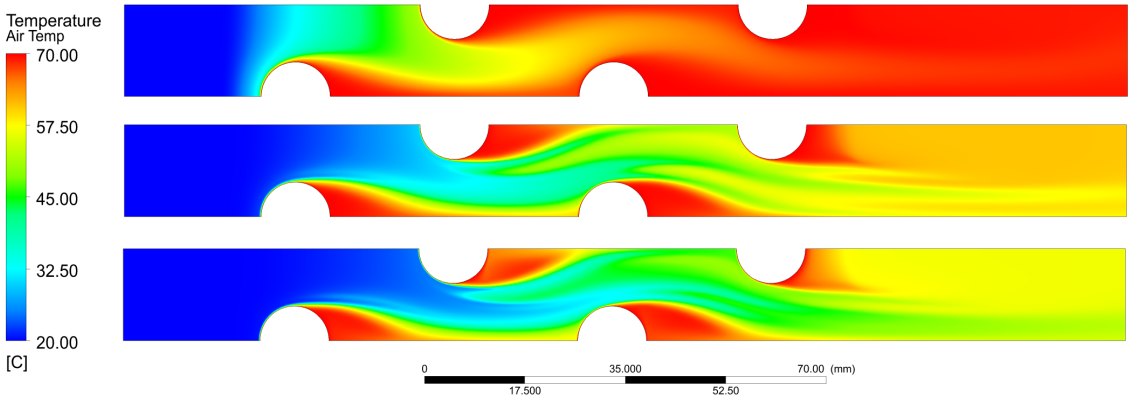


Figure 3.19: Air temperature in the middle of the distance between the fins for different airspeeds sequentially for method 1 from the top for: 0.5 $m/s$ ($Re_a \sim 200$), 1.5 $m/s$ ($Re_a \sim 800$) and 2.5 $m/s$ ($Re_a \sim 1400$).

The average Nusselt number on the first row of tubes is only higher than that on the second row of tubes in the Reynolds number range from 200 to 2000 - 3200. This is because the average Nusselt number on the inlet (developing) flow section for the first row of tubes is larger than that of the one on the inlet section in front of the second row of tubes for smaller Reynolds numbers.

According to a heat transfer perspective, the front and rear stagnation point areas of the third tube row have substantial dead zones, which lowers the average Nusselt number for this row. The smaller dead zone area adjacent to the rear stagnation point area behind the fourth tube row causes the fourth tube row's higher average Nusselt number value than the third row. In the third tube row, the stagnation points and the active narrow airflow

channel cause the least average Nusselt number for this row.

# 4 Numerical model of plate fin and tube heat exchangers

## 4.1 Differential equations for gas (air) and liquid (water) flowing inside the tube

The mathematical formulation of the energy conservation equations is used to properly determine the air and water temperatures in the next node. Plate fin and tube heat exchanger (PFTHE) with its specific non-continuous construction cause difficulties in definitions of the initial-boundary conditions. Each row of tubes in which mostly water (liquid) flows separates perpendicular air flow (gas) and causes complicated phenomena within the PFTHE (Fig. 4.1). There is no possibility to directly use the basic energy, mass, and momentum conversion formulas. These formulas must be written in the appropriate form to the heat exchanger (HEX) geometry and the type of the HEX model. In this case, formulas are adapted to the cross-flow PFTHE and consider its discrete design. Hence, it is necessary to divide the energy conservation equation into two of them, one for the air-side and one for the water-side [118].

The basic element of the exchanger model is the single-tube model. The governing differential equations describing the distribution of water and air temperatures for the one-tube row are as follows.

- for water (liquid) side:

$$\frac{dT_w(x)}{dx} = N_w[T_w(x) - \overline{T}_a(x)] \tag{4.1}$$

- for air (gas) side:

$$\frac{dT_a(x,y)}{dx} = N_a[T_w(x) - T_a(x,y)] \tag{4.2}$$

where the average air temperature $\overline{T}_a(x)$ over the entire tube row width $p_l$ at a given $x$ coordinate is defined as follows

$$\overline{T}_a(x) = \int_0^{p_l} T_a(x,y)dy \tag{4.3}$$

The boundary conditions for both fluids for Eqs. 4.1 and 4.2 are given by

$$T_w|_{x=0} = T_w^i \tag{4.4}$$

$$T_a|_{y=0} = T_a^i \tag{4.5}$$

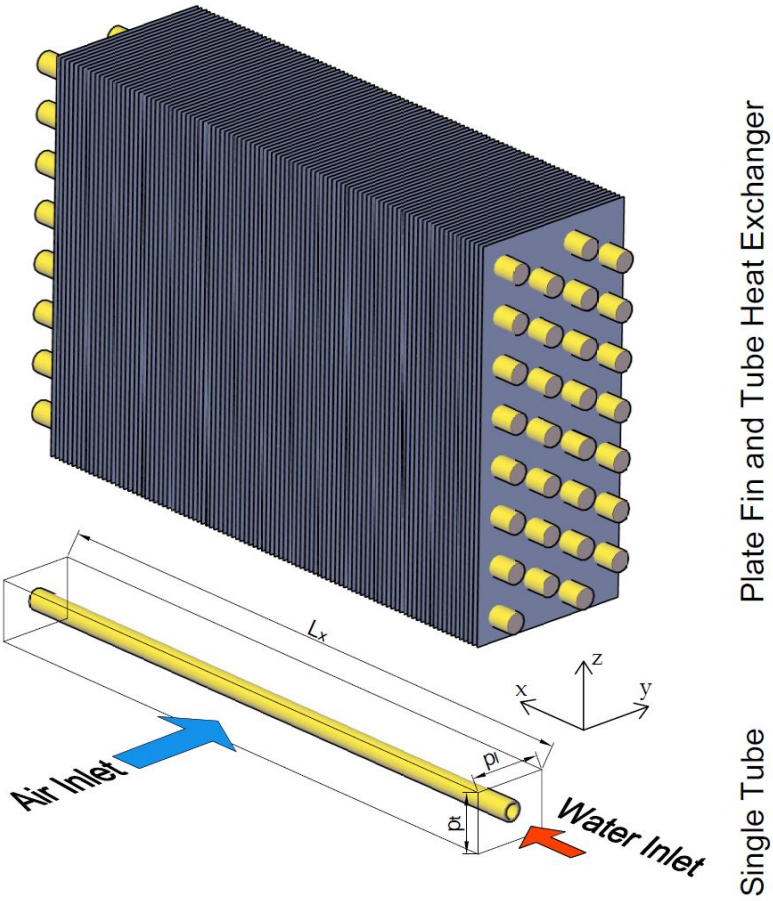


Figure 4.1: Diagram of the entire heat exchanger with a separate single tube inside which water and airflow in the direction perpendicular to the axis of the tube

The symbols $N_w$ in Eq. 4.1 and $N_a$ in Eq. 4.2 designate the number of heat transfer units (NTU) for water and air, respectively, and are defined as follows

$$N_w = \frac{U_o A_o}{\dot{m}_w c_w} \tag{4.6}$$

$$N_a = \frac{U_o A_o}{\dot{m}_a c_{p,a}} \tag{4.7}$$

The symbols in Eqs. 4.6 and 4.7 denote: $U_o$ the overall heat transfer coefficient based on the outer surface $A_o$ of the bare tube, $A_o = \pi d_o L_x$, $d_o$ the outer diameter of the bare tube, $L$ the length of the tube, $\dot{m}_w$, $\dot{m}_a$ the flow rate of water and air, $c_w$, $c_{p,a}$ the specific heat of water and air. The overall heat transfer coefficient $U_o$ related to the outer surface area of the bare tube is calculated as follows

$$\frac{1}{U_o} = \frac{1}{\alpha_{eq}} + \frac{A_o}{A_{in}} \frac{\delta_t}{\lambda_t} + \frac{A_o}{A_{in}} \frac{1}{\alpha_w} \tag{4.8}$$

where $\alpha_{eq}$ the equivalent air-side heat transfer coefficient (HTC) considering the fins attached to the tube, $A_{in}$ the area of the inner surface of the tube, $\delta_t$ the thickness of the

wall of the tube, $\lambda_t$ the thermal conductivity of the tube material, $\alpha_w$ the water-side heat transfer coefficient. The equivalent air-side HTC in Eq. 4.8 $\alpha_{eq}$ is calculated using the mean value of the HTC in the entire row of the tube.

$$\alpha_{eq} = \alpha_a[\frac{A_{bf}}{A_o} + \frac{A_f}{A_o}\eta_f(\alpha_a)] \tag{4.9}$$

where $A_{bf}$ area of the outer tube surface between fins, $A_f$ surface area of the fins, $\eta_f(\alpha_a)$ fin efficiency. It should be emphasized that there are no simple formulae in heat exchanger literature for calculating the efficiency of both smooth and corrugated continuous fins. Marcinkowski et al. [119][120] presented a method for determining the efficiency of fins with complex shapes using finite element method (FEM). The efficiency of the fin was determined from the following formula

$$\eta_f = \frac{\overline{T}_f - T_a}{T_b - T_a} \tag{4.10}$$

where $\overline{T}_f$ mean temperature of the fin surface, $T_a$ ambient temperature, $T_b$ temperature of the fin base.

Numerical simulations used in calculating fin efficiency also allow verification of the maximum temperature of the metal from which the fin is constructed. By too high a temperature of the flowing gas, e.g., exhaust gas at 600 $°C$, the fin can be damaged by burn-through [119].

## 4.2 Mathematical modeling of cross-flow plate fin and tube heat exchangers

In this section, the numerical determination of air, liquid, and wall temperatures is presented.

### 4.2.1 Determination of the Air Temperature Distribution

The determination of water and air temperatures is based on the finite-volume method. At first, PFTHE is divided into N finite volumes (Fig. 4.2). The length of the finite volume (FV) is $\Delta x = L_x/N$. The thickness in the $y$ coordinate direction is equal $\Delta y = p_l$, where $p_l$ is the longitudinal pitch of the tube arrangement. The height of the FV in the $z$ coordinate direction is presented as $\Delta z = p_t$, where $p_t$ denotes the transversal pitch of the tube arrangement.

According to the FVM, the heat balance equations for air and liquid flowing inside the tube for a single FV are written first. The heat balance equation for air is:

$$\Delta\dot{m}_a i_a|_y + U_o\Delta x\Delta y(\overline{T}_{w,i} - T_a|_y) = \Delta\dot{m}_a i_a|_{y+\Delta y} \tag{4.11}$$

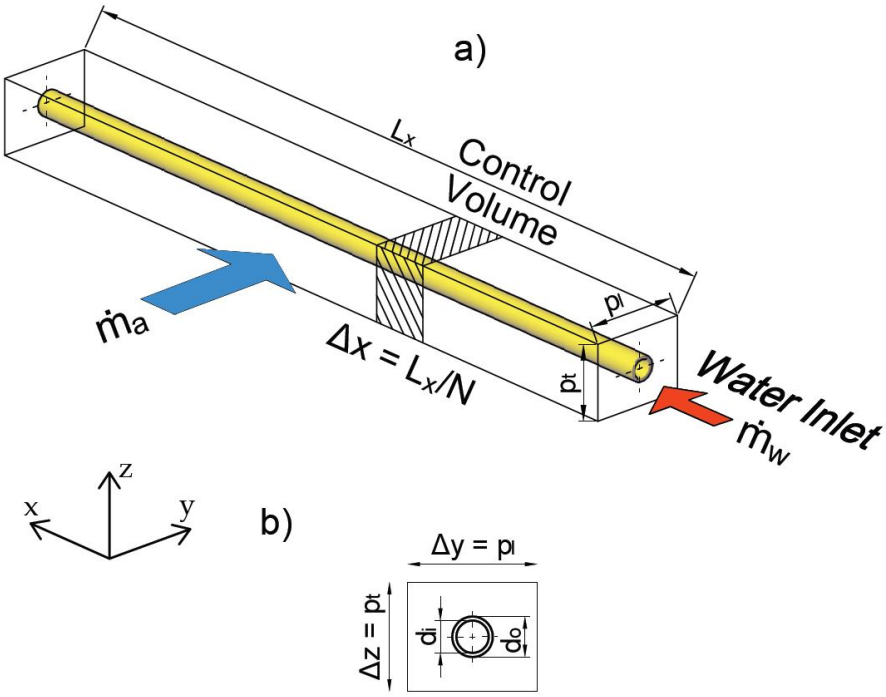


Figure 4.2: Schematic of the control area for the heat exchanger, water flows in the x-axis direction and air flows in the y-axis direction: a) control area, b) cross-sectional area

where the average temperature of the water can be calculated:

$$\overline{T}_{w,i} = \frac{T_{w,i} + T_{w,i+1}}{2} \tag{4.12}$$

The enthalpy of the air at the temperature $T_a$ (°C) is given by:

$$i_a = c_{p,a}\big|_0^{T_a} T_a \tag{4.13}$$

Considering Equation 4.13 in Equation 4.11:

$$\Delta\dot{m}_a \, c_{p,a}\big|_0^{T_a|_y} T_a\Big|_y + U_o \Delta x \Delta y (\overline{T}_{w,i} - T_a|_y) = \Delta\dot{m}_a \, c_{p,a}\big|_0^{T_a|_{y+\Delta y}} T_a\Big|_{y+\Delta y} \tag{4.14}$$

Writing down the average specific heat capacity of air in the constant pressure:

$$\overline{c}_{p,a,i} = \frac{c_{p,a,i}\big|_0^{T_a|_y} T_a|_y - c_{p,a,i}\big|_0^{T_a|_{y+\Delta y}} T_a|_{y+\Delta y}}{T_a|_y - T_a|_{y+\Delta y}} \tag{4.15}$$

Transforming equation Eq. 4.14 using equation Eq. 4.15, the result is:

$$\Delta\dot{m}_a \overline{c}_{p,a,i} (T_a|_y - T_a|_{y+\Delta y}) + U_o \Delta x \Delta y (\overline{T}_{w,i} - T_a|_y) = 0 \tag{4.16}$$

Solving Equation 4.16:

$$\Delta\dot{m}_a \overline{c}_{p,a,i} \frac{T_a|_{y+\Delta y} - T_a|_y}{\Delta y} + U_o \Delta x (T_a|_y - \overline{T}_{w,i}) = 0 \tag{4.17}$$

Then considering that $\Delta x \to 0$ and writing in the differential form:

$$\Delta \dot{m}_a c_{p,a}(T_a)\frac{\partial T_g}{\partial y} + U_o \Delta x(T_a - \overline{T}_{w,i}) = 0 \tag{4.18}$$

Additionally, the boundary condition in Eq. (4.19) can be considered in Equation 4.18

$$T_a|_{y=0} = T_{a,i}^{'} \tag{4.19}$$

and considering also the mean value of the specific capacity $\overline{c}_{p,a,i} = [c_{p,a}(T_{a,i}^{'}) + c_{p,a}(T_{a,i}^{''})]/2$, Eq. (4.18) takes the form

$$\frac{\partial(\overline{T}_{w,i} - T_{a,i})}{\partial y} = -\frac{U_o \Delta x}{\Delta \dot{m}_a \overline{c}_{p,a,i}}(\overline{T}_{w,i} - T_{a,i}) \tag{4.20}$$

By integrating, Eq. (4.20) transforms into the form

$$\int \frac{d(\overline{T}_{w,i} - T_{a,i})}{\overline{T}_{w,i} - T_{a,i}} = -\frac{U_o \Delta x}{\Delta \dot{m}_a \overline{c}_{p,a,i}} \int \Delta y + C \tag{4.21}$$

$$ln(\overline{T}_{w,i} - T_{a,i}) = -\frac{U_o \Delta x}{\Delta \dot{m}_a \overline{c}_{p,a,i}} y + C \tag{4.22}$$

Eq. (4.22) can be rewritten to

$$T_{a,i} = \overline{T}_{w,i} - C_1 exp(-\frac{U_o \Delta x}{\Delta \dot{m}_a \overline{c}_{p,a,i}} y) \tag{4.23}$$

where constant $C_1 = e^C$.
Considering the boundary condition Eq. (4.19) in Eq. (4.25) gives

$$C_1 = (\overline{T}_{w,i} - T_{a,i}) \tag{4.24}$$

Substituting $C_1$ and placing $y = p_l$ in Eq. (4.25), gives the air temperature $T_{a,i}^{''}$ behind the tube

$$T_{a,i}^{''} = \overline{T}_{w,i} - (\overline{T}_{w,i} - T_{a,i}^{'})\, exp\,(-\frac{U_o \Delta x p_l}{\Delta \dot{m}_a \overline{c}_{p,a,i}}), \qquad i = 1, ...., N \tag{4.25}$$

The area of the heat transfer $\Delta A$ in one control volume equals

$$\Delta A = p_l\, \Delta x = \pi d_o p_l \tag{4.26}$$

Considering Eq. (4.26) in Eq. (4.25), Eq. (4.25) becomes

$$T_{a,i}^{''} = \overline{T}_{w,i} - (\overline{T}_{w,i} - T_{a,i}^{'})\, exp\,(-\Delta N_{a,i}) \tag{4.27}$$

where

$$\Delta N_{a,i} = \frac{U_o \Delta A_o}{\Delta \dot{m}_a c_{p,a,i}}, \qquad A_o = P_o L_x, \qquad \Delta A_o = \frac{A_o}{N}, \qquad \overline{T}_{w,i} = \frac{T_{w,i} + T_{w,i+1}}{2} \tag{4.28}$$

In Eq. (4.28), the symbols denote $A_o$ outer surface area of the entire, single tube, $P_o$ outer perimeter of the tube, $L_x$ means length of the entire, single tube, $\Delta A_o$ outer surface area of the tube for the single control volume.

Rewriting Eqs. (4.28) and assuming that the overall heat transfer coefficient $U_o$ and mass flow rate $\Delta \dot{m}_a$ depends on the $x$ coordinate. Then, Eq. (4.27) takes the form

$$\Delta N_{a,i} = \frac{U_{o,i} \Delta A_o}{\Delta \dot{m}_{a,i} \overline{c}_{p,a,i}} \tag{4.29}$$

Eq. (4.27) allows calculating the air temperature behind the particular row of tubes in the one and multi-rows PFTHE. Additionally, by integrating the Eq. (4.27) can be obtained the formula for the mean air temperature in a single row.

$$\begin{aligned} \overline{T}_{a,i} = \frac{1}{p_l} \int_0^{p_l} T_a(y) dy = \\ &= \overline{T}_{w,i} - (\overline{T}_{w,i} - T'_{a,i}) \int_0^{p_l} exp\,(-\frac{U_{o,i} \Delta x}{\Delta \dot{m}_{a,i} \overline{c}_{p,a,i}} y) dy = \\ &= \overline{T}_{w,i} - (\overline{T}_{w,i} - T'_{a,i})\,(-\frac{\Delta \dot{m}_{a,i} \overline{c}_{p,a,i}}{U_{o,i} \Delta x\, p_l})\,[exp\,(-\frac{U_{o,i} \Delta x\, p_l}{\Delta \dot{m}_{a,i} \overline{c}_{p,a,i}}) - 1] \end{aligned} \tag{4.30}$$

The average air temperature Eq. 4.30 can be simplified to the form

$$\overline{T}_{a,i} = \overline{T}_{w,i} - \frac{1}{\Delta N_{a,i}} (\overline{T}_{w,i} - T'_{a,i})[1 - \; exp\,(-\Delta N_{a,i})] \tag{4.31}$$

The overall HTC $U_{o,i}$ that contains the air-side HTC $\alpha_a$ (4.8) can be determined using CFD simulation or experiment. The water-side HTC is mainly calculated using experimental correlations available in the literature.

### 4.2.2 Determination of the Liquid Temperature Distribution

An energy conservation equation for the water-side for a single control volume (Fig. 4.2) can be written

$$\dot{m}_w \overline{c}_{w,i} (T_{w,i+1} - T_{w,i}) = -U_{o,i}\, \Delta A_o (\overline{T}_{w,i} - \overline{T}_{a,i}) \tag{4.32}$$

Detailing the water-side average temperature $\overline{T}_{w,i}$

$$\overline{T}_{w,i} = \frac{T_{w,i} + T_{w,i+1}}{2} \tag{4.33}$$

Considering the water-side average specific heat $\overline{c}_{w,i}$ as

$$\overline{c}_{w,i} = \frac{c_w(T_{w,i}) + c_w(T_{w,i+1})}{2} \tag{4.34}$$

Additionally, defining the average water-side number of transfer units $\Delta N_{w,i}$ with Eq. (4.34)

$$\Delta N_{w,i} = \frac{U_{o,i}\,\Delta A_o}{\dot{m}_w \overline{c}_{w,i}} = \frac{2U_{o,i}\,\Delta A_o}{\dot{m}_w[c_w(T_{w,i}) + c_w(T_{w,i+1})]} \tag{4.35}$$

The water temperature behind the control volume $T_{w,i+1}$, obtained from Eq. (4.32) and taking int account Eqs. (4.33) and (4.35) is presented as

$$T_{w,i+1} = T_{w,i} + \Delta N_{w,i}(\overline{T}_{a,i} - \overline{T}_{w,i}), \qquad i = 1, \ldots, N \tag{4.36}$$

The proposed algebraic equations are related to the nonlinear model of the PFTHE. Entangled equation Eq. (4.36) was calculated using the Gauss-Seidel method. It was assumed that the initial value of the temperature in all nodes equals the inlet air or water temperature, i.e.

$$T_{w,i}^{(0)} = T_w^{'}, \qquad i = 1, \ldots, N, \qquad i = 1, \ldots, N+1 \tag{4.37}$$

$$T_{a,i}^{(0)} = T_a^{'}, \qquad i = 1, \ldots, N, \qquad i = 1, \ldots, N \tag{4.38}$$

### 4.2.3 Determination of tube wall temperature

Once the temperatures $\overline{T}_{a,i}$ and $\overline{T}_{w,i}$ have been determined using Gauss-Seidel, the temperature of the inner and outer surface of the tube in each finite volume can be calculated. The mean heat flux $\dot{q}_{o,i}$ along the length of the $i$-th finite volume on the outer surface of the bare tube is given by

$$\dot{q}_{o,i} = U_{o,i}(\overline{T}_{w,i} - \overline{T}_{a,i}) \tag{4.39}$$

The mean temperature $\overline{T}_{to,i}$ of the outer tube surface over the length of the $i$-th finite volume is calculated using the following formula

$$\overline{T}_{to,i} = \overline{T}_{w,i} - \dot{q}_{o,i}(\frac{1}{\alpha_w}\frac{r_o}{r_{in}} - \frac{r_o}{\lambda_t} ln \frac{r_o}{r_{in}}) = \overline{T}_{a,i} + \frac{\dot{q}_{o,i}}{\alpha_{eq}} \tag{4.40}$$

The mean temperature $\overline{T}_{tin,i}$ of the tube inner surface over the length of the $i$-th finite volume is calculated using the following formula

$$\overline{T}_{tin,i} = \overline{T}_{w,i} - \frac{\dot{q}_{o,i}}{\alpha_w}\frac{r_o}{r_{in}} = \overline{T}_{a,i} + \frac{\dot{q}_{o,i}}{\alpha_{eq}} + \frac{\dot{q}_{o,i} r_o}{\lambda_t} ln \frac{r_o}{r_{in}} \tag{4.41}$$

## 4.3 Calculation of the equivalent air-side heat transfer coefficient

The equivalent air-side heat transfer coefficient is used, e.g., in the overall heat transfer coefficient $U_o$ in the plate fin and tube heat exchanger. The overall heat transfer coefficient is calculated using the following formula:

$$\frac{1}{U_o} = \frac{1}{\alpha_{eq}} + \frac{A_o}{A_{in}}\frac{\delta_t}{\lambda_t} + \frac{A_o}{A_{in}}\frac{1}{\alpha_w} \tag{4.42}$$

$\alpha_{eq}$ the equivalent air-side heat transfer coefficient considering the fins attached to the tube, $A_{in}$ the area of the inner surface of the tube, $\delta_t$ the thickness of the wall of the tube, $\lambda_t$ the thermal conductivity of the tube material, $\alpha_w$ the water-side heat transfer coefficient. The equivalent air-side HTC in Eq. 4.8 $\alpha_{eq}$ is calculated using the mean value of the HTC in the entire row of the tube.

$$\alpha_{eq} = \alpha_a[\frac{A_{bf}}{A_o} + \frac{A_f}{A_o}\eta_f(\alpha_a)] \tag{4.43}$$

where $A_{bf}$ area of the outer tube surface between the fins, $A_f$ surface area of the fins, $\eta_f(\alpha_a)$ fin efficiency.

### 4.3.1 Fin efficiency of complex-shaped fins

Many devices use finned surfaces, including radiators for automobiles, electronic parts, HVAC systems, and power plants [3]. Harper and Brown [121] in 1922 introduced the first sources for measuring the efficiency of finned surfaces. At this point, it has been extensively discussed how to calculate the efficiency of fins with both basic and complex shapes. Bošnjaković et al. [122] comparison of analytical and numerical approaches of the annular fin. The more intricate research by Jing et al. [123] on the air-water heat exchanger for the data center used the calculation of the fin efficiency of a serrated form of the finned surface. The calculation of the area of stepped fins' effectiveness on the performance improvement of phase change thermal energy storage.

The efficiency of a fin is the ratio of the heat flux exchanged by the fin with the environment $\dot{Q}$ to the maximum heat flux $\dot{Q}_{max}$ that would flow between the fin and the environment if the temperature of the entire fin was equal to the temperature of the base of the fin $T_b$.

$$\eta_f = \frac{\dot{Q}}{\dot{Q}_{max}} \tag{4.44}$$

The heat flux $\dot{Q}$ is given by the formula:

$$\dot{Q} = \int_{A_f} \alpha(T - T_f)\, dA \tag{4.45}$$

where $\alpha$ is the air-side heat transfer coefficient on the surface of the fin and $A_f$ is the area of the surface of the fin on which the heat exchange occurs. When the heat transfer

coefficient $\alpha$ and the ambient temperature $T_f$ are constant, then the expression Eq. (4.45) can be written in the form:

$$\dot{Q} = \alpha A_f(\overline{T} - T_f) \tag{4.46}$$

where $\overline{T}$ is the average temperature of the fin surface calculated from the formula:

$$\overline{T} = \frac{\int_{A_f} T\, dA}{\sum_{i=1}^{N_e} A_{e,i}} = \frac{\sum_{i=1}^{N_e} \overline{T}_{e,i} A_{e,i}}{A_f} \tag{4.47}$$

where $T$ is the temperature of the surface of the fin in contact with the fluid, and $T_{e,i}$ is the average temperature of the finite element surface. The symbol $N_e$ denotes the number of finite elements on the surface on which heat exchange takes place. $A_{e,i}$ is the fin surface of the $i$-th number of finite elements and $A_f$ is the total fin surface. The maximum heat flux $\dot{Q}_{max}$ is defined by the formula:

$$\overline{T} = \alpha A_f(T_b - T_f) \tag{4.48}$$

After substituting Eq. (4.47) and Eq. (4.48) in Eq. (4.44), a simple formula for calculating the efficiency of the fin is obtained:

$$\eta = \frac{\overline{T} - T_f}{T_b - T_f} \tag{4.49}$$

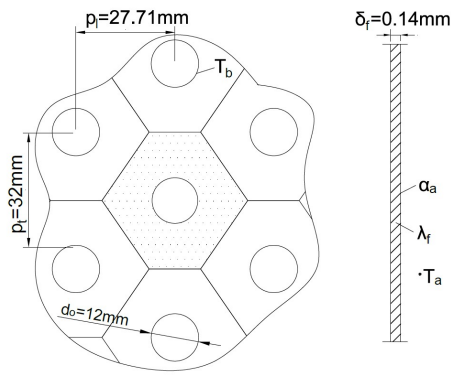


Figure 4.3: Conventional hexagonal fin determined from the continuous fin found in plate fin and tube heat exchangers for staggered tube arrangement.

In other words, it can be described as the ratio of the differences between the average fin temperature $\overline{T}$ and the ambient temperature $T_f$ to the difference between the base fin temperature and the ambient temperature $T_f$. For basic forms, such as straight or circular fins, it is possible to determine the precise value of fin efficiency [124]. However, we must use approximate analytical techniques, such as the Schmidt method [125] or the sector method [126] for complex designs such as virtual rectangular or virtual hexagonal fins. Additionally, only numerical methods, such as the finite element method (FEM) or

the finite volume method (FVM), can be used for more complicated designs, such as segmented or extended hexagonal shapes. For both basic and complex fin forms, numerical approaches are used to assess the fin's effectiveness [127]. Numerous fin shapes, including triangles, squares, rectangles, polygons, and trapezoids, have thus far been studied in steady state by Osorio et al. [128] using FEM and FVM.

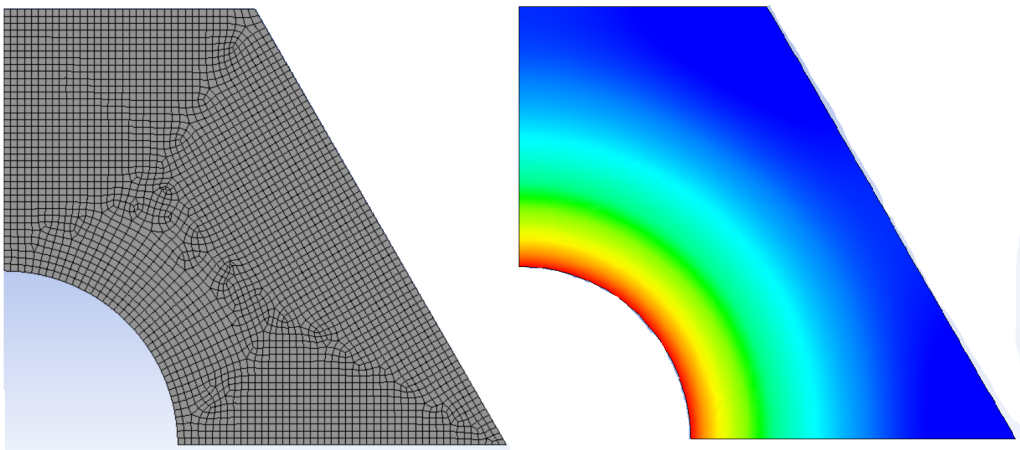

Figure 4.4: Division of the fin model into finite elements and temperature distribution on the fin surface.

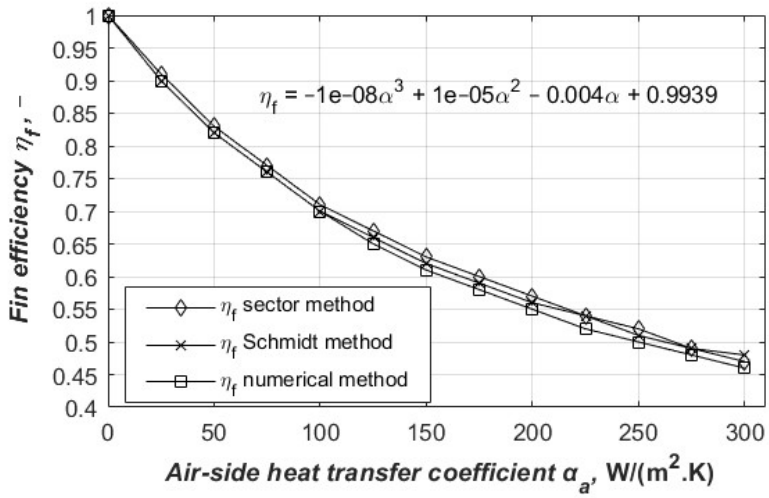


Figure 4.5: Fin efficiency as a function of the air-side heat transfer coefficient.

The plate fin and tube heat exchangers consist of tubes and metal sheets. One of the metal sheets is called a continuous fin. Simplifications have been in the calculations of plate-fin and tube heat exchangers that allow for calculating the efficiency of such fins. The continuous fin was divided into smaller imaginary fins attached to individual tubes (Fig. 4.3). In calculating the temperature distribution in the fin using the finite element method, it is easy to consider the dependence of the heat transfer coefficient on the location, time, or temperature of the fin. The use of Ansys Fluent software will be illustrated

by the example of determining the efficiency of a fin with complex geometry, shown in Fig. 4.3 and comparing it to the calculation methods such as sector and Schmidt's method in Fig. 4.5.

Two-dimensional temperature field of the conventional fin quadrant on 2904 finite elements (Fig. 4.4). Then, the average temperature of the fin surface $\overline{T}$, where the exchange of heat with the environment takes place, and the efficiency of the fin $\eta_f$ was determined. Fig. 4.5 shows the efficiency of the fin $\eta_f$ as a function of the air-side heat transfer coefficient $\alpha_a$. Analysis of the fin temperature field shows that the largest temperature gradient occurs just at the base of the fin (Fig. 4.4). The thermal parameters used for the calculation were: $T_b$ = 373.15 K, $T_f$ = 273.15 $K$ and $\lambda_f$ = 204 $\frac{W}{mK}$.

## 4.4 Numerical model of the heat exchanger considers different air-side Nusselt number correlations on different tube rows

### 4.4.1 Development of a numerical model of the heat exchanger considering different formulas for the air-side Nusselt number on different tube rows

A numerical model was created based on the mathematical model presented in chapter 4.2. A numerical model was used for the four-row plate fin and tube heat exchanger, which is commonly used as a heater or cooler in ventilation or air conditioning. The model is for the simulation of a heat exchanger operation in the steady state condition. The heat exchanger contains continuous aluminum fins slipped on copper circular tubes. Tubes are in staggered arrangements. Each row contains 11 tubes. tube spacing divisions are: transverse ($p_t$) 32 mm, longitudinal ($p_l$) 27.71 mm. The outer diameter of tubes ($d_o$) is 12 mm. The wall thickness of the tubes ($\delta_t$) is 0.35 mm. The plate fins have a width ($\delta_f$) of 0.14 mm and their pitch (module) ($s$) is 3 mm. The number of fins ($n_{ft}$) on one tube is 200 pieces. The width of the exchanger ($L_x$) is 0.6 m and the height ($H$) is 0.35 m. A detailed production description can be found on the manufacturer's website [109].

Hot water flows through the exchanger only once, that is, there is one flow from the input manifold to the output manifold (Fig. 4.6). Air flows transversely to the axis of the horizontal tubes of the exchanger. The input data for calculating the exchanger are:

- Volume flow of water at the inlet to the exchanger $\dot{V}_w(t)$.
- Inlet temperature of water at the exchanger $T_w(t)$.
- Inlet air volume flow rate at the exchanger $\dot{V}_a(t)$.
- Inlet air temperature at the exchanger $T'_w(t)$.

The mass flux of water flowing through the cooler is calculated based on known input

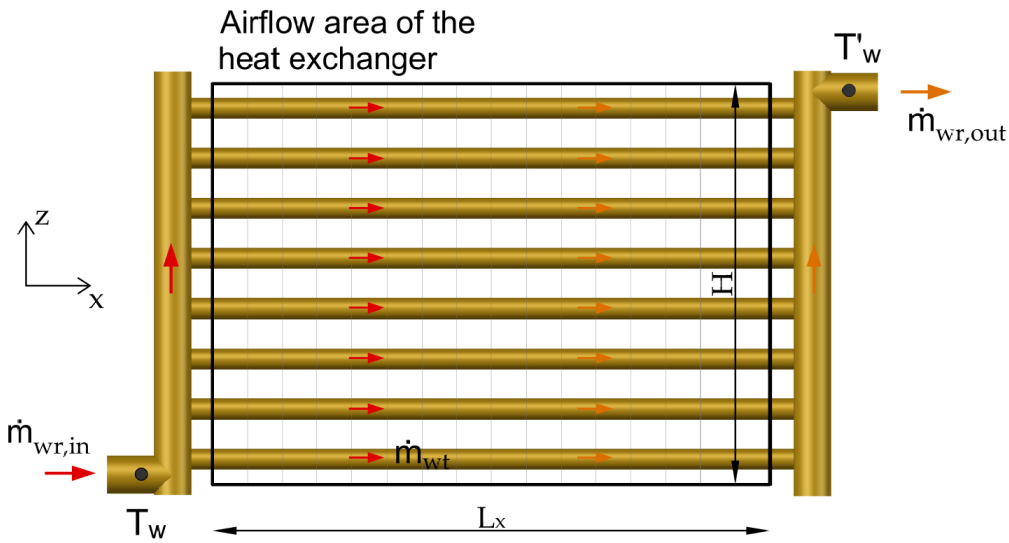


Figure 4.6: Flow system of a 4-row heat exchanger showing the flow of water in one row from the supply to the return manifold.

values $\dot{V}_w(t)$, $T_w(t)$.

$$\dot{m}_w(t) = \dot{V}_w(t)\rho(T'_w(t)) \tag{4.50}$$

The exchanger has 4 rows ($n_r$), so the flux of water flowing through one row denotes $\dot{m}_{wr}$ (Eq. 4.51) Additionally, each row has 11 tubes ($n_t$), so the flux of water flowing through one tube denotes $\dot{m}_{wt}$ (Eq. 4.52).

$$\dot{m}_{wr} = \frac{\dot{m}_w}{n_r} \tag{4.51}$$

$$\dot{m}_{wt} = \frac{\dot{m}_r}{n_t} \tag{4.52}$$

The mass flux of air $\dot{m}_a(t)$ flowing through the coolers is determined from the formulas:

$$\dot{m}_a(t) = \dot{V}_a(t)\rho\left[T_{a,0}(t)\right] \tag{4.53}$$

where the air volume flux $\dot{V}_a(t)$ in front of the cooler is given by the formula:

$$\dot{V}_a(t) = w_o L_x H \tag{4.54}$$

The symbols $L_x$ and $H$ denote the width and height of the active section of the heater, respectively. The speed of airflow in front of the exchanger (Fig. 4.7) in a duct with a rectangular cross-section can be calculated:

$$w_o = \frac{\dot{V}_a(t)}{L_x H} \tag{4.55}$$

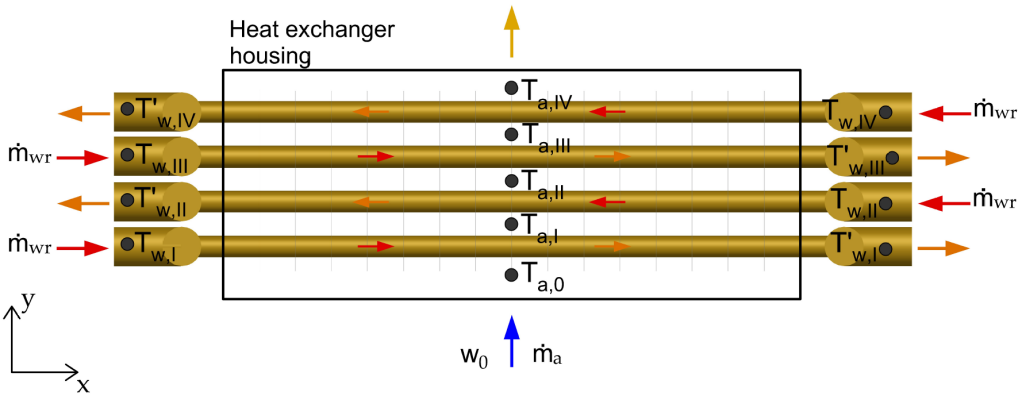


Figure 4.7: Flow system of a 4-row heat exchanger showing the flow of water in each row from the supply to the return manifold.

The air mass flux per tube $\dot{m}_{a,t}$ is:

$$\dot{m}_{a,t} = \frac{\dot{m}_a}{n_t} = w_0 p_l L_x \rho \left[T_a^0(t)\right] \tag{4.56}$$

To calculate the air-side heat transfer coefficient ($\alpha_a$) for each row individually, proprietary correlations determined by CFD modeling were used and experimentally verified. Correlations were approximated using the function (Eq. 4.57). The coefficients $x_1$ and $x_2$ necessary for the correlations are presented in chapter 3.8 in Tab. 3.12.

$$Nu_a = x_1 Re_a^{x_2} Pr_a^{1/3} \quad 200 \leq Re_a \leq 6000 \tag{4.57}$$

Correlations on the water-side Nusselt number that exist in the literature can cause considerable calculation uncertainties because they have been determined for straight tube sections. In fact, tubular heat exchangers exhibit significant turbulence due to bends or changes in the direction of the water supply pipe to the exchanger. Thus, if the calculated value of the heat transfer coefficient is too high, the value of the heat transfer coefficient on the air-side will be underestimated, and vice versa. Therefore, the correlation of Taler and Taler [90] was used, which was determined for a heat exchanger with a complex structure.

$$\begin{gathered} Nu_w = 0.01253 Re_w^{0.8413} Pr_w^{0.6179} \left[1 + (\frac{d_i}{L_x})^{2/3}\right] \\ 3000 \leq Re_w \leq 10^6 \quad 1 < Pr_w \leq 3 \end{gathered} \tag{4.58}$$

$$\begin{gathered} Nu_w = 0.00881 Re_w^{0.8991} Pr_w^{0.3911} \left[1 + (\frac{d_i}{L_x})^{2/3}\right] \\ 3000 \leq Re_w \leq 10^6 \quad 3 < Pr_w \leq 1000 \end{gathered} \tag{4.59}$$

where $Nu$ denotes the Nusselt number, $Re$ the Reynolds number and, $Pr$ the Prandtl number. The subscript $a$ denotes the value for air and $w$ for water. For $Nu$ and $Re$ numbers on the air-side, the hydraulic diameter $d_h$ was used, and additionally in the Reynolds

number, the maximum air velocity $w_{max}$ occurring in the exchanger in the smallest cross-section $A_{min}$ between the tubes was considered. The symbol $d_o$ ,$d_i$ denotes the outer and inner diameter of the circular tube. The symbol $L_x$ denotes the length of the tube in the exchanger. The Reynolds number on the air-side $Re_a$ is determined by the formula:

$$Re_a = \frac{w_{max} d_h}{\nu_a} \tag{4.60}$$

where $w_{max}$ is the maximum air flow velocity in the exchanger, $d_h$ is the equivalent hydraulic diameter calculated according to the formulas of Kays and London [1].

$$d_h = \frac{4V_o}{A} \tag{4.61}$$

$$V_o = V_a - V_t \tag{4.62}$$

$$A = A_f + A_t \tag{4.63}$$

The volume through which air flows in a single row is denoted by the symbol $V_o$. The total area in a single row is represented by the letter $A$. Other symbols stand for: $V_a$ is the overall volume of a row, $V_t$ is the volume of tubes in one row, $A_f$ is the area occupied by the fins in one fin pitch, and $A_t$ is the space of the bare tubes in a row between the two fins directly above it.

$$V_a = p_l p_t (s - \delta_f) \tag{4.64}$$

$$V_t = \pi (\frac{d_o}{2})^2 (s - \delta_f) \tag{4.65}$$

$$A_f = 2 \left[ p_l p_t - \pi (\frac{d_o}{2})^2 \right] \tag{4.66}$$

$$A_t = \pi d_o (s - \delta_f) \tag{4.67}$$

The transverse fin pitch is designated by the letter $p_t$, while the longitudinal fin pitch is indicated by the character $p_l$. Other symbols represent: $s$ the fin pitch, $\delta_f$ the fin thickness, $d_o$ the tube's outer diameter. Eq. (4.68) shows Eq. (4.61) in its form, including Eqs. (4.64)-(4.67). The hydraulic diameter in the case of PFTHE is equal to 5.35 mm and typically has a slightly lower than the double fin pinch.

$$d_h = \frac{4(s - \delta_f)(p_l p_t - \pi (\frac{d_o}{2})^2)}{2 \left[ p_l p_t - \pi (\frac{d_o}{2})^2 \right] + (\pi d_o)(s - \delta_f)} \tag{4.68}$$

Due to the staggered arrangement of tubes in the exchanger and the dimensions of the transverse and longitudinal pitches of the tubes, the maximum velocity $w_{max}$ occurs in the transverse plane between two consecutive tubes in a row. In addition, the air velocity when flowing through the exchanger increases because of its heating from the inlet temperature $T_a^i$ to the temperature $T_a^{i+1}$ occurring behind each row. Assuming an average air temperature over the thickness of one row $\overline{T}_a^i = (T_a^i + T_a^{i+1})/2$, the maximum air velocity is given by the formula:

$$w_{max} = \frac{(sp_l)}{(s-\delta_f)(p_l - d_{o,min})} \frac{\overline{T}_a^i}{\overline{T}_a^0} w_0 \tag{4.69}$$

The air velocity in the smallest cross-section of the airflow is represented by the symbol $w_{max}$. Other symbols are shown: $d_{o,min}$ the minimum distance between tubes, $\overline{T}_{0,a}$ the average air temperature of the inlet mass, $\overline{T}_a^i$ the average air temperature of the mass in the $i$-th row of the PFTHE, and $w_0$ the air velocity in front of the PFTHE.

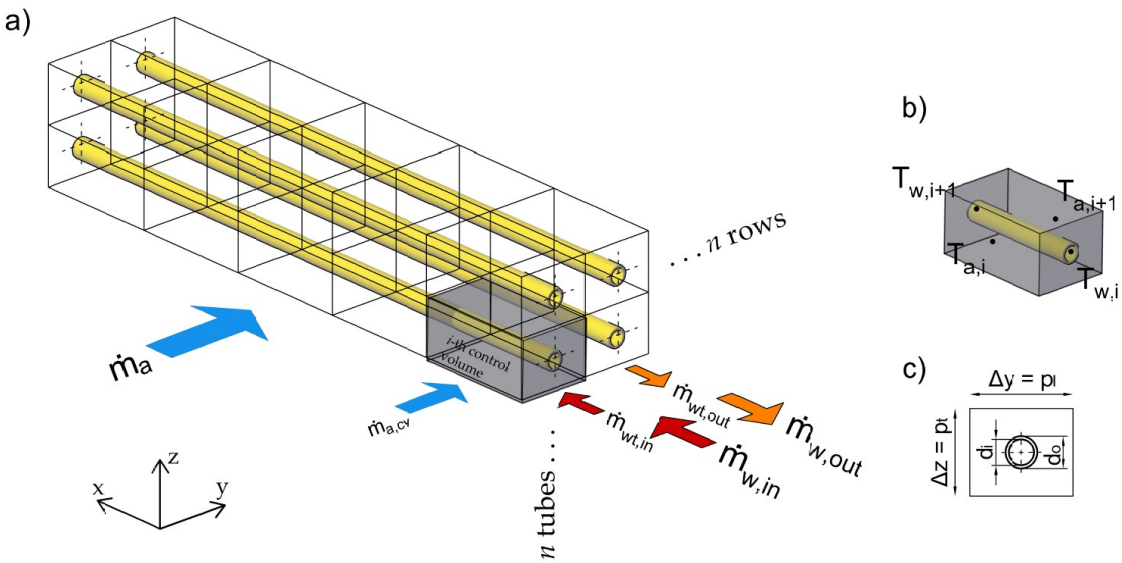


Figure 4.8: a) Air and water flow diagram.; b) Air and water temperature in one control volume.; c) Dimensions of one control volume.

Fig. 4.8 presents the division entire heat exchanger to control volumes. The mathematical model calculates outlet air temperature and water outlet temperature $T_w^{i+1}$ for each control volume. Each tube in the heat exchanger is divided into 5 control volumes per row. Broadly investigation in this work shows that 5 control volumes are enough to acquire temperature results differ less than 1 % that from the higher number of the control volume. The entire procedure is precisely described in chapter 4.2.

### 4.4.2 Testing of the developed model

The results obtained using the numerical modeling methods presented were compared with the method based on CFD simulation described in chapter 3.6.3 and the experiment described in chapter 7. In the numerical modeling performed, each exchanger tube was divided into five control volumes, and the results were compared for the following data set: $\dot{V}_w$ = 7.88 l/min, $T_a^0$ = 23 $°C$, $T_w^0$ = 63 $°C$. The above values are average values from the entire set of experiments. The air velocity in front of the exchanger $w_0$ varied from 0.47 to 4.91 m/s. The accuracy of the obtained results was evaluated by calculating the relative error of Nusselt numbers.

| $w_0$ | **CFD Model 3** | | | | **Experiment** | | | | **Numerical Model** | | | |
|---|---|---|---|---|---|---|---|---|---|---|---|---|
| | $T_{a,I}$ | $T_{a,II}$ | $T_{a,III}$ | $T_{a,IV}$ | $T_{a,I}$ | $T_{a,II}$ | $T_{a,III}$ | $T_{a,IV}$ | $T_{a,I}$ | $T_{a,II}$ | $T_{a,III}$ | $T_{a,IV}$ |
| $[m/s]$ | $[°C]$ | $[°C]$ | $[°C]$ | $[°C]$ | $[°C]$ | $[°C]$ | $[°C]$ | $[°C]$ | $[°C]$ | $[°C]$ | $[°C]$ | $[°C]$ |
| 0.47 | 41.94 | 51.86 | 56.22 | 58.89 | 40.41 | 49.17 | 54.86 | 58.55 | 40.43 | 49.10 | 54.98 | 58.60 |
| 1.11 | 32.72 | 38.81 | 43.20 | 46.59 | 31.59 | 37.84 | 42.44 | 46.24 | 31.73 | 37.93 | 42.58 | 46.47 |
| 1.45 | 32.67 | 39.03 | 43.95 | 47.88 | 31.84 | 38.46 | 43.61 | 47.99 | 32.06 | 38.93 | 44.01 | 48.37 |
| 2.06 | 29.74 | 34.79 | 38.81 | 42.26 | 29.28 | 34.44 | 38.69 | 42.49 | 29.49 | 34.74 | 38.91 | 42.64 |
| 2.55 | 29.42 | 33.98 | 37.59 | 40.84 | 29.12 | 33.70 | 37.59 | 41.08 | 29.24 | 33.88 | 37.71 | 41.14 |
| 3.13 | 27.61 | 31.97 | 35.40 | 38.59 | 27.62 | 32.12 | 36.05 | 39.67 | 27.65 | 32.16 | 35.98 | 39.50 |
| 4.07 | 26.22 | 29.47 | 32.01 | 34.55 | 26.18 | 29.45 | 32.39 | 35.12 | 26.25 | 29.56 | 32.45 | 35.14 |
| 4.91 | 25.81 | 28.41 | 30.59 | 32.83 | 25.78 | 28.42 | 30.83 | 33.09 | 25.86 | 28.60 | 31.05 | 33.34 |

Table 4.1: Comparison of the air temperature behind each row in heat exchanger for CFD method 3, experiment and numerical model.

| $w_0$ | **CFD Model 3** | | | | **Experiment** | | | | **Numerical Model** | | | |
|---|---|---|---|---|---|---|---|---|---|---|---|---|
| | $Q_{a,I}$ | $Q_{a,II}$ | $Q_{a,III}$ | $Q_{a,IV}$ | $Q_{a,I}$ | $Q_{a,II}$ | $Q_{a,III}$ | $Q_{a,IV}$ | $Q_{a,I}$ | $Q_{a,II}$ | $Q_{a,III}$ | $Q_{a,IV}$ |
| $[m/s]$ | $[W]$ | $[W]$ | $[W]$ | $[W]$ | $[W]$ | $[W]$ | $[W]$ | $[W]$ | $[W]$ | $[W]$ | $[W]$ | $[W]$ |
| 0.47 | 2007.0 | 895.3 | 517.1 | 265.3 | 1790.9 | 946.6 | 605.9 | 388.5 | 1792.7 | 938.2 | 624.4 | 381.9 |
| 1.11 | 2330.5 | 1516.5 | 1135.2 | 857.0 | 2166.5 | 1642.0 | 1194.2 | 984.3 | 2203.3 | 1630.8 | 1208.0 | 1004.8 |
| 1.45 | 2996.9 | 2099.9 | 1624.0 | 1296.3 | 2884.7 | 2274.3 | 1741.3 | 1476.6 | 2962.9 | 2357.4 | 1720.3 | 1468.3 |
| 2.06 | 3050.5 | 2368.4 | 1890.8 | 1620.5 | 3034.6 | 2552.1 | 2077.5 | 1847.9 | 3138.7 | 2597.5 | 2040.7 | 1815.8 |
| 2.55 | 3204.4 | 2642.4 | 2096.1 | 1886.4 | 3244.3 | 2816.0 | 2360.8 | 2114.0 | 3315.9 | 2852.4 | 2326.5 | 2077.8 |
| 3.13 | 3533.5 | 3115.5 | 2448.8 | 2280.6 | 3815.5 | 3430.1 | 2955.0 | 2715.6 | 3841.5 | 3432.0 | 2877.5 | 2636.4 |
| 4.07 | 3248.6 | 3023.8 | 2363.6 | 2356.1 | 3494.2 | 3270.0 | 2912.9 | 2691.8 | 3560.7 | 3308.7 | 2872.7 | 2656.8 |
| 4.91 | 3533.5 | 3115.5 | 2448.8 | 2280.6 | 3338.1 | 3147.4 | 2851.0 | 2655.7 | 3427.9 | 3269.6 | 2895.8 | 2698.4 |

Table 4.2: Comparison of the air temperature behind each row in heat exchanger for CFD method 3, experiment and numerical model.

Tab. 4.1 shows the results of the air temperature behind each row in the heat exchanger for CFD method 3, experiment, and numerical model in the exchanger for the tested range of air velocities upstream of the exchanger. The calculations were performed using a numerical model, CFD simulation, and experimental verification. The air heat flux for an individual row using the above methods is shown in Tab. 4.2. The relative error in calculating the air heat flux for an individual row using the above methods is shown in Tab. 4.3. The equations that were used to calculate the relative difference (error) of the heat flux between the numerical model and CFD model $e^{CFD}_{\dot{Q}_a}$ and experiment $e^{exp}_{\dot{Q}_a}$ are as follows:

$$e^{CFD}_{\dot{Q}_a} = \frac{\dot{Q}^{num}_a - \dot{Q}^{CFD}_a}{\dot{Q}^{num}_a} 100\% \tag{4.70}$$

$$e^{exp}_{\dot{Q}_a} = \frac{\dot{Q}^{num}_a - \dot{Q}^{exp}_a}{\dot{Q}^{num}_a} 100\% \tag{4.71}$$

where $\dot{Q}^{num}_a$, $\dot{Q}^{CFD}_a$ and $\dot{Q}^{exp}_a$ are heat fluxes obtained from a numerical model, CFD simulation and experiment respectively.

| $w_0$ | **CFD Model 3 vs Numerical Model** | | | | **Experiment vs Numerical Model** | | | |
|---|---|---|---|---|---|---|---|---|
| $[m/s]$ | $e^{CFD}_{Q_{a,I}}$ **[%]** | $e^{CFD}_{Q_{a,II}}$ **[%]** | $e^{CFD}_{Q_{a,III}}$ **[%]** | $e^{CFD}_{Q_{a,IV}}$ **[%]** | $e^{exp}_{Q_{a,I}}$ **[%]** | $e^{exp}_{Q_{a,II}}$ **[%]** | $e^{exp}_{Q_{a,III}}$ **[%]** | $e^{exp}_{Q_{a,IV}}$ **[%]** |
| 0.47 | 10.8 | -5.7 | -17.2 | -46.4 | -0.1 | 0.9 | -3.1 | 1.7 |
| 1.11 | 7.0 | -8.3 | -5.2 | -14.9 | -1.7 | 0.7 | -1.2 | -2.1 |
| 1.45 | 3.7 | -8.3 | -7.2 | -13.9 | -2.7 | -3.7 | 1.2 | 0.6 |
| 2.06 | 0.5 | -7.8 | -9.9 | -14.0 | -3.4 | -1.8 | 1.8 | 1.7 |
| 2.55 | -1.2 | -6.6 | -12.6 | -12.1 | -2.2 | -1.3 | 1.5 | 1.7 |
| 3.13 | -8.0 | -10.1 | -20.7 | -19.1 | -0.7 | -0.1 | 2.6 | 2.9 |
| 4.07 | -7.6 | -8.1 | -23.2 | -14.2 | -1.9 | -1.2 | 1.4 | 1.3 |
| 4.91 | 5.5 | -1.0 | -16.4 | -16.4 | -2.7 | -3.9 | -1.6 | -1.6 |

Table 4.3: Comparison of relative errors using the developed models and methods.

From the analysis of the results in Tab. 4.1, Tab. 4.2 and Tab. 4.3, it can be seen that the accuracy of the proposed numerical method based on the finite volume method is very accurate. The results obtained with this model do not significantly differ from the CFD simulation and experimental verification. The advantage of this model is the ease of modeling heat exchangers with complex flow systems characterized by many rows and tubes. The temperature dependence of the physical properties of the media can also be considered in a fairly simple way. A program featuring a graphical user interface was additionally developed to accompany the numerical method, showcasing the model's exceptional adaptability and user-friendliness (Fig. 4.9).

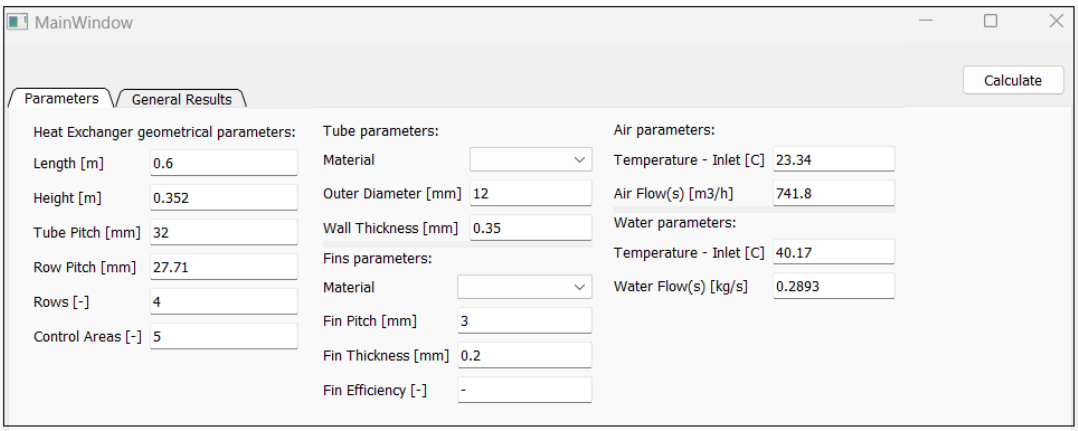


(a)

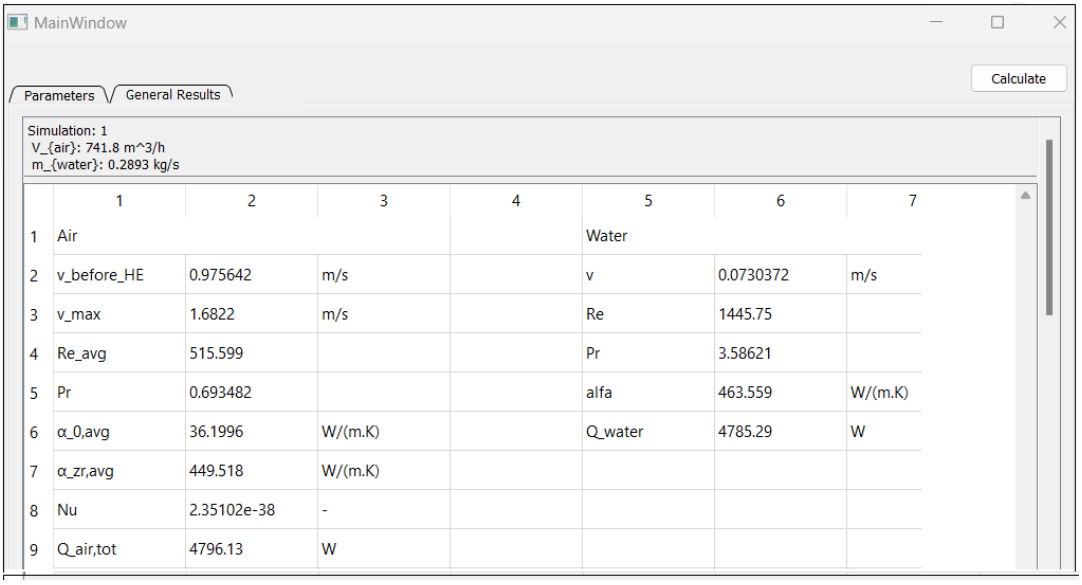


| | 1 | 2 | 3 | 4 | 5 | 6 | 7 |
|---|---|---|---|---|---|---|---|
| 1 | Air | | | | Water | | |
| 2 | v_before_HE | 0.975642 | m/s | | v | 0.0730372 | m/s |
| 3 | v_max | 1.6822 | m/s | | Re | 1445.75 | |
| 4 | Re_avg | 515.599 | | | Pr | 3.58621 | |
| 5 | Pr | 0.693482 | | | alfa | 463.559 | W/(m.K) |
| 6 | α_0,avg | 36.1996 | W/(m.K) | | Q_water | 4785.29 | W |
| 7 | α_zr,avg | 449.518 | W/(m.K) | | | | |
| 8 | Nu | 2.35102e-38 | - | | | | |
| 9 | Q_air,tot | 4796.13 | W | | | | |

(b)

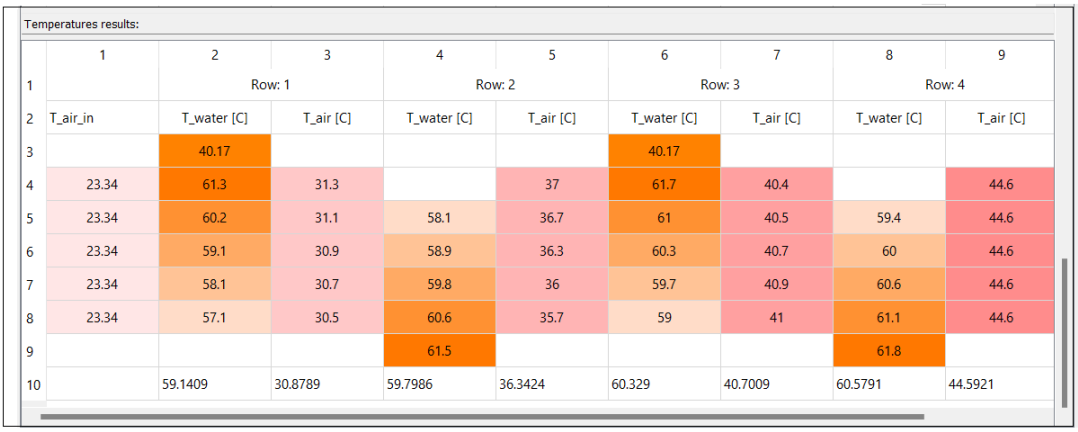


| | 1 | 2 | 3 | 4 | 5 | 6 | 7 | 8 | 9 |
|---|---|---|---|---|---|---|---|---|---|
| 1 | | Row: 1 | | Row: 2 | | Row: 3 | | Row: 4 | |
| 2 | T_air_in | T_water [C] | T_air [C] | T_water [C] | T_air [C] | T_water [C] | T_air [C] | T_water [C] | T_air [C] |
| 3 | | 40.17 | | | | 40.17 | | | |
| 4 | 23.34 | 61.3 | 31.3 | | 37 | 61.7 | 40.4 | | 44.6 |
| 5 | 23.34 | 60.2 | 31.1 | 58.1 | 36.7 | 61 | 40.5 | 59.4 | 44.6 |
| 6 | 23.34 | 59.1 | 30.9 | 58.9 | 36.3 | 60.3 | 40.7 | 60 | 44.6 |
| 7 | 23.34 | 58.1 | 30.7 | 59.8 | 36 | 59.7 | 40.9 | 60.6 | 44.6 |
| 8 | 23.34 | 57.1 | 30.5 | 60.6 | 35.7 | 59 | 41 | 61.1 | 44.6 |
| 9 | | | | 61.5 | | | | 61.8 | |
| 10 | | 59.1409 | 30.8789 | 59.7986 | 36.3424 | 60.329 | 40.7009 | 60.5791 | 44.5921 |

(c)

Figure 4.9: Graphical interface of the developed numerical model in C++ programming language: a) Data input visualization. b) Results - parameters. c) Air and water temperatures at the inlet and outlet of each control volume.

This interface allows for effortless manipulation of input parameters, enabling users to perform various calculations pertaining to alterations in media temperature, determination of the heat transfer coefficient, and evaluation of the power distribution within individual rows and the entire system.

The interface provides an intuitive and user-friendly platform, empowering researchers and engineers to efficiently explore the dynamic behavior of the system under diverse scenarios. Through the trouble-free adjustment of input parameters, users can instantaneously assess the effects of varying different variables on the system's thermal performance. The development of a sophisticated graphical interface adds an extra layer of universality and ease of use to the numerical method, expanding its applications across various research and engineering fields.

# 5 Thermal and flow test facility description

This chapter discusses the construction of the test bed, along with brief characteristics of its basic components. The hydraulic system, automation system, and measurement system are presented. Next, the methods of measuring air velocity and air and water temperatures are presented.

## 5.1 Description of the test stand construction

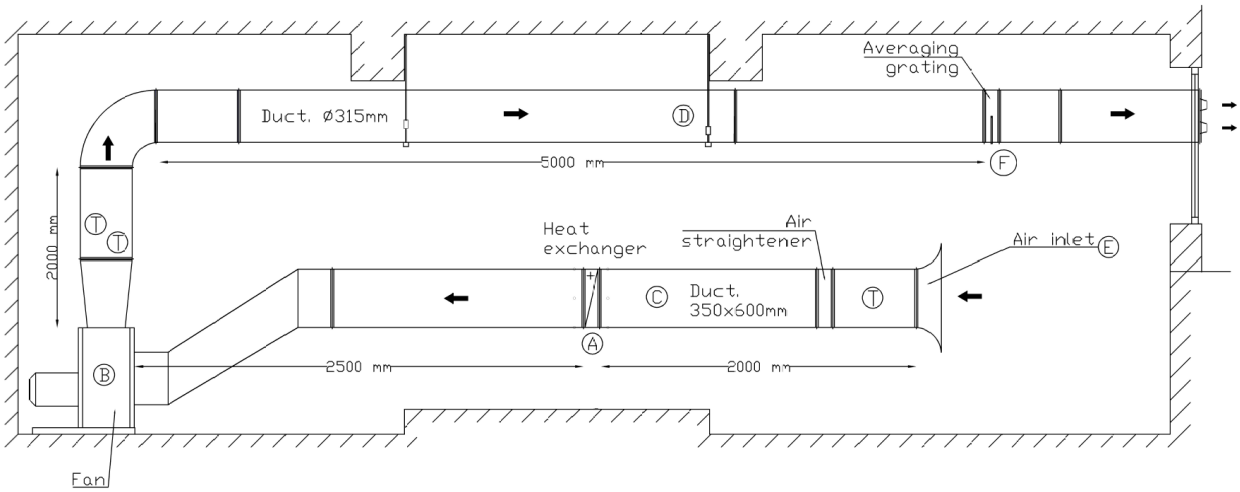


Figure 5.1: Diagram of the airflow; A - heat exchanger, B - fan, C - rectangular duct 350 x 600 mm, D - circular duct ⌀ 315 mm, E - flanged starting element, F - airflow averaging grating, T - air temperature sensors.

The described experimental setup consists of several interconnected components designed to facilitate the study of airflow dynamics and heat transfer processes. The stand

includes several selected devices that contribute to the overall functionality and experimental suitability. The stand allows aerodynamic, hydraulic, and thermal testing of heat exchangers under steady-state and transient conditions. The main component of the stand is a duct with a rectangular cross-section $B$ x $H$: 600 x 350 mm on the suction side of the fan and a circular cross-section $d_z$ = 315 mm on the discharge duct (Fig. 5.1 and Fig. 5.2).

Figure 5.2: Exprimental stand.

The stiffness of the ducts is maintained due to an appropriate wall thickness of 1 mm. The intake part (C) is located on the laboratory floor, set on a stable support structure. The exhaust section (D), on the other hand, is suspended from the ceiling, optimizing space utilization and allowing a continuous and unobstructed airflow path. The outlet duct is routed outside the room so that the temperature inside does not change during the experiment. All ducts are also thermally insulated. The air intake duct draws in air from the room, which has a large volume, and thanks to this a constant temperature of the intake air is ensured (Fig. 5.2).

The central element of the test stand is the placement of the heat exchanger (A) at the beginning of the intake duct. This placement ensures that the air sucked in by the centrifugal fan (B) first passes through the heat exchanger, after a sufficiently long run-up section (Fig. 5.3).

The fan, a key component of this system, is driven by a three-phase motor rated at 2.2 kW. The primary operating parameter, the maximum airflow rate, is 4,500 $\frac{m^3}{h}$ (equivalent to 1.25 $\frac{m^3}{s}$). Such a value allows the exchanger to be tested at air speeds in front of the exchanger from 0.5 to almost 5 m/s. Importantly, the speed of the fan can be infinitely adjusted using a frequency converter (Fig. 5.4).

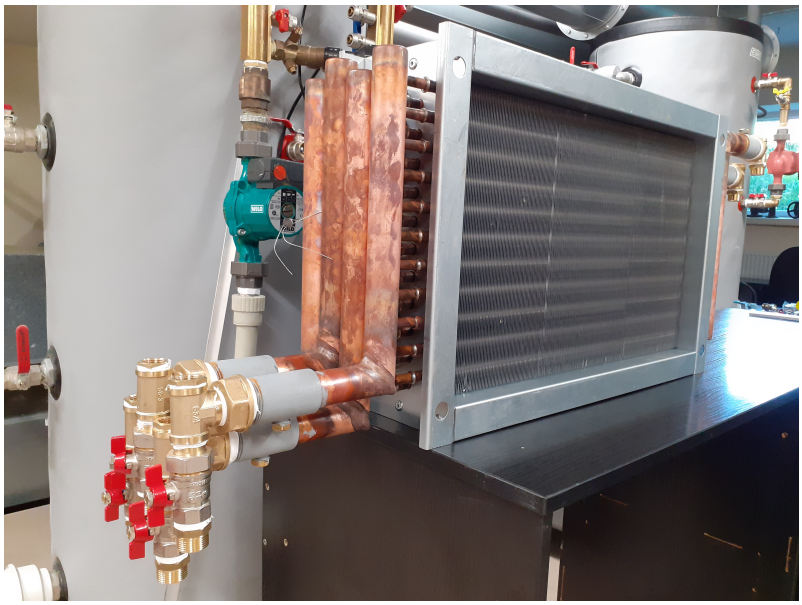

Figure 5.3: Tested heat exchanger.

Figure 5.4: Air fan.

An averaging measurement grid was mounted on the air outlet duct, suspended from the ceiling, to test the air velocity. The upper duct has a smaller flow area of 2.7 times that of the lower duct on which the heat exchanger is mounted, to be able to test the exchanger at speeds from 0.5 m/s (Fig. 5.5).

To verify the measurement of the differential pressure, and thus the airflow velocity, one of the commonly used methods was used - a Prandtl tube with a differential pressure measurement at the center of the converging nozzles. The measurement was made at the end of the air outlet channel, in a configuration with four converging nozzles. Each nozzle narrows the airflow, increasing its velocity after exiting the nozzle. This higher velocity

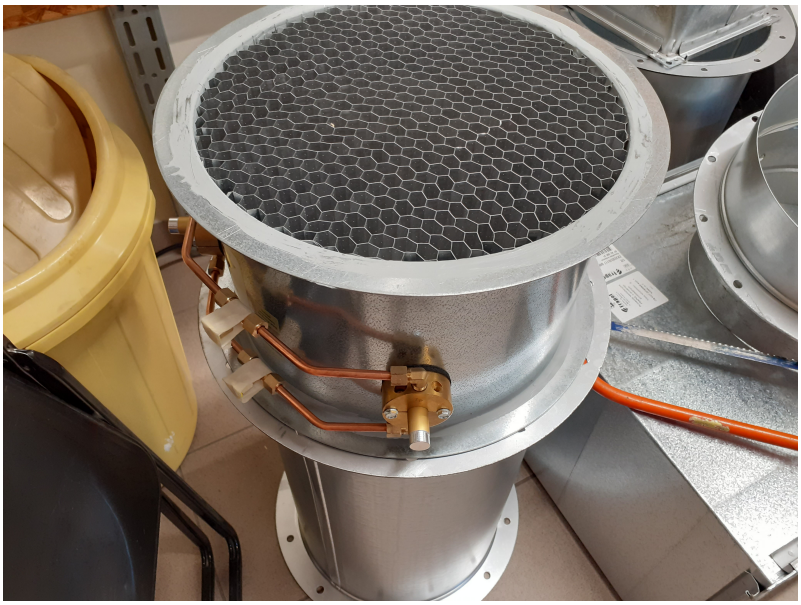

Figure 5.5: Averaging measurement grid.

flow area is critical for accurate measurements. The principle of the Prandtl tube is based on Bernoulli's equation, which relates the dynamic pressure of a fluid to its velocity. As air flows through the Prandtl tube, the converging jets cause the air velocity to increase, leading to a pressure drop. This pressure difference is used to calculate the local air velocity.

The data obtained from the Prandtl tube velocity measurements can then be compared with readings from an averaging grid, which also measures airflow velocity. By cross-validating the results from these two different measurement methods, the reliability and accuracy of the measurements can be ensured. This verification and validation process is essential in experimental setups to ensure the consistency and reliability of measurements.

The working medium flowing inside the exchanger tubes is water. The water is heated by a gas boiler with nominal power of 18 kW (1) and two electric heaters of 4.5 kW made (2) each placed in the second tank (3). The boiler is equipped with a circulation pump that provides water flow in the heat source (boiler) circuit.

During the tests under steady-state conditions, the temperature of the boiler feed water should be constant. For this purpose, two water storage tanks were installed, one to collect hot water from the boiler and the other to collect cooled water from the heat exchanger. The capacity of each tank is 400 liters. If the mass flux of water drawn from the storage tank is $\dot{V}_w = 0.5\ \frac{l}{s}$, the emptying time of the tanks is 26 min. This is a long enough chunk of time for the conducted tests to occur at the steady state (Fig. 5.6)

During the experiments, the hot feed water flows out of the tank (3) flows through the exchanger (5), which cools the water, and then it is pumped into the cold water tank (3). A circulating pump (6) is used to pump the water from tank one to tank two through the exchanger. The pump has a manual switch for 14-speed switching. Before the next

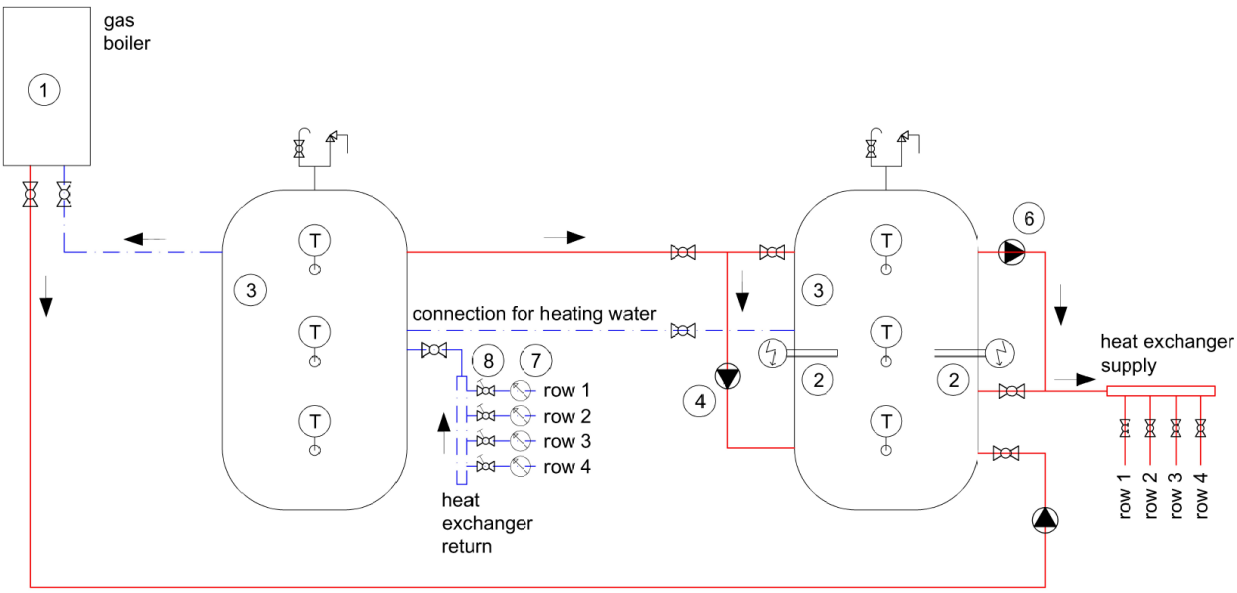


Figure 5.6: Diagram of the water flow; 1 - gas boiler, 2 - electric heater, 3 - supply and return water tank, 4 - mixing pump, 5 - circulating pump, 6 - turbine flow meters, 7 - control valves, T - water temperature sensors.

series of measurements, the water is heated to the target value in both tanks. In addition, a mixing pump is installed in tank two (4), which draws water from the top of the tank and dumps it into the bottom of the tank to unify the temperature.

The heat exchanger has a design with 4 rows and 11 runs. Water flows into 4 supply manifolds alternating left and right to average the temperature of the heating air behind every 2nd row. Then, from each of the 4 rows, it flows into a tube, where the water passes through the exchanger only once and flows into one of the four return manifolds. Graphically, the water flow is shown in Fig. 5.7. This diagram can be compared with the existing exchanger, which is pictured in Fig. 5.3.

## 5.2 Characteristics of the measurement system

Fig. 5.1 and Fig. 5.6 show a diagram of the test stand, consisting of an air duct with a hydraulic system. There are many temperature and pressure measuring points in the air supply and exhaust ducts. The list of used measuring instruments with their maximum uncertainty of measurement is presented in the table Tab. 5.1.

A differential pressure transducer FD 8612 DPS by Alhborn (Tab. 5.1) was used to measure the pressure difference on the averaging measurement grid (F) (Fig. 5.5). PT1000 temperature sensors were used to measure the water temperature at the inlet and outlet of each exchanger row. The thermocouples of the sensors are inserted into the hydraulic elbows at the beginning of the supply manifold of each row and at the end of the return manifold from each row of the exchanger (Fig. 5.8).

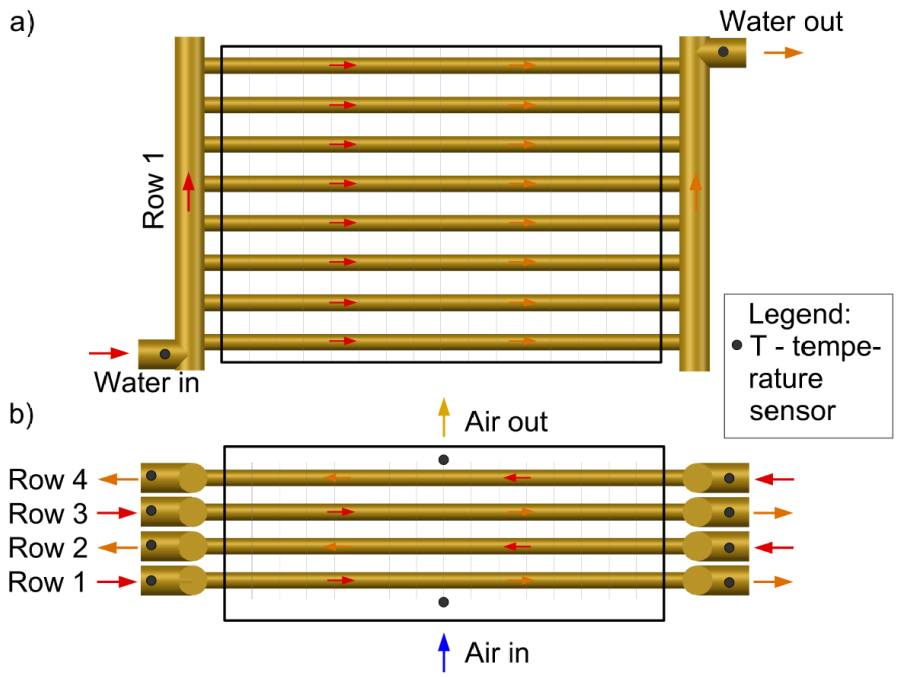


Figure 5.7: Diagram showing the flow of water in the heat exchanger under study: a) view of air inlet surface, b) top view showing the number of heat exchanger rows.

| Lp. | Name and type of measuring sensor | Measured quantity, measuring range | Maximum measurement uncertainty |
|---|---|---|---|
| 1 | Prandtl pipe FD A602-S1K | Air velocity, 0.5 ÷ 40 m/s | ± 0.5 % the upper limit of the measuring range |
| 2 | Turbine anemometer | Air velocity, 0.2 ÷ 20 m/s | ± 0.5 % the upper limit of the measuring range, ± 1.5 measured value |
| 3 | Differential pressure transducer FD 8612 DPS (air, Prandtl tube) | Pressure difference, 0 ÷ 50 Pa | ± 0.5 % the upper limit of the measuring range |
| 4 | Differential pressure transmitter FD 8612 DPS (air, measurement grid) | Pressure difference, 0 ÷ 50 Pa | ± 0.5 % the upper limit of the measuring range |
| 5 | PT1000 air temperature sensor | Air temperature, -50 $°C$ ÷ +180 $°C$ | ± 0.15 $°C$ for 0 $°C$ and ± 0.35 $°C$ for 100 $°C$ |
| 6 | PT1000 water temperature sensor | Water temperature, -50 $°C$ ÷ +180 $°C$ | ± 0.15 $°C$ for 0 $°C$ and ± 0.35 $°C$ for 100 $°C$ |
| 7 | Turbine turbine flow meter FVA915VTHM | Water volume flow, 2 ÷ 40 l/min | ± 0.5 % the upper limit of the measuring range |
| 8 | Data acquisition system ALMEMO 5690-2 | Up to 36 measuring points | |

Table 5.1: Specifications of the measuring instruments used.

The volume flow of water is measured using a turbine flow meter type FVA915VTHM by Alhborn, with a measuring range from 2.0 to 40.0 $\frac{l}{min}$, mounted on the water return

Figure 5.8: PT1000 temperature sensors mounted in heat exchanger's manifolds.

from each row of the exchanger to the chilled water tank. PT1000 temperature sensors were used to measure the air temperature before and after the exchanger. The sensor that measures the temperature of the air entering the duct is mounted in front of the exchanger. Two sensors measuring the temperature of the air behind the exchanger are placed behind the fan after the air is mixed in it.

# 6 Conduct experimental tests at different air velocities in front of the heat exchanger

Experimental studies included flow and heat measurements of air and water. Extensive steady-state tests were carried out at different air velocities with a single value of water flux. The values of the heat flux transferred from the water-side to the air-side were compared to control the correctness of the measurements. Based on the tests, correlations were determined for the heat transfer coefficients on the air-side, knowing the correlations for the heat transfer coefficient on the water-side. The experimentally determined correlations for the air-side heat transfer coefficient were compared with the correlations determined by CFD simulations.

## 6.1 The description of average air speed measurement

The air velocity was measured using the STRA from Test-therm (Fig. 5.5). It additionally has an inserted air straightener made of aluminum. The entire is mounted in the ventilation duct by screwing the flanges of the duct and the truss. The trusses are connected with hoses from two measuring nipples of total and static pressure and from the differential pressure transducer on the other side. Two averaging measuring tubes are placed in the lattice of the housing. The principle of operation is similar to other damming devices such as orifices, nozzles, or Prandtl tubes. In addition, the air velocity measurement was verified by an alternative Prandtl tube measurement at the outlet of the duct. A flap with four converging nozzles was built at the outlet of the duct.

The measurement procedure for the average air velocity can be done directly using a measuring grid with averaging probes. The total pressure is measured in several holes evenly spaced on the front surfaces of two probes crossed at right angles. On each of the two side surfaces of each probe on either side are additional holes measuring static pressure. By averaging the total pressure and the average pressure in the cross-section of the channel based on the measured pressure difference $\Delta p$, it is possible to determine the average velocity of the fluid flow. An averaging Prandtl tube used to measure the average air velocity in channels was used for the verification measurement. The dynamic pressure value measured with averaging tubes usually does not exceed 50 mm H2O (about 500 Pa).

## 6.2 Description of water temperature measurement for each row separately

The heat exchanger has a supply manifold and a return manifold (Fig. 5.8). Each collector feeds one row of tubes in the exchanger. One row has 11 tubes. Water flows through each tube in each row only once. It is an 11-run heat exchanger. Each row has a temperature sensor at the collector's supply and at the collector's outlet, due to which it is possible to determine the water cooling, and thus determine the heat flux from the water-side for each row independently. A shut-off valve is installed on the inlet of the tube line that carries water from the hot water tank to the respective rows. On the return line from each row to the tank, a turbine flow meter is installed to measure the volume flow of water, and a regulating valve is installed to set the same water flow through each row. Temperature sensors and flow meters are connected to a data acquisition system that collects all data during the experiment.

## 6.3 Description of air temperature determination for each row separately

Finned tubular heat exchangers have a complicated structure, and it is not possible to experimentally directly measure the average air temperature for each row. This work shows an indirect methodology where the heat fluxes transferred from water to air on a particular row are known. The air temperatures are calculated assuming that the heat flux on each row given up by the water is entirely transferred to the heat flux absorbed by the air. The heat flux transferred by water is given by the formula:

$$\dot{Q}_w = \dot{m}_w c_w (T_{w,in} - T_{w,out}) \tag{6.1}$$

where $Q_w$ is the heat flux on the water-side, $\dot{m}_w$ is the mass flow of water, $c_w$ is the average specific heat of the water, $T_{w,in}$ is the supply water temperature of a particular row, and $T_{w,out}$ mean the return water temperature from a particular row. The heat flux received by the air is:

$$\dot{Q}_a = \dot{m}_a c_{p,a} (T_{a,out} - T_{a,in}) \tag{6.2}$$

where $Q_a$ is the heat flux on the air-side, $\dot{m}_a$ is the mass flow of air, $c_{p,a}$ is the average specific heat of the air, $T_{w,in}$ is the air temperature in front of each row and $T_{w,out}$ denotes the air temperature behind a particular row.

Assuming that the heat flux from the water-side equals the water flux from the air-side $Q_w = Q_a$, equation Eq. 6.2 can be converted to the form:

$$T_{a,out}^{calc} = \frac{Q_w + \dot{m}_a c_{p,a} T_{a,in}}{\dot{m}_a c_{p,a}} \tag{6.3}$$

Using this formula, you can determine the average temperatures for each row. In order to check the correctness of measurements and calculations, the calculated temperature after the last row ($T_{a,out}^{calc}$) can be compared to the measured air temperature ($T_{a,out}^{exp}$) using a temperature sensor behind the exchanger.

## 6.4 Comparison of the exchanged heat flux determined from the air and water sides

Experimental tests were conducted with the electric heaters turned on and the exchanger supplied with hot water. Temperature and volume flux measurements were carried out on the water and air-sides. During the measurements, the speed of the airflow was changed by varying the speed of the fan pumping the air. The results of steady-state measurements are shown in Tab. 6.1.

During the measurements, the requirement presented by the ASHRAE standard [129] was met, according to which $\frac{\dot{Q}_w - \dot{Q}_{avg}}{\dot{Q}_{avg}}$ should be less than or equal to 5 % (Eq. 6.7), where

| $j$ [$-$] | $w_0$ [$m/s$] | $T_{a,in}$ [$°C$] | $T_{a,out}$ [$°C$] | $\dot{V}_w$ [$l/min$] | $T_{w,in}$ [$°C$] | $T_{w,out}$ [$°C$] | $Re_a$ [$-$] | $Re_w$ [$-$] |
|---|---|---|---|---|---|---|---|---|
| 1 | 0.47 | 24.22 | 52.54 | 31.35 | 63.63 | 61.14 | 260.9 | 3212.8 |
| 2 | 1.11 | 23.50 | 46.70 | 31.88 | 60.26 | 57.06 | 626.2 | 3099.4 |
| 3 | 1.45 | 23.59 | 48.41 | 32.72 | 65.80 | 61.65 | 817.2 | 3415.5 |
| 4 | 2.06 | 23.25 | 43.60 | 30.99 | 63.57 | 58.57 | 1170.4 | 3117.6 |
| 5 | 2.55 | 23.92 | 42.72 | 31.21 | 64.31 | 58.85 | 1446.4 | 3162.4 |
| 6 | 3.13 | 22.67 | 41.48 | 31.70 | 66.82 | 60.19 | 1794.0 | 3297.2 |
| 7 | 4.07 | 22.72 | 37.18 | 31.49 | 61.95 | 55.40 | 2344.7 | 3061.2 |
| 8 | 4.91 | 23.04 | 35.10 | 31.21 | 59.63 | 53.05 | 2809.9 | 2934.1 |

Table 6.1: Measurement results for the measurement series.

$\dot{Q}_w$ denotes the heat flux given off by water, while $\dot{Q}_{avg}$ is calculated as the arithmetic mean of $\dot{Q}_w$ and the heat flux taken over by air $\dot{Q}_a$. The heat fluxes $\dot{Q}_w$ and $\dot{Q}_a$ are defined by the formulas:

$$\dot{Q}_w = \dot{V}_w \rho_w(T_{w,in}) c_w|_{T_{w,out}}^{T_{w,in}} (T_{w,in} - T_{w,out}) \tag{6.4}$$

$$\dot{Q}_a = \dot{V}_a \rho_a(T_{a,in}) c_{p,a}|_{T_{a,out}}^{T_{a,in}} (T_{a,out} - T_{a,in}) \tag{6.5}$$

Air volume flux $\dot{V}_a$ is calculated from the formula:

$$\dot{V}_a = \frac{\pi d_{in}^2}{4} w_{avg} = HBw_0 \tag{6.6}$$

where $w_{avg}$ denotes the average airflow velocity in a circular duct and $w_0$ denotes the average airflow velocity before the exchanger in a rectangular duct, $H$ is the height of the heat exchanger and $B$ is the width of the heat exchanger.

The average temperature of the air behind the exchanger $T_{a,out}$ was measured behind the fan, where the mixed air has a homogeneous temperature. This measurement was made with two sensors at two different locations in the cross-section of the duct behind the fan. The correctness of the obtained experimental results was evaluated by calculating the relative difference $\epsilon_Q$ from the formula:

$$\epsilon_Q = \frac{\dot{Q}_w - \dot{Q}_{avg}}{\dot{Q}_{avg}} 100\% \tag{6.7}$$

where

$$\dot{Q}_{avg} = \frac{\dot{Q}_w + \dot{Q}_a}{2} \tag{6.8}$$

| $j$ [−] | $T_{a,out}^{exp}$ [°$C$] | $T_{a,out}^{calc}$ [°$C$] | $\dot{Q}_w$ [$W$] | $\dot{Q}_a$ [$W$] | $\dot{Q}_{avg}$ [$W$] | $\epsilon_Q$ [%] |
|---|---|---|---|---|---|---|
| 1 | 52.54 | 70.26 | 5310.5 | 5024.0 | 5167.3 | 2.77 |
| 2 | 46.70 | 47.86 | 6950.0 | 6450.9 | 6700.4 | 3.72 |
| 3 | 48.41 | 48.44 | 9262.3 | 8581.6 | 8921.9 | 3.82 |
| 4 | 43.60 | 42.53 | 10542.6 | 10093.4 | 10318.0 | 2.18 |
| 5 | 42.72 | 41.08 | 11615.9 | 11531.9 | 11573.9 | 0.36 |
| 6 | 41.48 | 39.64 | 14288.8 | 14260.1 | 14274.5 | 0.10 |
| 7 | 37.18 | 35.12 | 14085.0 | 14377.8 | 14231.4 | -1.03 |
| 8 | 35.10 | 33.23 | 14033.2 | 14508.3 | 14270.7 | -1.66 |

Table 6.2: Comparison of the average air temperature $T_{a,out}^{exp}$ determined from measurements with the temperature $T_{a,out}^{calc}$ determined from Eq. 6.8 and the relative difference $\epsilon_Q$ between the heat flux confessed from the water-side $\dot{Q}_w$ and the average flux $\dot{Q}_{avg}$.

The quality of the obtained measurement results can also be evaluated by determining the air temperature $T_{a,out}$ at the outlet of the exchanger from the energy balance:

$$\dot{Q}_w = \dot{Q}_a \tag{6.9}$$

The heat fluxes $\dot{Q}_w$ and $\dot{Q}_a$ are defined by the formulas Eq. 6.4 and Eq. 6.5. After substituting the formulas Eq. 6.4 and Eq. 6.5 into Eq. 6.9, the form is obtained:

$$T_{a,out} = \frac{Q_w + \dot{m}_a c_{p,a} T_{a,in}}{\dot{m}_a c_{p,a}} \tag{6.10}$$

Tab. 6.2 compares $T_{a,out}^{exp}$ values obtained from measurements with $T_{a,out}^{calc}$ values calculated from Eq. 6.10. The results shown in Tab. 6.2, it can be seen that the agreement of the values of heat fluxes confessed from the water and air-sides is very good, and the absolute values of $\epsilon_Q$ are less than the permissible value of 5 %.

## 6.5 Uncertainties of measurements and calculation results in experimental studies according to AMSE

Uncertainties of measurements and results of the experimental data were calculated using the ASME Measurement Uncertainty methodology [129]. Experimental results should include the following information:

- The precision limit $P$ relative to the nominal result (single or averaged) is the 95 % confidence interval within which the averages of multiple measurements should fall if the experiment is repeated multiple times under the same conditions using the

same equipment. Thus, the precision limit is an estimate of the lack of reproducibility caused by random errors and parameter transience during the experiment.

- The bias limit $B_l$. This is an estimate of the constant systematic error. This assumes that the person performing the experiment will pretend 95 % that the true value of the systematic error if known, should be less than $|B_l|$.

- Uncertainty $U$, the interval $\pm U$ relative to the nominal result, is the band in which the true results lie with 95 % confidence. The uncertainty of the result, with an assumed 95 % confidence interval, is calculated from the formula:

$$U = \sqrt{{B_l}^2 + P^2} \tag{6.11}$$

- Analyze the uncertainty according to the brief description above or according to the given literature. Estimation of precision and bias limits should be carried out at a representative time for the experiment. The uncertainty assessment should include additional information, which is best presented in tabular form. These include:

  - The precision and bias limits for each variable and parameters used in the study.
  - The equation used to develop the results (indirect measurement).
  - A presentation of the results including a comparison of the scatter of the results of the experiment conducted repeatedly with the expected scatter ($\pm P$) determined from the analysis of measurement uncertainty.

The discussion of the sources of experimental error without the evaluation of uncertainty presented above does not satisfy the AMSE requirements. All results presented must include an evaluation of uncertainty. All drawings presenting new experimental data should show an evaluation of the uncertainty of these data, either in the figure or in the figure description.

For the case of the analyzed heat exchanger, the heat flux $\dot{Q}$ received by the air is calculated from the formula:

$$\dot{Q} = \dot{m}_a c_{p,a}(T_{a,out} - T_{a,in}) \tag{6.12}$$

where $\dot{m}_a$ denotes the mass flow of air, $T_{a,out}$ and $T_{a,in}$ the inlet and outlet temperatures of air from the exchanger, respectively, and $c_{p,a}$ the specific heat of air at constant pressure.

The measurement uncertainty $U_{\dot{Q}}$ of the calculated value $U_{\dot{Q}}$ at the assumed 95 % confidence level is due to the random uncertainty $P_{\dot{Q}}$ and the systematic error $B_{\dot{Q}}$:

$$U_{\dot{Q}} = \sqrt{P_{\dot{Q}}^2 + B_{\dot{Q}}^2} \tag{6.13}$$

These two uncertainty components $U_{\dot{Q}}$ can be calculated separately as a function of the sensitivity coefficients of the calculated value of $\dot{Q}$ with respect to the measured quantities (i.e., $\frac{\partial \dot{Q}}{\partial \dot{m}_a}$) according to the law of error propagation [130][131]:

$$P_{\dot{Q}}^2 = (\frac{\partial \dot{Q}}{\partial \dot{m}_a})^2 P_{\dot{m}_a}^2 + (\frac{\partial \dot{Q}}{\partial \dot{c}_a})^2 P_{\dot{c}_a}^2 + (\frac{\partial \dot{Q}}{\partial \dot{T}_{a,out}})^2 P_{\dot{T}_{a,out}}^2 + (\frac{\partial \dot{Q}}{\partial \dot{T}_{a,in}})^2 P_{\dot{T}_{a,in}}^2 \tag{6.14}$$

and

$$B_{\dot{Q}}^2 = (\frac{\partial \dot{Q}}{\partial \dot{m}_a})^2 B_{\dot{m}_a}^2 + (\frac{\partial \dot{Q}}{\partial \dot{c}_a})^2 B_{\dot{c}_a}^2 + (\frac{\partial \dot{Q}}{\partial \dot{T}_{a,out}})^2 B_{\dot{T}_{a,out}}^2 + (\frac{\partial \dot{Q}}{\partial \dot{T}_{a,in}})^2 B_{\dot{T}_{a,in}}^2 \tag{6.15}$$

$$+2(\frac{\partial \dot{Q}}{\partial \dot{T}_{a,out}})(\frac{\partial \dot{Q}}{\partial \dot{T}_{a,in}}) B'_{T_{a,out}} B'_{T_{a,in}} \tag{6.16}$$

where $B'_{T_{a,out}}$ and $B'_{T_{a,in}}$ are the parts of $B_{T_{a,out}}$ and $B_{T_{a,in}}$ that are caused by identical sources of error (such as calibration error of thermocouples that were calibrated using the same standards, equipment and procedures) and therefore, are assumed to be perfectly correlated. Using the equation Eq. 6.12 to determine the derivatives and denoting $\Delta T = T_{a,out} - T_{a,in}$ is obtained after transformations:

$$\frac{P_{\dot{Q}}}{\dot{Q}} = (\frac{P_{\dot{m}_a}}{\dot{m}_a})^2 + (\frac{P_{c_{p,a}}}{c_{p,a}})^2 + (\frac{P_{T_{a,out}}}{\Delta T})^2 + (\frac{P_{T_{a,in}}}{\Delta T})^2 \tag{6.17}$$

and:

$$\frac{B_{\dot{Q}}}{\dot{Q}} = (\frac{B_{\dot{m}_a}}{\dot{m}_a})^2 + (\frac{B_{c_{p,a}}}{c_{p,a}})^2 + (\frac{B_{T_{a,out}}}{\Delta T})^2 + (\frac{B_{T_{a,in}}}{\Delta T})^2 - 2(\frac{B'_{T_{a,out}}}{\Delta T})(\frac{B'_{T_{a,out}}}{\Delta T}) \tag{6.18}$$

The derivatives in formulas Eq. 6.13 and Eq. 6.14 and Eq. 6.16 can be computed analytically, numerically, or with the aid of a data development program. The set of observations (measurements) of $\dot{m}$, $T_{a,out}$ and $T_{a,in}$, respectively, collected using appropriate meters in typical operating conditions, can be considered to have precision (accuracy) limitations of $P_{\dot{m}_a}$, $P_{T_{a,out}}$ and $P_{T_{a,im}}$ equal to two times the standard deviations of the set. The expressions must additionally account for the process's unpredictability (randomness); relying solely on the measuring instrument's error is insufficient. For the biggest unsteadiness period, a significant number of samples ($\geq 30$) should be taken during a long enough sampling time in order for the unsteadiness characteristics to be representative of the process.

Changes in the mean temperature in situations where the heat value is calculated using tables or the $c_{p,a}(T)$ function obtained using the least squares method may have an impact on the specific heat determination precision (accuracy) limit. If the dependence of $c_{p,a}$ on $T$ is defined, the $c_{p,a}$ value can be obtained. In contrast to the other factors in Eq. 6.14, this term is typically unnecessary when calculating the precision (accuracy) limit $P_{\dot{Q}}$. The estimation of partial systematic errors in pertinent variables or calibration done before and

after the experiment is used to determine the limits of systematic errors $B_{\dot{m}}$, $B_{T_{a,out}}$, and $B_{T_{a,in}}$. These limits are derived as the sum of the squares of partial errors.

The calibration technique, estimated inaccuracies in calibration standards, and errors resulting from the imprecise approximation of calibration results are all examples of partial systematic errors. The ”organic” error, which represents the systematic error incorporated in the specific heat value read from tables, is one of the elements of the limit of systematic error $B_c$. The inaccuracy is a result of mistakes made in measuring these qualities and tabulating the findings. These shares are typically at least 0.25 $\div$ 0.5 $\%$ and frequently substantially higher [131]. The true variable must be determined before evaluating the precision (accuracy) and the systematic error limits. For instance, in Eq. 6.12, temperatures $T_{a,out}$ and $T_{a,in}$ represent, respectively, the fluid mean temperatures in the outlet and inlet cross-sections. The systematic error, which Moffat [131] called the concept systematic error, is equal to the difference between the point-measured temperatures To and Ti and the fluid mean temperatures corresponding to them in the outlet and inlet cross-sections, respectively, if the temperatures $T_{a,out}$ and $T_{a,in}$ in Eq. 6.12 are determined at specific locations.

To account for this discrepancy, the indicators should be corrected, and when calculating the systematic error, the correction residual uncertainty should be added to the systematic errors in calibration, consider the following scenario: the systematic error limitations are non-correlated and total 0.5 $K$, with a 0.5 $\%$ systematic error limit for specific heat. In the range of indications from 10 to 90 $\%$ of the overall range, the estimated systematic error in mass flow rate measurement totals 0.25 $\%$. A conversation with the manufacturer reveals that this is an assessment of a constant error (which cannot be lowered by averaging multiple measurements and is therefore a systematic error). Eq. 6.18 yields the following result for $\Delta T$ = 20 $K$:

$$\frac{B_{\dot{Q}}}{\dot{Q}} = \sqrt{(0.0025)^2 + (0.005)^2 + (\frac{0.5K}{20K})^2 + (\frac{0.5K}{20K})^2} = 0.036 = 3.6\% \tag{6.19}$$

It is evident that the systematic error of temperature measurement is dominant and has the largest impact on the total systematic error of 3.6 $\%$. If the random errors and the nonstationarity of the process were such that the accuracy limit $P_{\dot{Q}}$ calculated from Eq. 6.13 would be 2.7 $\%$, then the total uncertainty of determining $U_{\dot{Q}}$ denoted by $U_{\dot{Q}}$ would be:

$$\frac{U_{\dot{Q}}}{\dot{Q}} = \sqrt{(\frac{B_{\dot{Q}}}{\dot{Q}})^2 + (\frac{P_{\dot{Q}}}{\dot{Q}})^2} = \sqrt{(0.036)^2 + (0.027)^2} = 0.045 = 4.5\% \tag{6.20}$$

# 7 Experimental determination of air-side Nusselt number correlations of individual tube rows, assuming known correlations for the Nusselt number on the inner surfaces of the tube

Experimental determination of the air-side heat transfer coefficients depicts the most actual heat flow in a heat exchanger from hot water to cool air. The process uses constant temperatures in the free fluid flow stream (70 $°C$) and a constant heat transfer coefficient on the water-side [93]. The simulation considers equal thermal resistance between the base of the fin and the outer surface of the tube, and equal: $R_{tc}$ = 3.17E-05 $\frac{m^2K}{W}$ [107]. The ability to assume a constant temperature in the free stream is due to the small differences in the outlet temperatures of individual rows. Furthermore, the effect of these row-by-row temperature differences on the air-side heat transfer coefficient is negligible, since the Prandtl numbers that vary for air do not change much [114]. The water-side heat transfer coefficients are equal in each row of tubes and are determined from the correlation [90] proposed by Taler and Taler as follows:

$$Nu_w = 0.01253 Re_w^{0.8413} Pr_w^{0.6179} \left[1 + (\frac{d_i}{L_x})^{2/3}\right] \qquad 3000 \leq Re_w \leq 10^6 \quad 1 < Pr_w \leq 3 \tag{7.1}$$

$$Nu_w = 0.00881 Re_w^{0.8991} Pr_w^{0.3911} \left[1 + (\frac{d_i}{L_x})^{2/3}\right] \qquad 3000 \leq Re_w \leq 10^6 \quad 3 < Pr_w \leq 1000 \tag{7.2}$$

The temperature increment on each row is recorded in the following

$$\Delta T_a^i = T_a^{i+1} - T_a^i \tag{7.3}$$

The symbol $\Delta T_a^i$ means the difference in the obtained air temperature between two adjacent rows, $T_a^{i+1}$ denotes air temperature in the outlet of the $i$-th row and $T_a^i$ is the inlet air temperature in the $i$-th row. The air temperatures were calculated using Eq. 6.10. From another perspective, the temperatures in Eq. 7.3 could be determined by solving differential equations describing air temperature distribution considering boundary conditions in front of the heat exchanger.

$$\frac{dT_a(y)}{dy} = N_a^i[T_w - T_a^i(y)] \tag{7.4}$$

The symbol $N_a^i$ (Eq. (7.4)) means the number of heat exchange units on the air-side for a particular row of tubes.

$$N_a^i = \frac{U_o^i A_{eq}}{\dot{m}_a c_{p,a}} \tag{7.5}$$

In Eq. (7.4), the symbol $A_{eq}$ denotes the outer surface area of the bare tube without fins in one fin pitch. The symbol $\dot{m}_a$ means air mass flow per tube and $c_{p,a}$ air heat capacity. The overall heat transfer coefficient is shown below.

$$\frac{1}{U_o^i} = \frac{1}{\alpha_{eq}^i} + \frac{A_{eq}}{A_m}\frac{\delta_t}{\lambda_t} + \frac{A_{eq}}{A_{in}}\frac{1}{\alpha_w} \tag{7.6}$$

where $\alpha_{eq}^i$ the equivalent air-side heat transfer coefficient (HTC) considering the fins attached to the tube, $A_{in}$ the area of the inner surface of the tube, $A_m = \frac{A_{in}+A_{out}}{2}$ the average area of the inner and outer surface of the tube $\delta_t$ the thickness of the wall of the tube, $\lambda_t$ the thermal conductivity of the tube material, $\alpha_w$ the water-side heat transfer coefficient. The value of $U_o^i$ was determined using the mathematical model developed in chapter 4.2. The value of $U_o^i$ was chosen so that the water temperature at the outlet of the $i$-th order was equal to the temperature measured in the experiment.

The equivalent air-side HTC in Eq. 7.7 $\alpha_{eq}$ is calculated using the mean HTC value in the entire tube row.

$$\alpha_{eq}^i = \alpha_a^i[\frac{A_{bf}}{A_o} + \frac{A_f}{A_o}\eta_f(\alpha_a^i)] \tag{7.7}$$

where $A_{bf}$ area of the outer tube surface between the fins, $A_f$ surface area of the fins, $\eta_f(\alpha_a)$ fin efficiency.

The boundary conditions in Eq. (7.8) have the following form:

$$T_a^i\big|_{y=0} = T_a^0 \tag{7.8}$$

Solving Eq. (7.4) considering the boundary condition Eq. (7.8)

$$T_a^i(y) = T_w + (T_a^i - T_w)e^{-N_a^i y}, \qquad 0 \leq y \leq 1 \tag{7.9}$$

Substituting $y = 1$ into Eq. (7.9) obtained the outlet temperature for the $i$-th row of tubes.

$$T_a^{i+1} = T_a^i(y) = T_w + (T_a^i - T_w)e^{-N_a^i} \tag{7.10}$$

Considering the range of $(y)$ for the next $i$-th row of tubes, obtained ojutlet temperatures for the $i$-th row of tubes.

$$Row\ 1 \qquad T_{a,I} = T_w + (T_a^0 - T_w)e^{-N_{a,I}} \tag{7.11}$$

$$Row\ 2 \qquad T_{a,II} = T_w + (T_{a,I} - T_w)e^{-(N_{a,I}+N_{a,II})} \tag{7.12}$$

$$Row\ 3 \qquad T_{a,III} = T_w + (T_{a,II} - T_w)e^{-(N_{a,I}+N_{a,II}+N_{a,III})} \tag{7.13}$$

| $j$ | $w_0$, $m/s$ | $\Delta T_{a,I}$, $°C$ | $\Delta T_{a,II}$, $°C$ | $\Delta T_{a,III}$, $°C$ | $\Delta T_{a,IV}$, $°C$ | $\Delta T_{t,i}$, $°C$ |
|---|---|---|---|---|---|---|
| 1 | 0.47 | 16.20 | 8.75 | 5.70 | 3.68 | 34.44 |
| 2 | 1.11 | 8.10 | 6.24 | 4.60 | 3.81 | 22.76 |
| 3 | 1.45 | 8.25 | 6.62 | 5.14 | 4.39 | 24.42 |
| 4 | 2.06 | 6.04 | 5.16 | 4.25 | 3.80 | 19.09 |
| 5 | 2.55 | 5.21 | 4.58 | 3.88 | 3.50 | 17.16 |
| 6 | 3.13 | 4.95 | 4.51 | 3.92 | 3.62 | 17.01 |
| 7 | 4.07 | 3.46 | 3.27 | 2.94 | 2.73 | 12.40 |
| 8 | 4.91 | 2.74 | 2.64 | 2.41 | 2.26 | 10.05 |

Table 7.1: Air temperatures behind each row obtained from experimental tests.

| $j$ | $w_0$ $\frac{m}{s}$ | $\alpha_{a,avg}$ $\frac{W}{m^2K}$ | $\alpha_{a,I}$ $\frac{W}{m^2K}$ | $\alpha_{a,II}$ $\frac{W}{m^2K}$ | $\alpha_{a,III}$ $\frac{W}{m^2K}$ | $\alpha_{a,IV}$ $\frac{W}{m^2K}$ | $Nu_{a,avg}$ | $Nu_{a,I}$ | $Nu_{a,II}$ | $Nu_{a,III}$ | $Nu_{a,IV}$ |
|---|---|---|---|---|---|---|---|---|---|---|---|
| 1 | 0.47 | 29.90 | 29.00 | 25.35 | 24.20 | 30.00 | 5.80 | 5.77 | 4.89 | 4.58 | 5.60 |
| 2 | 1.11 | 34.03 | 35.60 | 34.90 | 28.20 | 32.00 | 6.72 | 7.17 | 6.88 | 5.48 | 6.15 |
| 3 | 1.45 | 40.67 | 40.90 | 39.60 | 35.90 | 40.00 | 8.02 | 8.23 | 7.80 | 6.97 | 7.67 |
| 4 | 2.06 | 46.00 | 46.80 | 46.00 | 42.00 | 46.50 | 9.14 | 9.46 | 9.15 | 8.25 | 9.05 |
| 5 | 2.55 | 51.50 | 51.20 | 51.00 | 47.00 | 50.50 | 10.24 | 10.35 | 10.16 | 9.26 | 9.86 |
| 6 | 3.13 | 55.60 | 53.10 | 54.80 | 51.50 | 56.50 | 11.11 | 10.78 | 10.98 | 10.21 | 11.10 |
| 7 | 4.07 | 65.00 | 61.00 | 65.30 | 61.50 | 64.70 | 13.06 | 12.40 | 13.15 | 12.29 | 12.84 |
| 8 | 4.91 | 70.00 | 65.00 | 70.80 | 67.00 | 70.00 | 13.98 | 13.27 | 14.27 | 13.28 | 13.75 |

Table 7.2: Heat transfer coefficient $\alpha_a$ and Nusselt number $Nu$ for different air velocities for experiment.

$$Row\ 4 \qquad T_{a,IV} = T_w + (T_{a,IV} - T_w)e^{-(N_{a,I}+N_{a,II}+N_{a,III}+N_{a,IV})} \tag{7.14}$$

The outlet temperature from the entire heat exchanger using the average air-side heat transfer coefficient.

$$T_a^{out} = T_w + (T_a^{in} - T_w)e^{-(4N_a^{avg})} \tag{7.15}$$

The symbol $T_a^0$ means air temperature in front of the heat exchanger, $T_a^i$ is the inlet air temperature of the $i$-th row and $T_a^{i+1}$ is the outlet air temperature of the $i$-th row e.g. $T_{a,I}$ for row 1., $T_{a,II}$ for row 2., etc. The symbol $T_w$ denotes the temperature of the water and $N_a^i$ equals the number of heat exchange units for the $i$-th row of tubes e.g. $N_{a,I}$ for row 1., $N_{a,II}$ for row 2., etc. The symbol $N_a^{avg}$ means the average number of heat exchange units for the entire heat exchanger.

The resulting nonlinear equations from Eq. (7.11) to Eq. (7.15 with respect to air-side HTC ($\alpha_a$) can be solved by performing CFD simulations or by performing experiments.

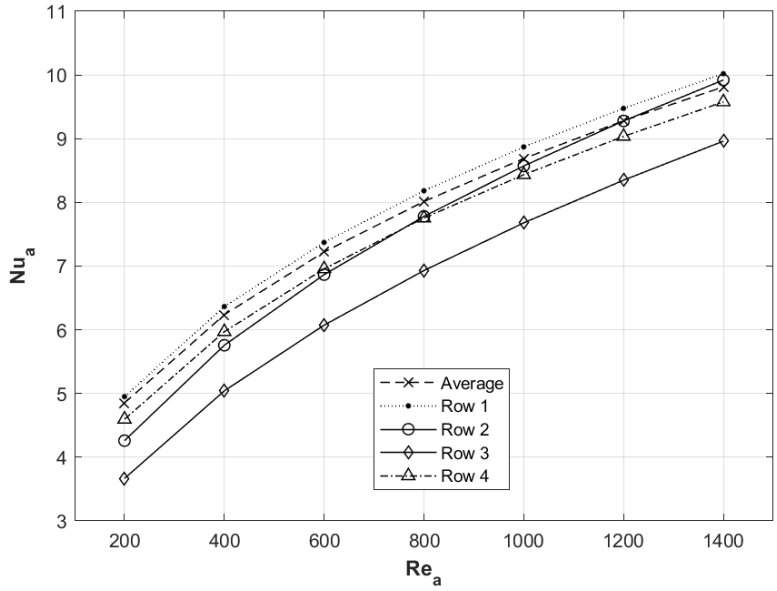


Figure 7.1: The impact of the PFTHE row number on the Nusselt number for experiments in the following Reynolds number ranges 200–1400.

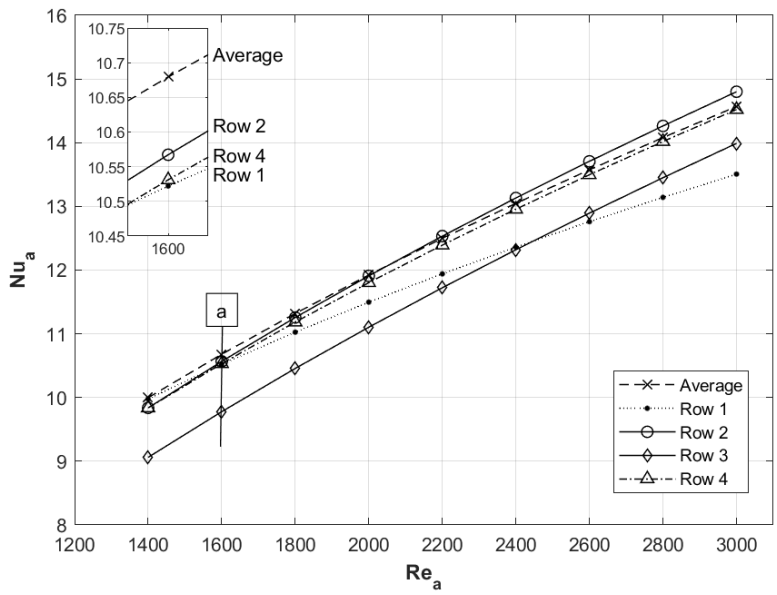


Figure 7.2: The impact of the PFTHE row number on the Nusselt number for experiments in the following Reynolds number ranges 1400–3000.

Necessarily is necessary to obtain the air temperature behind each row of tubes. Next, for $n$ different air velocities in front of the PFTHE $w_j^0, j = 1, ..., n$, $n$ air temperatures behind each row of tubes $T_a^{cfd,i}$ are obtained, and the HTC coefficient of the air-side $\alpha_{a,j}^i, j = 1, ..., n$ are obtained.

Knowing the determined values of $Nu_{a,i}$ for $j$ different air velocities $w_{0,j}$, the correlations on the Nusselt number from the air side with the following form $Nu_a = x_1 Re_a^{x_2} Pr_a^{1/3}$ were then determined. Parameters $x_1$ and $x_2$ of the experiment for the correlations deter-

| Reynolds number range | 200 $<Re_a<$1400 | | 1400 $<Re_a<$3000 | |
|---|---|---|---|---|
| Correlation's parameter | $x_1$ | $x_2$ | $x_1$ | $x_2$ |
| Average | 0.8033 | 0.3619 | 0.3143 | 0.494 |
| Row 1 | 0.8184 | 0.3622 | 0.6325 | 0.3972 |
| Row 2 | 0.4803 | 0.4344 | 0.2283 | 0.5359 |
| Row 3 | 0.3625 | 0.4592 | 0.1645 | 0.5698 |
| Row 4 | 0.7012 | 0.3773 | 0.2732 | 0.5111 |

Table 7.3: The PFTHE air-side Nusselt number correlation parameters for different Reynolds number ranges based on experimental data.

mined for the average Nusselt numbers for the entire heat exchanger and for the Nusselt number correlations of individual tube rows are presented in Tab. 7.3.

The values of the exponent $x_2$ for Reynolds numbers are within the range of 0.3619 - 0.4592 for Reynolds number value of 1400, which is consistent with the exponent values proposed by Taler et al. [132] for circular tubes. This could indicate that the airflow at such low Reynolds number values is characterized by laminar flow, compared to the Reynolds number exponents in its higher range from 1400 to 6000.

For larger Reynolds number values above 1400, the exponents are within the range of 0.3972 - 0.5698. However, the lower limit always occurs for the first row. This may imply that even at higher air velocities, the flow could be laminar or transitional in the first row, and turbulent in the subsequent rows, influenced by additional obstacles inside the heat exchanger in the form of exchange tubes.

# 8 Conclusions

This thesis addresses a range of topics concerning mathematical modeling, CFD simulations, and experimental studies of tubular finned cross-current heat exchangers. The equations of conservation of mass, momentum, and energy, which have been applied in mathematical modeling after simplification, are described in detail. At the beginning of the work, three different simulation methods carried out with Ansys Fluent 2020 R2 software are described. Correlations for the Nusselt number versus the Reynolds number were derived and compared with correlations available in the literature. All three methods were found to be very consistent with each other and with those available in the literature. Correlations $Nu_a = f(Re_a, Pr_a)$ contain two unknown parameters $x_1$ and $x_2$ which were determined based on CFD simulations.

The next part of the thesis presents the author's analytical derivations for a mathematical model of finned tubular heat exchangers. The model was programmed in the C++ programming language and verified experimentally. The results are very close to those

obtained by CFD simulations and experiments. At the end of the monography, the experiments conducted were described in detail. Starting with the description of the test facility, the experimental tests, and the experimental correlations for the Nusselt number were derived. The experimental correlations are very close to those derived from the CFD simulations were also presented. The efficiencies determined by the proposed procedure were compared with efficiencies calculated analytically.

Conclusions drawn from the entire work, with a particular focus on individual air-side Nusselt number correlations for different tube rows, are given below:

- Three different methods were developed to determine the mean Nusselt number in the particular tube row. In the first method, the temperature of the fin and the tube is constant. In the second method, only the temperature of the outer surface of the tube is constant, while the temperature of the fin depends on the position. In the third procedure, the temperature of the medium inside the tube and the heat transfer coefficient on the inner surface of the tube are assumed to be known.

- The developed numerical model accurately predicts the heat transfer behavior in the plate fin and tube heat exchanger, considering different air-side Nusselt number correlations for individual tube rows. This ensures a reliable representation of the heat transfer process.

- The experimental determination of air-side heat transfer coefficients for each tube row provides valuable data for validation, confirming the accuracy of the numerical model and simulation approach.

- Significant variations in air-side heat transfer coefficients for different tube rows were observed, emphasizing the importance of considering individual Nusselt number correlations for accurate predictions.

- The insights gained from this study have implications for the design and optimization of PFTHEs, enabling improved performance and efficiency.

- The findings are relevant for various industrial applications that rely on efficient heat transfer systems, such as ventilation, air conditioning, and refrigeration units.

Future research could explore more complex geometries and transient conditions to gain a deeper understanding of heat transfer phenomena in different applications and environments. Based on the calculations, simulations, and experimental studies, the following directions for extending existing research can be derived:

- Comprehensive investigation and testing of heat exchangers across the full spectrum of fluids flow within the exchanger.

- Refinement of methods for determining heat transfer coefficients through enhanced CFD simulation techniques.
- Expanded utilization of CFD simulations to curtail or minimize costs associated with experimental studies.
- Determination of correlations on individual tube rows for exchangers with multiple tube rows.
- Examination and modeling of exchangers under transient conditions.
- Application of the mathematical heat exchanger model to regulate outlet fluid temperatures, addressing the inverse problem for heat exchangers.

In summary, a combination of numerical and experimental analyses enhances insight into heat transfer within plate fin and tube heat exchangers. The validated numerical model, alongside empirical data, provides a solid basis for improving the design and operation of these heat exchangers across diverse applications. Incorporating Nusselt number correlations specific to individual tube rows enables precise prediction and optimization for distinct operational scenarios. The outcomes of this research contribute to the advancement of heat exchanger technology, leading to more sustainable and energy-efficient systems in the future.

# Nomenclature

## Abbreviations

BLS baseline

CFD Computational Fluid Dynamics

CHE Compact Heat Exchanger

DNS Direct Numerical Simulation

HEX Heat Exchanger

HTC Heat Transfer Coefficient

HVAC&R Heating, Ventilation, Air Conditioning and Refriegeration

PFTHE Plate Fin and Tube Heat Exchanger

SST Shear-Stress Transport

VDI Verein Deutscher Ingenieure, eng. Association of German Engineers

## Greek symbols

$\alpha_a$ air-side heat transfer coefficient, $W/m^2K$

$\alpha_{a,eq}$ equivalent air-side heat transfer coefficient, $W/m^2K$

$\delta_f$ fin thickness, $m$

$\delta_t$ tube thickness, $m$

$\eta_f$ fin efficiency, $-$

$\lambda_a$ air heat conduction, $W/mK$

$\lambda_t$ tube heat conduction, $W/mK$

$\nu_a$ air kinematic viscosity, $m^2/s$

$\rho_{a,0}$ air density in front of the heat exchanger, $kg/m^3$

$\rho_a$ air density, $kg/m^3$

$\rho_w$ water density, $kg/m^3$

$\sigma$ mean standard deviation, $-$

**Symbols**

$\Delta A$ heat transfer area in one control volume, $m^2$

$\Delta T_1$, $\Delta T_2$ temperature difference between air and heated wall, $K$

$\Delta T_a$ air temperature increment, $K$

$\Delta T_{m,a}$ logarihtmic mean air temperature, $K$

$\Delta x$ control volume thickness, width in $x$-direction, $m$

$\Delta y$ control volume length in $y$-direction = $p_l$, $m$

$\Delta z$ control volume height in $z$-direction = $p_t$, $m$

$\overline{c}_{p,a}$ average air specific heat at constant pressure, $J/kgK$

$\overline{c}_w$ average water specific heat, $J/kgK$

$\overline{T}$ average temperature of the fin surface, $°C$

$\overline{T}_a^i$, $\overline{T}_a^{i+1}$ average mass air temperature in front and behind particular row, $°C$

$\overline{T}_f$ average surface temperature of the fin, $°C$

$\overline{T}_{e,i}$ the average temperature of the fin surface for $i$-th finite element, $°C$

$\overline{T}_{tin,i}$ the average temperature of the tube's inner surface for $i$-th finite element, $°C$

$\overline{T}_{to,i}$ the average temperature of the tube's outer surface for $i$-th finite element, $°C$

$\overline{T}_{w,i}$ water average temperature in a control volume, $°C$

$\overline{w}_{a,i}$ average air velocity at the inlet of the $i$-th control area, $m/s$

$\overline{w}_{a,o}$ average air velocity in front of the heat exchanger, $m/s$

A total heat transfer area in single row, $m^2$

$A_b$ fin base surface area, $m^2$

$A_f$ area of the fin surface, $m^2$

$A_m$ average surface area of the tube $A_m = \frac{A_{in}+A_o}{2}$, $m^2$

$A_o$ outer tube surface area, $m^2$

$A_{bf}$ outer tube surface area in one fin pitch ($s$) between two fins, $m^2$

$A_{cv}$ cross sectional area of the control volume, $m^2$

$A_{eq}$ equivalent area, the outer surface of the bare tube in one fin pitch $s$ without fins, $m^2$

$A_{in}$ inner tube surface area, $m^2$

$A_i$ tube inner surface area, $m^2$

$A_{m,a}$ cross-section area of the modelled area, $m^2$

$A_{min}$ smallest cross-sectional area inside the heat exchanger, $m^2$

$A_o$ tube outer surface area, $m^2$

$A_t$ surface area of the equivalent bare tube, $m^2$

$B_l$ bias limit, $-$

C,$C_1$, $C_2$ constants of integration, $-$

$c_w$ water specific heat, $J/kgK$

$c_{p,a}$ air specific heat at constant pressure, $J/kgK$

$d_h$ equivalent hydraulic diameter, $m$

$d_i$ inner tube diameter, $m$

$d_o$ outer tube diameter, $m$

$d_{o,min}$ minimal outer tube diameter (in case of the elliptical tube), $m$

$e^{CFD}_{Q_{a,I}}$, $e^{CFD}_{Q_{a,II}}$, ... relative difference (error) of the total heat flow rate $Q_a$ in a particular row between the total heat flow rate obtained through CFD simulations and numerical calculations for the first row, second row, ..., n row, $-$

$e^{exp}_{Q_{a,I}}$, $e^{exp}_{Q_{a,II}}$, ... relative difference (error) of the total heat flow rate $Q_a$ in a particular row between the total heat flow rate obtained through experiment and numerical calculations for the first row, second row, ..., n row, $-$

$e_{Nu}$ relative difference (error) of the Nusselt number between Nusselt number with dedicated mesh elements and reference Nusselt number with mesh with a reference value of the elements, $-$

H height of the heat exchanger, $m$

i number of the row iteration, $-$

$i_a$, $h_a$ air enthalpy, $J/kg$

j number of the velocity iteration, $-$

$L_r$ fin length of the single row of the heat exchanger, $m$

$L_x$, $B$ width of the heat exchanger, $m$

$m_{a,i}$ air mass flow rate by one control volume, $kg/s$

$m_a$ air mass flow rate, $kg/s$

$m_{wr}$ mass flow rate of water per one row, $kg/s$

$m_{wt}$ mass flow rate of water per one tube, $kg/s$

$m_w$ water mass flow rate, $kg/s$

N number of the control volume in one row, $-$

$N_e$ number of the control volume, $-$

$n_r$ number of rows in the heat exchanger, $-$

$n_t$ number of tubes in one row, $-$

$N_{a,avg}$ average number of the air heat transfer unit of the entire heat exchanger, $-$

$N_{a,I}$, $N_{a,II}$, ... number of the air heat transfer unit (NTU) for a first row, second row, ..., n row, $-$

$N_{a,i}$ number of the air heat transfer unit (NTU) for a particular row, $-$

$N_a$ number of the air heat transfer unit (NTU), $-$

$N_{w,i}$ number of the water heat transfer unit (NTU) for a particular row, $-$

$N_w$ number of the water heat transfer unit (NTU), $-$

$Nu_{a,i}$ air-side Nusselt number of the particular row of the heat exchanger, $-$

$Nu_a$ air-side Nusselt number, $-$

$Nu_{ni}$ air-side Nusselt number with a given number of the mesh elements, $-$

$Nu_{ref}$ air-side Nusselt number for mesh with a reference value of the elements, $-$

$Nu_w$ water-side Nusselt number, $-$

P precision limit, $-$

$p_l$ longitudinal tube pitch, $m$

$P_o$ outer perimeter of the tube, $m$

$p_t$ transversal tube pitch, $m$

$Pr_a$ air-side Prandtl number, $-$

$Pr_w$ water-side Prandtl number, $-$

Q total heat flow rate transferred from wall to air, $W$

$Q_{a,I}$, $Q_{a,II}$, ... total heat flow rate transferred to air for the first row, second row, ..., n row, $W$

$Q_{a,i}$ total heat flow rate transferred from wall to air, $W$

$Q_{avg}$ arithmetic mean heat flow rate of the water- and air-side, $W$

$Q_a$ total heat flow rate on the air-side, $W$

$Q_{max}$ total maximum heat flow rate transferred from wall to air assuming constant fin temperature as the temperature of the fin base, $W$

$q_{o,i}$ mean heat flux on the length of the $i$-th control volume, $W/kg$

$Q_w$ total heat flow rate transferred from water, $W$

R number of row, $-$

$r_i$ inner tube radius, $m$

$r_o$ outer tube radius, $m$

$R_{\alpha,a}$ thermal heat transfer resistance from the outside surface of the tubes and fin, $m^2K/W$

$R_{\alpha,w}$ thermal heat transfer resistance from the inside surface of the tubes, $m^2K/W$

$R_{\lambda,ft}$ thermal heat transfer resistance from the outside surface of the tubes and fin, $m^2K/W$

$R_{\lambda,f}$ thermal heat conduction resistance of the fin, $mK/W$

$R_{tr}$ thermal resistance between fin base and the tube outer surface, $m^2K/W$

$Re_a$ air-side Reynolds number, $-$

$Re_{d_h,a}$ air-side Reynolds number based on the hydraulic diameter, $-$

$\mathrm{Re}_{d_o}$ air-side Reynolds number based on the outer tube diameter, $-$

$\mathrm{Re}_w$ water-side Reynolds number, $-$

s fin pitch, $m$

$\mathrm{T}_2^{calc}$, $T_2^{exp}$ calculated and obtained experimentally outlet air temperature behind particular row, $^\circ C$

$\mathrm{T}_a^{i+1}$, $T_a^{out}$, $T_2$, $T_{a,i}^{''}$ outlet mass average air temperature behind particular row in the heat exchanger, $^\circ C$

$\mathrm{T}_a^{i}$, $T_a^{in}$, $T_1$, $T_{a,i}^{'}$ inlet mass average air temperature in front of each row in heat exchange, $^\circ C$

$\mathrm{T}_a$ air temperature, $^\circ C$

$\mathrm{T}_b$ fin base temperature, $^\circ C$

$\mathrm{T}_{a,0}$ mass average air temperature in front of the heat exchanger, $^\circ C$

$\mathrm{T}_{a,I}, T_{a,II}, T_{a,III}, T_{a,IV}$ outlet mass average air temperature behind each row in heat exchange, $^\circ C$

$\mathrm{T}_{a,i}^{CFD}$ mass average air temperature behind a particular row of tubes based on the CFD simulation, $^\circ C$

$\mathrm{T}_{a,out}^{calc}$ outlet mass average air temperature behind the particular row in heat exchanger based on the calculation, $^\circ C$

$\mathrm{T}_{a,out}^{exp}$ outlet mass average air temperature behind the particular row in heat exchanger based on the CFD simulation, $^\circ C$

$\mathrm{T}_{amb}$ ambient temperature, $^\circ C$

$\mathrm{T}_{fl}$ free flow fluid temperature, $^\circ C$

$\mathrm{T}_{w,i+1}$, $T_w^{''}$, $T_{w,out}$ outlet water temperature of the control volume, $^\circ C$

$\mathrm{T}_{w,i}$, $T_w^{'}$, $T_{w,in}$ inlet water temperature of the control volume, $^\circ C$

$\mathrm{T}_{wall}$ fin and tubes wall temperature, $^\circ C$

$\mathrm{T}_w$ water temperature, $^\circ C$

U uncertainity, $-$

$\mathrm{U}_o$ overal heat transfer coefficient in dedicated row, $W/m^2K$

$U_{ca}$ perimeter of the cross-section in the control volume, $m$

$V_a$ overall volume of a row, $m^2$

$V_a$ volume air flow rate, $m^3/s$

$V_o$ volume through which air flow in a single row, $m^3$

$V_t$ volume of tubes in one row, $m^2$

$V_w$ volume water flow rate, $m^3/s$

$w_{a,max}$, $w_{max}$ maximum air velocity in the smallest cross sectional area $A_{min}$ inside heat exchanger, $m/s$

$w_{a,o}$ air velocity in front of the heat exchanger, $m/s$

$x_1, x_2$ parameters in the approximation function $Nu = x_1 Re^{x_2} Pr^{1/3}$, $-$

# References


1. Kays, W. M. & London, A. L. *Compact heat exchangers* Third Edition. ISBN: 0-07-033418-8 (Scientific International, India, 2018).
2. Alyaseen, N. O. M., Mehrzad, S. & Saffarian, M. R. An investigation of multi-stream plate-fin heat exchanger modelling and design: a review. *Kerntechnik* **88,** 457–474 (2023).
3. Thulukkanam, K. *Heat Exchanger Design Handbook* Second Edition. ISBN: 978-1-4398-4212-6 (CRC Press, Boca Raton, FL, USA, 2013).
4. Najafi, H., Najafi, B. & Hoseinpoori, P. Energy and cost optimization of a plate and fin heat exchanger using genetic algorithm. *Applied Thermal Engineering* **31,** 1839–1847 (2011).
5. McQuiston, F., Parker, J. & Spitler, J. *Heating, Ventilating, and Air Conditioning Analysis and Design* ISBN: 0-471-47015-5 (JohnWiley & Sons, Hoboken, NJ, 2005).
6. Stehlík, P. & Wadekar, V. V. Different Strategies to Improve Industrial Heat Exchange. *Heat Transfer Engineering* **23,** 36–48 (2002).
7. Piroozfam, N., Hosseinpour Shafaghi, A. & Razavi, S. E. Numerical investigation of three methods for improving heat transfer in counter-flow heat exchangers. *International Journal of Thermal Sciences* **133,** 230–239 (2018).
8. Sun, N. *et al.* An intelligent plate fin-and-tube heat exchanger design system through integration of CFD, NSGA-II, ANN and TOPSIS. *Expert Systems with Applications* **233,** 120926 (2023).
9. Bhuiyan, A. A. & Islam, A. K. M. S. Thermal and hydraulic performance of finned-tube heat exchangers under different flow ranges: A review on modeling and experiment. *International Journal of Heat and Mass Transfer* **101,** 38–59 (2016).
10. Aslam Bhutta, M. M. *et al.* CFD applications in various heat exchangers design: A review. *Applied Thermal Engineering* **32,** 1–12 (2012).
11. Taler, D. *Numerical Modelling and Experimental Testing of Heat Exchangers* ISBN: 978-3-319-91127-4 (Springer International Publishing, Cham, Switzerland, 2019).
12. Wen, M.-Y. & Ho, C.-Y. Heat-transfer enhancement in fin-and-tube heat exchanger with improved fin design. *Applied Thermal Engineering* **29,** 1050–1057 (2009).
13. Kudiiarov, V., Elman, R., Pushilina, N. & Kurdyumov, N. State of the Art in Development of Heat Exchanger Geometry Optimization and Different Storage Bed Designs of a Metal Hydride Reactor. *Materials* **16,** 4891 (2023).

14. Sadeghianjahromi, A. & Wang, C.-C. Heat transfer enhancement in fin-and-tube heat exchangers – A review on different mechanisms. *Renewable and Sustainable Energy Reviews* **137,** 110470 (2021).

15. Adam, A. Y. *et al.* State of the art on flow and heat transfer performance of compact fin-and-tube heat exchangers. *Journal of Thermal Analysis and Calorimetry* **139,** 2739–2768 (2020).

16. Korde, V. M., Gotmare, G. S., Kachhwah, P. K. & Lokhande, D. *Design and Performance of Plate-Fin Heat Exchanger: A Brief Review* in *Advances in Mechanical Engineering and Technology* (eds Singari, R. M., Kankar, P. K. & Moona, G.) (Springer Singapore, Singapore, 2022), 127–139.

17. Macchitella, S., Colangelo, G. & Starace, G. Performance Prediction of Plate-Finned Tube Heat Exchangers for Refrigeration: A Review on Modeling and Optimization Methods. *Energies* **16,** 1948 (2023).

18. Marcinkowski, M., Taler, D., Taler, J. & Weglarz, K. Air-Side Nusselt Numbers and Friction Factor's Individual Correlations of Finned Heat Exchangers. *Energies* **15,** 5630 (2022).

19. Lindqvist, K., Skaugen, G. & Meyer, O. H. H. Plate fin-and-tube heat exchanger computational fluid dynamics model. *Applied Thermal Engineering* **189,** 116669 (2021).

20. Hu, D. *et al.* Performance optimization of a wavy finned-tube heat exchanger with staggered curved vortex generators. *International Journal of Thermal Sciences* **183,** 107830 (2023).

21. Erdinc, M. T. Computational thermal-hydraulic analysis and geometric optimization of elliptic and circular wavy fin and tube heat exchangers. *International Communications in Heat and Mass Transfer* **140,** 106518 (2023).

22. Dodiya, K., Bhatt, N. & Lai, F. Louvered fin compact heat exchanger: a comprehensive review. *International Journal of Ambient Energy* **43,** 3545–3559 (2022).

23. Hsieh, C.-T. & Jang, J.-Y. Parametric study and optimization of louver finned-tube heat exchangers by Taguchi method. *Applied Thermal Engineering* **42,** 101–110 (2012).

24. Yun, R., Kim, Y. & Kim, Y. Air side heat transfer characteristics of plate finned tube heat exchangers with slit fin configuration under wet conditions. *Applied Thermal Engineering* **29,** 3014–3020 (2009).

25. Mohanta, L., Joardar, A., Esformes, J. L., Videto, B. & Sienel, T. H. Numerical Analysis of Fluid Flow and Heat Transfer in Wavy and Hybrid-Slit-Wavy Fin-and-Tube Heat Exchangers. *Science and Technology for the Built Environment* **25,** 767–775 (2019).

26. Arora, A. & Subbarao, P. M. V. Investigation of Performance Augmentation Due to Geometric Modification of Vortex Generators Placed in Fin-and-Tube Heat Exchangers. *Journal of Thermal Science and Engineering Applications* **15,** 1–13 (2023).

27. Sharma, R., Mishra, D. P., Sarangi, S. K. & Brar, L. S. Performance Evaluation of a Fin and Tube Heat Exchanger Based on Different Shapes of the Winglets. *Journal of Thermal Science and Engineering Applications* **15,** 1–10 (2023).

28. Chen, H.-T., Lin, Y.-S., Chen, P.-C. & Chang, J.-R. Numerical and experimental study of natural convection heat transfer characteristics for vertical plate fin and tube heat exchangers with various tube diameters. *International Journal of Heat and Mass Transfer* **100,** 320–331 (2016).

29. Zhu, H. *et al.* Thermal-Hydraulic Performance and Optimization of Tube Ellipticity in a Plate Fin-And-Tube Heat Exchanger. *Journal of Electronic Packaging* **141,** 1–8 (2019).

30. Zeeshan, M., Nath, S. & Bhanja, D. Numerical study to predict optimal configuration of fin and tube compact heat exchanger with various tube shapes and spatial arrangements. *Energy Conversion and Management* **148,** 737–752 (2017).

31. Kim, Y. & Kim, Y. Heat transfer characteristics of flat plate finned-tube heat exchangers with large fin pitch. *International Journal of Refrigeration* **28,** 851–858 (2005).

32. Saboya, F. E. M. & Sparrow, E. M. Local and Average Transfer Coefficients for One-Row Plate Fin and Tube Heat Exchanger Configurations. *Journal of Heat Transfer* **96,** 265–272 (1974).

33. Yaïci, W., Ghorab, M. & Entchev, E. 3D CFD study of the effect of inlet air flow maldistribution on plate-fin-tube heat exchanger design and thermal–hydraulic performance. *International Journal of Heat and Mass Transfer* **101,** 527–541 (2016).

34. He, Y. L., Tao, W. Q., Song, F. Q. & Zhang, W. Three-dimensional numerical study of heat transfer characteristics of plain plate fin-and-tube heat exchangers from view point of field synergy principle. *International Journal of Heat and Fluid Flow* **26,** 459–473 (2005).

35. Marcinkowski, M. & Taler, D. Calculating the Efficiency of Complex-Shaped Fins. *Energies* **14,** 577 (2021).

36. Jang, J.-Y., Wu, M.-C. & Chang, W.-J. Numerical and experimental studies of threedimensional plate-fin and tube heat exchangers. *International Journal of Heat and Mass Transfer* **39,** 3057–3066 (1996).

37. Pesteei, S. M., Subbarao, P. M. V. & Agarwal, R. S. Experimental study of the effect of winglet location on heat transfer enhancement and pressure drop in fin-tube heat exchangers. *Applied Thermal Engineering* **25,** 1684–1696 (2005).

38. Xie, G., Wang, Q. & Sunden, B. Parametric study and multiple correlations on air-side heat transfer and friction characteristics of fin-and-tube heat exchangers with large number of large-diameter tube rows. *Applied Thermal Engineering* **29,** 1–16 (2009).

39. Sadeghianjahromi, A., Kheradmand, S., Nemati, H. & Wang, C.-C. Optimization of the Louver Fin-and-tube Heat Exchangers – A Parametric Approach. *Journal of Enhanced Heat Transfer* **27,** 1–14 (2020).

40. Romero-Méndez, R., Sen, M., Yang, K. T. & McClain, R. Effect of fin spacing on convection in a plate fin and tube heat exchanger. *International Journal of Heat and Mass Transfer* **43,** 39–51 (2000).

41. Wang, C. C., Chi, K. Y. & Chang, C. J. Heat transfer and friction characteristics of plain fin-and-tube heat exchangers, part II: Correlation. *International Journal of Heat and Mass Transfer* **43,** 2693–2700 (2000).

42. Choi, J. M., Kim, Y., Lee, M. & Kim, Y. Air side heat transfer coefficients of discrete plate finned-tube heat exchangers with large fin pitch. *Applied Thermal Engineering* **30,** 174–180 (2010).

43. Zhan, F., Tang, J., Ding, G. & Zhuang, D. Experimental investigation on particle deposition characteristics of wavy fin-and-tube heat exchangers. *Applied Thermal Engineering* **99,** 1039–1047 (2016).

44. Lee, M., Kim, Y., Lee, H. & Kim, Y. Air-side heat transfer characteristics of flat plate finned-tube heat exchangers with large fin pitches under frosting conditions. *International Journal of Heat and Mass Transfer* **53,** 2655–2661 (2010).

45. Chen, H.-T., Chou, J.-C. & Wang, H.-C. Estimation of heat transfer coefficient on the vertical plate fin of finned-tube heat exchangers for various air speeds and fin spacings. *International Journal of Heat and Mass Transfer* **50,** 45–57 (2007).

46. Syuhada, A., Afandi, D. & Sofyan, S. E. Convective heat transfer study on the spiral finned tube heat exchanger under various fin pitch arrangements. *IOP Conference Series: Earth and Environmental Science* **463,** 012024 (2020).

47. Rainieri, S., Bozzoli, F. & Pagliarini, G. Wiener filtering technique applied to thermographic data reduction intended for the estimation of plate fins performance. *Experimental Thermal and Fluid Science* **28,** 179–183 (2004).

48. Bilirgen, H., Dunbar, S. & Levy, E. K. Numerical modeling of finned heat exchangers. *Applied Thermal Engineering* **61,** 278–288 (2013).

49. Gholami, A., Wahid, M. A. & Mohammed, H. A. Thermal–hydraulic performance of fin-and-oval tube compact heat exchangers with innovative design of corrugated fin patterns. *International Journal of Heat and Mass Transfer* **106,** 573–592 (2017).

50. Awais, M. & Bhuiyan, A. A. Heat and mass transfer for compact heat exchanger (CHXs) design: A state-of-the-art review. *International Journal of Heat and Mass Transfer* **127,** 359–380 (2018).

51. Li, L., Du, X., Zhang, Y., Yang, L. & Yang, Y. Numerical simulation on flow and heat transfer of fin-and-tube heat exchanger with longitudinal vortex generators. *International Journal of Thermal Sciences* **92,** 85–96 (2015).

52. He, Y.-L., Chu, P., Tao, W.-Q., Zhang, Y.-W. & Xie, T. Analysis of heat transfer and pressure drop for fin-and-tube heat exchangers with rectangular winglet-type vortex generators. *Applied Thermal Engineering* **61,** 770–783 (2013).

53. Pirompugd, W., Wongwises, S. & Wang, C.-C. Simultaneous heat and mass transfer characteristics for wavy fin-and-tube heat exchangers under dehumidifying conditions. *International Journal of Heat and Mass Transfer* **49,** 132–143 (2006).

54. Taler, D., Taler, J. & Trojan, M. Thermal calculations of plate–fin–and-tube heat exchangers with different heat transfer coefficients on each tube row. *Energy* **203,** 117806 (2020).

55. Marcinkowski, M., Taler, D., Taler, J. & Weglarz, K. Comparison of Individual Air-Side Row-By-Row Heat Transfer Coefficient Correlations on Four-Row Finned-Tube Heat Exchangers. *Heat Transfer Engineering* **44,** 1002–1014 (2023).

56. Caket, A. G., Wang, C., Nugroho, M. A., Celik, H. & Mobedi, M. Recent studies on 3D lattice metal frame technique for enhancement of heat transfer: Discovering trends and reasons. *Renewable and Sustainable Energy Reviews* **167,** 112697 (2022).

57. Bashtani, I., Esfahani, J. A. & Kim, K. C. Hybrid CFD-ANN approach for evaluation of bio-inspired dolphins dorsal fin turbulators of heat exchanger in turbulent flow. *Applied Thermal Engineering* **219,** 119422 (2023).

58. Zhang, Y. *et al.* A quantitative energy efficiency evaluation and grading of plate heat exchangers. *Energy* **142,** 228–233 (2018).

59. Pratama, A. & Irwansyah, R. Additive manufacturing-based heat exchanger: A review. *AIP Conference Proceedings* **2630,** 030008 (2023).

60. Muley, A. *et al. Recent Advances in Thin-Wall Additively Manufactured Heat Exchangers* in *IMECE2021* (Volume 2A: Advanced Manufacturing, 2021). (2023).

61. Niknam, S. A., Mortazavi, M. & Li, D. Additively manufactured heat exchangers: a review on opportunities and challenges. *The International Journal of Advanced Manufacturing Technology* **112,** 601–618 (2021).

62. Klein, E., Ling, J., Aute, V., Hwang, Y. & Radermacher, R. A Review of Recent Advances in Additively Manufactured Heat Exchangers. *International Refrigeration and Air Conditioning Conference* **2478,** 1–10 (2018).

63. Jadhav, P. H., Gnanasekaran, N., Perumal, D. A. & Mobedi, M. Performance evaluation of partially filled high porosity metal foam configurations in a pipe. *Applied Thermal Engineering* **194,** 117081 (2021).

64. Alam, T. & Kim, M.-H. A comprehensive review on single phase heat transfer enhancement techniques in heat exchanger applications. *Renewable and Sustainable Energy Reviews* **81,** 813–839 (2018).

65. Kaur, I. & Singh, P. State-of-the-art in heat exchanger additive manufacturing. *International Journal of Heat and Mass Transfer* **178,** 121600 (2021).

66. Hussain, A. R. J. *et al.* Review of polymers for heat exchanger applications: Factors concerning thermal conductivity. *Applied Thermal Engineering* **113,** 1118–1127 (2017).

67. Cevallos, J. G., Bergles, A. E., Bar-Cohen, A., Rodgers, P. & Gupta, S. K. Polymer Heat Exchangers—History, Opportunities, and Challenges. *Heat Transfer Engineering* **33,** 1075–1093 (2012).

68. Zaheed, L. & Jachuck, R. J. J. Review of polymer compact heat exchangers, with special emphasis on a polymer film unit. *Applied Thermal Engineering* **24,** 2323–2358 (2004).

69. Qian, M. *et al.* Study on heat dissipation performance of a lattice porous structures under jet impingement cooling. *Case Studies in Thermal Engineering* **49,** 103244 (2023).

70. Cormier, Y., Dupuis, P., Jodoin, B. & Corbeil, A. Net Shape Fins for Compact Heat Exchanger Produced by Cold Spray. *Journal of Thermal Spray Technology* **22,** 1210–1221 (2013).

71. Yadav, A. & Singh, Y. A review on microchannel heat exchanger and the effects of various parameters. *AIP Conference Proceedings* **2521,** 030016 (2023).

72. Zhang, J., Zou, Z. & Fu, C. A Review of the Complex Flow and Heat Transfer Characteristics in Microchannels. *Micromachines* **14,** 1451 (2023).

73. Mohammed, H. A., Bhaskaran, G., Shuaib, N. H. & Saidur, R. Heat transfer and fluid flow characteristics in microchannels heat exchanger using nanofluids: A review. *Renewable and Sustainable Energy Reviews* **15,** 1502–1512 (2011).

74. Luo, L., Fan, Y. & Tondeur, D. Heat exchanger: from micro- to multi-scale design optimization. *International Journal of Energy Research* **31,** 1266–1274 (2007).

75. Kambli, A. & Dey, P. A critical review on recent developments and applications of microchannels in the field of heat transfer and energy. *Heat and Mass Transfer* **59,** 1707–1747 (2023).

76. Gosai, S. S. & Joshi, V. C. A Review on Two Phase Flow in Micro channel Heat Exchangers. *International Journal of Applied Research & Studies* **2,** 1–9 (2015).

77. Bhosale, S. & Acharya, A. Review On Applications of Micro Channel Heat Exchanger. *International Research Journal of Engineering and Technology* **7,** 1–5 (2020).

78. Nguyen, D. H. & Ahn, H. S. A comprehensive review on micro/nanoscale surface modification techniques for heat transfer enhancement in heat exchanger. *International Journal of Heat and Mass Transfer* **178,** 121601 (2021).

79. Han, Y., Liu, Y., Li, M. & Huang, J. A review of development of micro-channel heat exchanger applied in air-conditioning system. *Energy Procedia* **14,** 148–153 (2012).

80. Jamuna Rani, G., Sai Rani, G. & Praveen, A. Nano fluids effect on crossflow heat exchanger characteristics – Review. *Materials Today: Proceedings* **44,** 527–531 (2021).

81. Ajeeb, W. & Murshed, S. M. S. *An Overview of Performance and Application of Nanofluids in Compact Heat Exchangers* in *5-6th Thermal and Fluids Engineering Conference (TFEC)* (2021), 1171–1180.

82. Pandya, N. S., Shah, H., Molana, M. & Tiwari, A. K. Heat transfer enhancement with nanofluids in plate heat exchangers: A comprehensive review. *European Journal of Mechanics - B/Fluids* **81,** 173–190 (2020).

83. Ajeeb, W. & Murshed, S. M. S. Nanofluids in compact heat exchangers for thermal applications: A State-of-the-art review. *Thermal Science and Engineering Progress* **30,** 101276 (2022).

84. Patel, T. A., Kumar, A. & Patel, V. K. Efficiency and cost optimization of offset Plate-Fin heat exchanger. *Materials Today: Proceedings* **77,** 142–147 (2023).

85. Moon, H., Mcgregor, D. J., Miljkovic, N. & King, W. P. Ultra-power-dense heat exchanger development through genetic algorithm design and additive manufacturing. *Joule* **5,** 3045–3056 (2021).

86. Che, M. & Elbel, S. Comparison of Local and Averaged Air-Side Heat Transfer Coefficients on Fin-and-Tube Heat Exchangers Obtained With Experimental and Numerical Methods. *Journal of Thermal Science and Engineering Applications* **14,** 1–13 (2022).

87. Goswami, R. D., Chakraborty, S. & Misra, B. *Variants of Genetic Algorithms and Their Applications* in *Applied Genetic Algorithm and Its Variants* (ed Dey, N.) (Springer Nature, Singapore, 2023), 1–20. ISBN: 978-981-9934-28-7.

88. Kalra, J. *et al. Design Optimization of Solar Thermal Energy Storage Tank: Using the Stratification Coefficient* in *Machine Learning, Advances in Computing, Renewable Energy and Communication* (eds Tomar, A., Malik, H., Kumar, P. & Iqbal, A.) (Springer, Singapore, 2022), 49–56. ISBN: 9789811623547.

89. Ajeeb, W., Thieleke da Silva, R. R. S. & Murshed, S. M. S. Experimental investigation of heat transfer performance of Al2O3 nanofluids in a compact plate heat exchanger. *Applied Thermal Engineering* **218,** 119321 (2023).

90. Taler, D. & Taler, J. Simple heat transfer correlations for turbulent tube flow. *E3S Web of Conferences* **13,** 02008 (2017).

91. Maarawi, A., Anxionnaz-Minvielle, Z., Coste, P., Raimondi, N. D. M. & Cabassud, M. 1D/3D Numerical Approach for Modelling a Milli-Structured Heat Exchanger/Reactor. *Chemical Engineering Transactions* **86,** 1441–1446 (2021).

92. Li, H. *et al.* The influence of catchment scale on comprehensive heat transfer performance about tube fin heat exchanger in numerical calculation. *Energy Reports* **8,** 147–155 (2022).

93. Marcinkowski, M., Taler, D., Taler, J. & Weglarz, K. Thermal Calculations of Four-Row Plate-Fin and Tube Heat Exchanger Taking into Account Different Air-Side Correlations on Individual Rows of Tubes for Low Reynold Numbers. *Energies* **14,** 6978 (2021).

94. González, A. M., Vaz, M. & Zdanski, P. S. B. A hybrid numerical-experimental analysis of heat transfer by forced convection in plate-finned heat exchangers. *Applied Thermal Engineering* **148,** 363–370 (2019).

95. Elmekawy, A., Ibrahim, A., Shahin, A., Al-Ali, S. & Hassan, G. Performance enhancement for tube bank staggered configuration heat exchanger - CFD Study. *Chemical Engineering and Processing - Process Intensification* **164,** 108392 (2021).

96. Petrik, M. & Szepesi, G. Experimental and Numerical Investigation of the Air Side Heat Transfer of a Finned Tubes Heat Exchanger. *Processes* **8,** 773 (2020).

97. Petrik, M., Szepesi, G. & Jármai, K. CFD analysis and heat transfer characteristics of finned tube heat exchangers. *Pollack Periodica* **14,** 165–176 (2019).

98. Khan, M. S., Zou, R. & Yu, A. Computational simulation of air-side heat transfer and pressure drop performance in staggered mannered twisted oval tube bundle operating in crossflow. *International Journal of Thermal Sciences* **161,** 106748 (2021).

99. Łecki, M., Andrzejewski, D., Gutkowski, A. N. & Górecki, G. Study of the Influence of the Lack of Contact in Plate and Fin and Tube Heat Exchanger on Heat Transfer Efficiency under Periodic Flow Conditions. *Energies* **14,** 3779 (2021).

100. Okbaz, A., Pınarbaşı, A. & Olcay, A. B. Experimental investigation of effect of different tube row-numbers, fin pitches and operating conditions on thermal and hydraulic performances of louvered and wavy finned heat exchangers. *International Journal of Thermal Sciences* **151,** 106256 (2020).

101. Rich, D. The effect of the number of tube rows on heat transfer performance of smooth plate fin-and-tube heat exchangers. *ASHRAE Transactions* **81,** 307–317 (1975).

102. Weglarz, K., Taler, D., Taler, J. & Marcinkowski, M. New calculation method for tube cross-flow heat exchangers. *E3S Web of Conferences* **323,** 00032 (2021).

103. Weglarz, K., Taler, D. & Taler, J. New non-iterative method for computation of tubular cross-flow heat exchangers. *Energy* **260,** 124955 (2022).

104. *Ansys Fluent Theory Guide* `https://dl.cfdexperts.net/cfd_resources/Ansys_Documentation/Fluent/Ansys_Fluent_Theory_Guide.pdf` (2023).

105. Menter, F. R. Two-equation eddy-viscosity turbulence models for engineering applications. *AIAA Journal* **32,** 1598–1605 (1994).

106. Wilcox, D. *Turbulence Modeling for CFD* (DCW Industries, Inc., La Canada, California, 1998).

107. Taler, D. & Ocłoń, P. Thermal contact resistance in plate fin-and-tube heat exchangers, determined by experimental data and CFD simulations. *International Journal of Thermal Sciences* **84,** 309–322 (2014).

108. Camerlengo, A. L. & O'Brien, J. J. Open boundary conditions in rotating fluids. *Journal of Computational Physics* **35,** 12–35 (1980).

109. *Kelvion. Compact Fin and Tube Coils.* `https://www.kelvion.com/products/product/coils/` (2023).

110. Menéndez Pérez, A., Fernández-Aballí Altamirano, C. & Borrajo Pérez, R. Parametric analysis of the influence of geometric variables of vortex generators on compact louver fin heat exchangers. *Thermal Science and Engineering Progress* **27,** 1–11 (2021).

111. Zhao, L., Gu, X., Gao, L. & Yang, Z. Numerical study on airside thermal-hydraulic performance of rectangular finned elliptical tube heat exchanger with large row number in turbulent flow regime. *International Journal of Heat and Mass Transfer* **114,** 1314–1330 (2017).

112. Okbaz, A., Pınarbas, A., Olcay, A. B. & Aksoy, H. An experimental, computational and flow visualization study on the air-side thermal and hydraulic performance of louvered fin and round tube heat exchangers. *International Journal of Heat and Mass Transfer* **121,** 153–169 (2018).

113. *Handbook of Grid Generation* ISBN: 978-0-367-80246-2 (CRC Press, Boca Raton, 1998).

114. Yang, H., Wen, J., Wang, S. & Li, Y. Effect of fin types and Prandtl number on performance of plate-fin heat exchanger: Experimental and numerical assessment. *Applied Thermal Engineering* **144,** 726–735 (2018).

115. Wang, C. C., Hsieh, Y. C. & Lin, Y. T. Performance of Plate Finned Tube Heat Exchangers Under Dehumidifying Conditions. *Journal of Heat Transfer* **119,** 109–117 (1997).

116. Wang, C. C., Chang, Y. J., Hsieh, Y. C. & Lin, Y. T. Sensible heat and friction characteristics of plate fin-and-tube heat exchangers having plane fins. *International Journal of Refrigeration* **19,** 223–230 (1996).

117. K.F., M. & Francis, O. B. *Correlation of Heat, Mass, and Momentum Transfer Coefficients in Plate-Fin-Tube Heat Exchangers* PhD thesis (Oklahoma State University, Stillwater, 1976).

118. Taler, D. Mathematical modeling and control of plate fin and tube heat exchangers. *Energy Conversion and Management* **96,** 452–462 (2015).

119. Marcinkowski, Mateusz, Taler, Dawid, Taler, Jan, Weglarz, Katarzyna & Lewandowski, Janusz. Efficiency and Maximum Temperature of Fins of Complex Geometry. *Journal of Power Technologies* **101,** 105–111 (2021).

120. Taler, D. & Marcinkowski, M. Calculating the Efficiency of Complex Shaped Fins. *Chemical Engineering Transactions* **81,** 1333–1338 (2020).

121. Harper, R. R. & Brown, W. B. *Mathematical equations for heat conduction in the fins of air-cooled engines* tech. rep. (1923). `https://ntrs.nasa.gov/api/citations/19930091223/downloads/19930091223.pdf` (2023).

122. Bošnjaković, M., Muhič, S., Čikić, A. & Živić, M. How Big Is an Error in the Analytical Calculation of Annular Fin Efficiency? *Energies* **12,** 1787 (2019).

123. Jing, H. *et al.* Thermal Performance and Energy Saving Analysis of Indoor Air–Water Heat Exchanger Based on Micro Heat Pipe Array for Data Center. *Energies* **13,** 393 (2020).

124. Taler, J. & Duda, P. *Solving Direct and Inverse Heat Conduction Problems* ISBN: 978-3-540-33471-2 (Springer, Berlin, Heidelberg, 2006).

125. Schmidt, T. Heat transfer calculations for extended surfaces. *J. ASHRAE, Refrig.,* 351–357 (1949).

126. Shah, R. & London, A. L. *Laminar Flow Forced Convection in Ducts* ISBN: 978-981-9934-28-7 (Academic Press, London, 1978).

127. Taler, D. & Taler, J. Steady-state and transient heat transfer through fins of complex geometry. *Archives of Thermodynamics* **35,** 117–133 (2014).

128. Osorio, J. D., Rivera-Alvarez, A. & Ordonez, J. C. Shape optimization of thin flat plate fins with geometries defined by linear piecewise functions. *Applied Thermal Engineering* **112,** 572–584 (2017).

129. Abernethy, R. B., Benedict, R. P. & Dowdell, R. B. ASME Measurement Uncertainty. *Journal of Fluids Engineering* **107,** 161–164 (1985).

130. Coleman, H. W. & Steele, W. G. *Experimentation, Validation, and Uncertainty Analysis for Engineers* 4th. ISBN: 978-1-119-41751-4 (Wiley, 2018).

131. Moffat, R. J. Using Uncertainty Analysis in the Planning of an Experiment. *Journal of Fluids Engineering* **107,** 173–178 (1985).

132. Taler, D., Taler, J. & Trojan, M. Experimental Verification of an Analytical Mathematical Model of a Round or Oval Tube Two-Row Car Radiator. *Energies* **13,** 1–21 (2020).